Exploring the Long-term and Extreme Variability of Stars

A dissertation presented

by

Sumin Tang

to

The Department of Astronomy

in partial fulfillment of the requirements

for the degree of

Doctor of Philosophy

in the subject of

Astronomy

Harvard University

Cambridge, Massachusetts

May 2012

Thesis Advisor: Professor Jonathan Grindlay Sumin Tang

Exploring the Long-term and Extreme Variability of Stars

Abstract

This thesis presents observational studies of long-term and extreme variability of stars with the Digital Access to a Sky Century@Harvard (DASCH) project. Stellar variations over decades are poorly explored. With the unique 100 years coverage of DASCH, for the first time, we are able to study the variable sky over long timescales in a systematic way. I have developed photometric calibration and variable search algorithms for DASCH. I have discovered exciting new types of long-term variables, which do not match any of the common classes, and studied the physical processes involved.

Following a brief introduction on variable stars and DASCH in the first chapter, I describe my work on DASCH pipeline, including photometric development and defect filtering in chapter 2. I present our discovery of a group of peculiar long-term K giant variables with $\sim$ 1 mag variations over decades in chapter 3. Follow-up observations show that they consist of two subgroups, including a subgroup of RS CVn binaries with strong magnetic activity, and another subgroup of single stars. In both cases, the variation amplitudes and timescales are abnormal, and may be related to either ultra strong star spots, or novel dust formation processes.

In chapter 4, I present the discovery of a 5 yr dip around 1900 in the eclipsing binary KU Cyg consisting of a F star and a K giant, which is related to the accretion disk surrounding the F star. It showed a slow fading ($\sim$ 4 yr), which is probably

caused by increases in dust extinction in the disk, and a relatively fast brightening ($\sim$ 1 yr), which may be due to the evaporation of dust transported inward through the disk. The extinction excess which caused the fading may arise from an increased mass transfer rate in the system or from dust clump ejections from the K giant, in accordance with K giant "dimming" as discussed above.

In chapter 5, I present a 10 yr nova-like outburst in a peculiar symbiotic system. With $P = 119$ days, it is interestingly located in the period gap region between classical novae and symbiotic novae. The most probable explanation of the outburst is hydrogen shell-burning on the white dwarf (WD) without significant mass loss, which suggests a promising new channel for Type Ia Supernovae (SNe).

In chapter 6, I present the DASCH light curves of Kepler planet-candidate host stars. We found no variation for these host stars. In chapter 7, I present my variable search algorithms and the resulting DASCH variable catalog for the Kepler field. The conclusion is presented in chapter 8.

Contents

Acknowledgments

I first want to thank my parents and husband for all of the love and support they have given me. Mom, Dad & Tian, thank you for everything.

It is a great pleasure to thank my advisor, Josh Grindlay, for all of the guidance throughout the past six years. Josh, thank you for your numerous insightful and creative comments and suggestions, thank you for always being available when I need to discuss with you, thank you for your swift responses to my questions even many of them are silly, and thank you for believing in me that I can do it. Your support and encouragement helped me gain confidence in my understanding of the astrophysical world, and helped me develop into an independent researcher.

I would like to thank all the other DASCH team members, who made this thesis possible. I especially want to thank Alison Doane, Edward Los, Bob Simcoe, Jaime Pepper, David Sliski, Silas Laycock and Mathieu Servillat for their work on DASCH. I would also like to thank many volunteers who have helped digitize logbooks, clean and scan plates, including George Champine, Chase Green, Julia Hardy, Ray Kenison, Jim Ostiguy, Steve Siok, Alan Sliski, Bill Toomey, volunteers at American Museum of Natural History and many others (*http://hea-www.harvard.edu/DASCH/team.php*).

I want to thank my committee members, Dimitar Sasselov, Avi Loeb and Rosanne Di Stefano for their guidance, support and invaluable advices, and Howard Bond at STScI, for his help and advices during the past years, and for flying all the way from Baltimore for my defense. Thank you for your insightful comments and

questions, and your feedback and edits on my thesis. I would also like to thank Martin Elvis for serving in my committee for several years, and for many great advices and help.

I have benefited a lot from the help and discussions from many colleagues at CfA. In particular, I want to thank Bob Kurucz, Max Moe, Jonathan McDowell, Dave Latham, Jose Fernandez, Sam Quinn, Lars Buchhave, Allyson Bieryla, Scott Kenyon, Andrea Dupree, Anna Frebel, Francesca Civano, Soren Meibom, Warren Brown, Ruth Murray-Clay, Matthew Holman, Branden Allen, Maureen van den Berg, Paul Green, Emilio Falco, Perry Berlind, Nelson Caldwell, Mike Calkins, Jessica Mink, Bill Wyatt and Susan Tokarz. I also want to thank Jerry Orosz at San Diego State Univ., and Ronald Gilliland at Penn State Univ. for their generous help on my projects.

I would like to thank my fellow Astronomy graduate students (past and present) for the supportive and friendly community they create. I especially would like to thank Ann Mao, Heng Hao, Roman Shcherbakov, Sasha Tchekhovskoi, Gongjie Li, Li Zeng, Wen-fai Fong, Joey Nelson, Robert Marcus, Jack Steiner, Laura Blecha, Xavier Koenig, Meredith Hughes, Heather Knutson and Gurtina Besla.

I would like to thank many of the faculty members for their support and advices, especially Julia Lee, Jim Moran, Ramesh Narayan, Irwin Shapiro, David Charbonneau, Bob Kirshner and Daniel Eisenstein. I want to thank the CF and HEA computer staff, for helping out on many things. I can not imagine that anyone could graduate without the hard work of Peg Herlihy, Donna Adams and Jean Collins; thank you for caring about us so much.

Last but not the least, I would like to thank all my other friends, and all the people I have climbed with, who made each day much more pleasurable.

For my Parents, and

For my dear husband, Tian.

Chapter 1

Introduction

1.1 Variable Stars

A star is called variable if its brightness changes over time. The variability could be extrinsic, such as eclipses by a companion star, or intrinsic, such as pulsations, flares, accretion variability, or explosions (see e.g. Hoffmeister et al. 1990; Percy 2007). Note that the definition of variable stars must depend on variability amplitude and timescales: All stars are variable if the measurement accuracy is high enough; Or if we could wait long enough, all stars are variable with evolutionary changes over their lives. Our Sun, a G2 main sequence star, varies at 0.1% level over the solar cycle due to sunspots activity (Fröhlich 2006), and such variability is normal among solar-type stars (Basri et al. 2010).

The study of variable stars has kept changing our understanding of the universe. Chinese, Japanese and Arab Astronomers recorded the supernova in 1054, which was

called a "guest star" in Chinese documents. On Nov 11th 1572, Tycho Brahe was astonished to see a "new star" (Brahe 1573), which was realized hundreds of years later as a Type Ia supernova in the Milky Way. Unlike other moving objects known to be variable at that time such as comets and planets, this "new star" at a fixed position, totally changed the view of a "celestial world in which no change takes place", and inaugurated a revolution in astronomy. In 1929, based on Henrietta Swan Leavitt's period-luminosity relationship for Cepheids discovered from the Harvard plates (Leavitt & Pickering 1912), Edwin Hubble published his paper on a rough proportionality of the objects' distances with their radial velocities, which revealed the expansion of the universe (Hubble 1929). In 1998, using type Ia supernovae as distance measures, astronomers discovered the accelerating universe (Riess et al. 1998; Perlmutter et al. 1999), with the new accelerating force now referred to as "dark energy".

In this thesis, I work on long-term and extreme variability of stars. By "long-term" , I mean timescales from days to 100 years; by "extreme", I mean variation amplitude $>\sim 0.5$ mag. In particular, I focus on unexpected rare variables with slow variations over years to decades, many of which are new types of variable stars. They may be related to dust processes, magnetic activity, accretion phenomena, or nuclear burning events, and provide important information about the physical processes involved.

1.2 DASCH Project

The time domain, especially on 10-100 yr timescales, is poorly explored despite its astrophysical importance. The Harvard College Observatory (HCO) maintains a collection of ∼500,000 glass astrophotographic plates from 1885 to 1992, constituting the largest continuous record of the whole sky in existence. Every point on the sky has been observed between 500 and 2000 times. This 100 years coverage is a unique resource for studying temporal variations in the universe on ∼1-100 yr timescales.

DASCH (Digital Access to a Sky Century @ Harvard) is a project to digitize and analyze the scientific data contained in the HCO plates. The motivation is to explore the temporal variations of stars and active galaxies on the relatively poorly explored $\sim 1-100$ yr timescales (but extending down to ~ 1 week timescales as well), and to make these data available to the astronomical community, as summarized by Grindlay et al. (2009). An ultra-high speed digital plate scanner has been built (Simcoe et al. 2006). We developed the astrometry and photometry pipeline (Laycock et al. 2010; Los et al. 2011; Servillat et al. 2011, Tang et al. in prep.), and have scanned over 20,000 plates in five initial fields, including M44, 3C 273, the Kepler field, Baade's Window and the Large Magellanic Cloud (LMC). Each plate covers 5−30 degrees on a side with typical limiting magnitudes of $B \sim 14-15$ mag, and most of them are blue sensitive emulsions (Laycock et al. 2010, Tang et al. in prep.).

With the advent of recent successful variability surveys, such as the Kepler space telescope (Borucki et al. 2010), and the Panoramic Survey Telescope and Rapid Response System (Pan-STARRS; Kaiser et al. 2002), the Palomar Transient

Factory (PTF; Law et al. 2009), the Catalina Real-Time Transient Survey (CRTS; Djorgovski et al. 2011), the All Sky Automated Survey (ASAS; Pojmanski 2002), the MAssive Compact Halo Objects project (MACHO; Alcock et al. 2000), the Optical Gravitational Lensing Experiment (OGLE; Udalski et al. 1997), and the future Large Synoptic Survey Telescope (LSST; Tyson et al. 2003; Walker 2003), we are entering a golden era of time domain astronomy. Compared with other modern time-series data, DASCH extends the field on the timescale dimension, and provides irreplaceable information on the long-term evolution of the variable sky.

1.3 DASCH Pipeline

Here I briefly describe how the DASCH pipeline works; a flow chart is shown in Figure 1.1. Plates are cleaned, to remove writing marks and dust, and then scanned (Simcoe et al. 2006). We started with SExtractor (Bertin & Arnouts 1996) to extract star images. We use Astronometry.net (Lang et al. 2010), WCSTools (Mink 2002), and SCAMP (Bertin 2006) to get astrometric solutions (Servillat et al. 2011). We also do iterative processing to derive astrometric solutions for multiple exposure plates (Los et al. 2011). Next, we flag the blended images, plate defects (Tang et al. in prep.), and Pickering Wedge images (Los et al. 2011). We then divide each plate image into nine annular bins to correct vignetting and radially dependent PSF variations, derive the effective color response of each plate, fit the calibration curves, and run two local correction algorithms, to correct for the inhomogeneity of the plate (Laycock et al. 2010, Tang et al. in prep.).

Combined with the meta-data from the logbooks, we get the light curves of

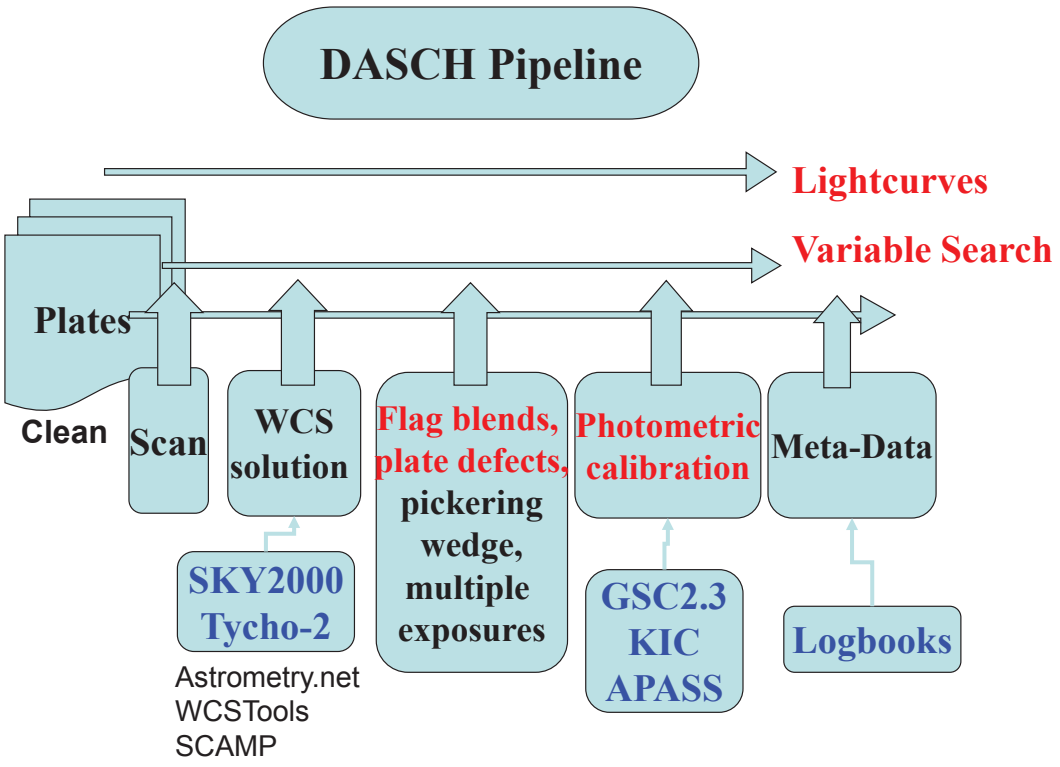

Figure 1.1.— Flow chart of DASCH pipeline. I marked the parts I developed or contributed significantly in red, including flagging blended images, filtering out image defects, photometric calibration, and the variable search.

each object. I developed a pipeline to search for variable objects utilizing a set of measurements, including light curve RMS, amplitude, number of outburst and dip points, long-term trends in the light curves. More details are presented in Chapters 2 and 7.

1.4 Follow-up Observations

Finding peculiar variables in DASCH is only the first step of the study. Follow-up observations, especially spectroscopic observations, are essential for understanding their properties and the physical processes involved.

I have done significant amount of follow-up observations mostly using FAST and TRES spectrographs on the FLWO 1.5m telescope, and also the Hectochelle spectrograph on MMT and the MIKE spectrograph on Magellan. These spectra provide a lot of information on the stars. They are used to derive spectral and luminosity classifications, radial velocities and orbits, and stellar parameters such as temperatures, surface gravity and metallicity. Some spectral lines, such as Ca H&K and Hα emission lines, also help us understand their magnetic activity levels.

Chapter 2

Developments in DASCH Photometry

S. Tang, J. Grindlay, E. Los, & M. Servillat *The Astronomical Journal*, in prep.

S. Laycock, S. Tang, J. Grindlay et al. *The Astronomical Journal*, Vol. 140, pp. 1062-1077, 2010

Abstract

Here I describe the DASCH photometry pipeline, focusing on the parts I developed. The initial photometry developments, including annular bin photometry, plate color-term fitting, are described in Laycock et al. (2010). New photometry developments, including identifying blended images, filtering out defects by using image profiles and large astrometric deviations, as well as improved local calibrations by using neighbor stars with similar magnitudes and colors, are described in Tang et al. (in

prep). All of the above developments are designed to serve the scientific purpose of finding real variables on DASCH plates. DASCH data from the Kepler field are used to illustrate the new photometry and light curve analysis tools. We report that our photometry accuracy is about $0.1 - 0.13$ mag. We also define statistical measurements of light curves, which will be used for selecting variable stars. The variable search and results for the Kepler field are presented in Chapter 7.

2.1 Introduction

During the development phase for the high speed DASCH scanner (Simcoe et al. 2006) and analysis software, we have scanned over $20,000$ plates in five selected fields covering M44, 3C 273, Baade's Window, the Kepler field, and the Large Magellanic Cloud (LMC). The initial photometry and astrometry developments are described in Laycock et al. (2010; hereafter L10). The pipeline and database is described in Los et al. (2011). Further astrometry development is described in Servillat et al. (2011). As a pilot scientific study, we have discovered interesting long-term variables with ~ 1 mag variations over years to decades, which provide important information about dust processes, accretion physics and possible nuclear shell burning on the surface of white dwarf (Tang et al. 2010, 2011a,b).

It is now an unprecedented era for the time domain astrophysics, with the advent of large time domain surveys such as the Panoramic Survey Telescope and Rapid Response System (Pan-STARRS; Kaiser et al. 2002), the Palomar Transient Factory (PTF; Law et al. 2009), the Catalina Real-Time Transient Survey (CRTS; Djorgovski et al. 2011), and the future Large Synoptic Survey Telescope (LSST;

Walker 2003). DASCH, with its unique 100 year time coverage and sampling, opens a new window of studying variables, especially the ones with long timescale variations. This requires the correct removal of plate defects (dust, scratches, etc. that are more likely on old plate images) as well as good astrometry and photometry on each resolved object.

One of the particularly interesting fields is the Kepler mission field. We have scanned 3654 plates taken from 1885 to 1990, in or covering part of the Kepler field. Most plates are blue-sensitive, close to Johnson B. Since the only plates scanned for the "Kepler field" were chosen to contain part or all of the Kepler field, the coverage for any given star decreases with increasing radius from the center of the Kepler field, as shown in Figure 2.1. At any given point within the Kepler field of view (FOV), there are at least 1500, 1000, 450, and 130 plates down to B =12, 13, 14, and 15 magnitudes, respectively. For photometric calibration, we used the Kepler Input Catalog (KIC) which contains Sloan-like griz photometry (Brown et al. 2011). KIC covers $\sim$ 177 square degrees centered at RA 19:22:40 and Dec +44:30, which is smaller than our scanned region. In other fields, we used the GSC2.3 catalog (Lasker et al. 1990), and the AAVSO APASS catalog (`http://www.aavso.org/apass`) for photometric calibration. For all other sky fields, we use the newly released APASS photometric catalog (BVR, gri) with photometric uncertainties ($<$ 0.05mag) some 4 times better than the GSC2.3.2 catalog used in our initial photometry (L10).

Here I describe the photometry developments I developed, including annular bin photometry, plate color-term fitting, identifying blended images, filtering out dubious detections by image profiles and high astrometry deviations, improved local calibration using neighbors with similar magnitudes. The above developments

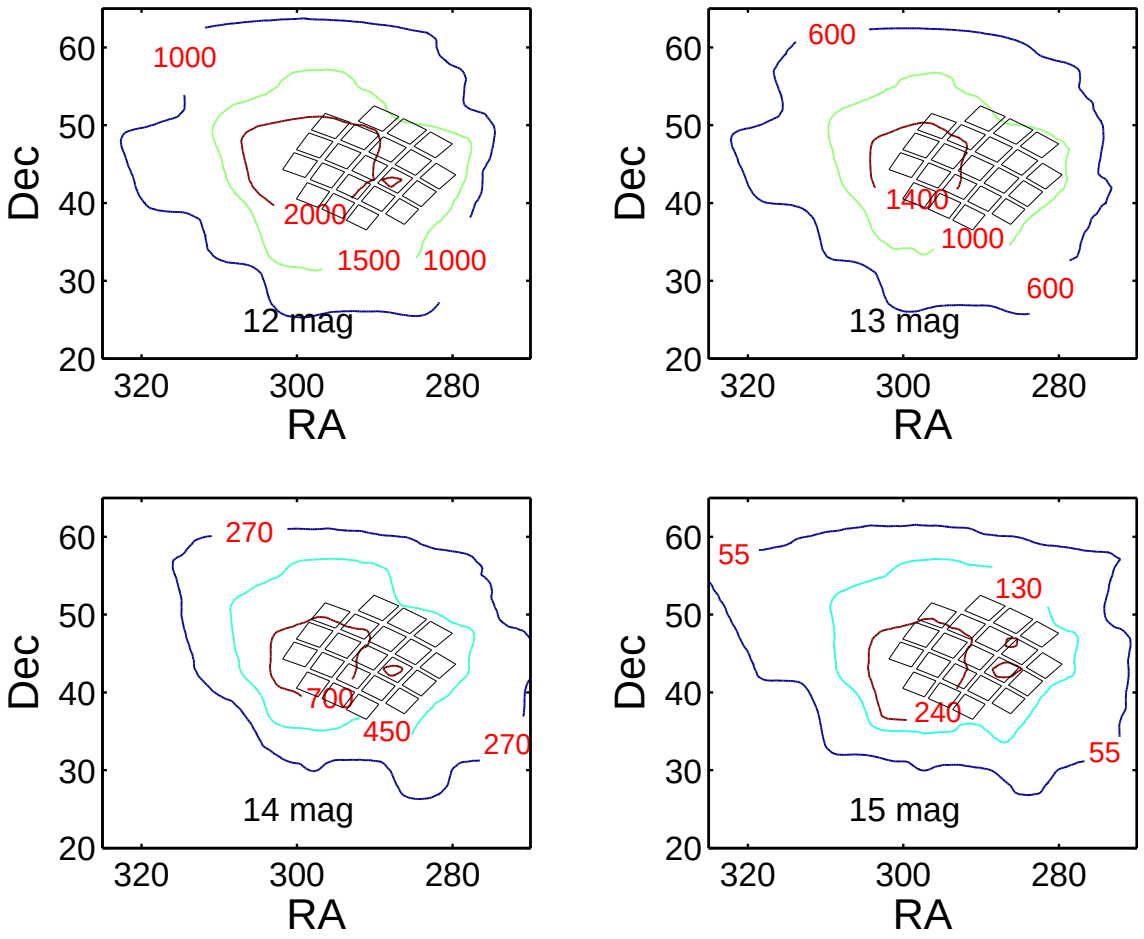

Figure 2.1.— Coverage contour of number of digitized plates in or covering part of the Kepler FOV. Four panels show number of plates reaching limiting magnitude of 12 mag (upper-left panel), 13 mag (upper-right panel), 14 mag (lower-left), and 15 mag (lower-right), respectively. The Kepler FOV is overlaid (black squares) in each panel.

are all essential to finding real variables on DASCH plates. We also describe statistical measurements of light curves, which will be used for selecting variables. A subsequent paper in preparation will report on the details of the initial DASCH variable search for the Kepler field (Tang et al 2012; Chapter 7).

2.2 Annular Photometry and Color-term Fitting of Plates

Here I briefly describe DASCH annular photometry and color-term fitting of plates. More details can be found at Laycock et al. (2010).

Given the heterogeneous nature of the plate collection, the characteristic calibration curve, i.e. the instrumental magnitude vs. the catalog magnitude, is different for every single plate. Moreover, given the inhomogeneity of a plate, including vignetting and position dependent variations, the calibration curve also differs from place to place on a given plate. We first divided each plates into 9 annular bins, as shown in Figure 2.2. Next, we fit the calibration curve in each bin separately. After extensive experimenting, we found that no polynomial model works consistently well to fit the calibration curve. We identified the statistical-analysis function *rlowesss* (Cleveland 1981), a robust (zero weight to outliers) local regression using weighted linear least squares and a first degree polynomial model, works the best for our calibration. An example fit is given in Figure 2.3.

Another issue is the color responses of plates. Most Harvard plates are blue sensitive plates without filters, with a color response close to Johnson B. However,

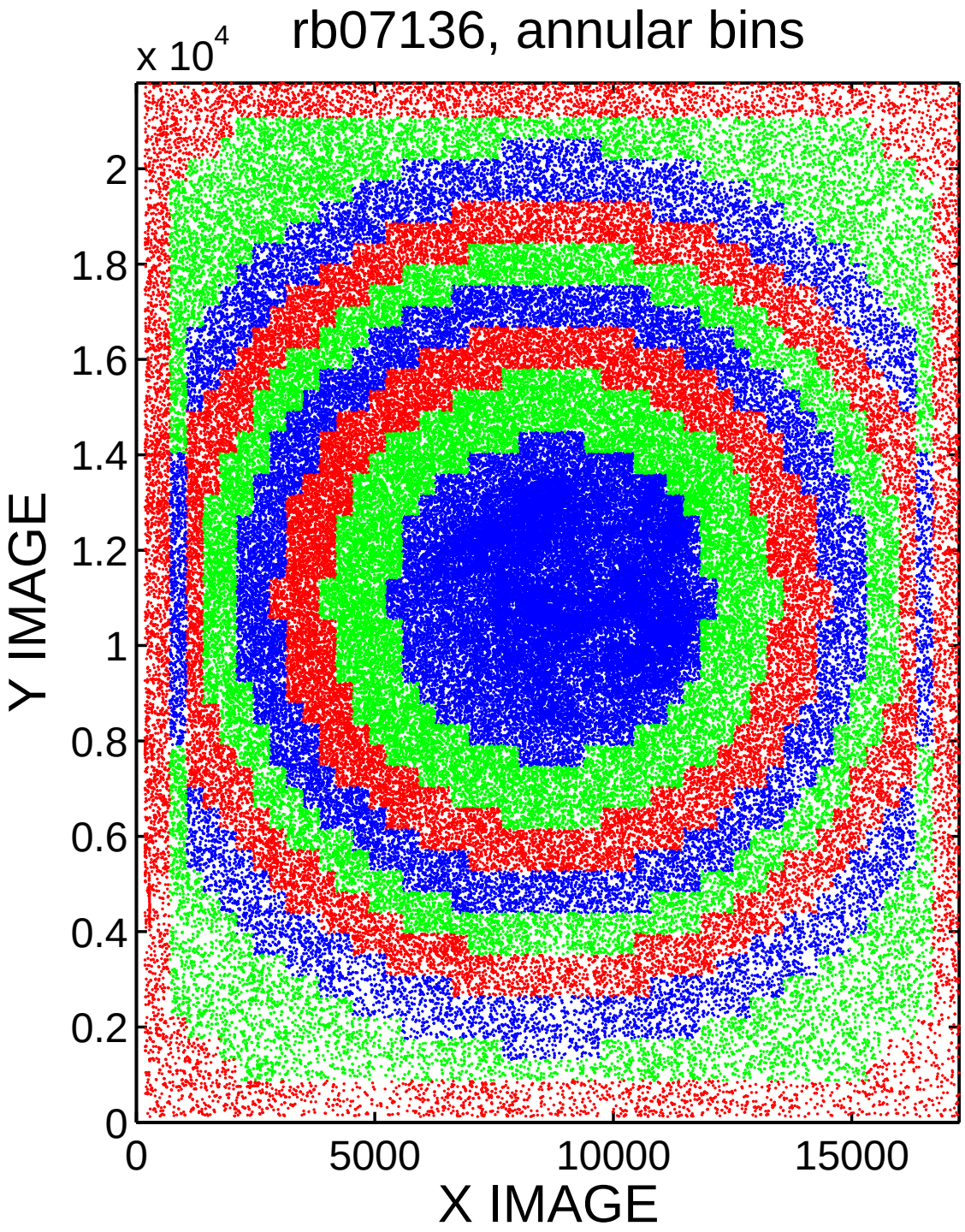

Figure 2.2.— Nine annular bins on plate rb 07136, to remove radial dependence of vignetting. There are thousands of stars in each bin, which insures independent calibration of magnitude values in each bin.

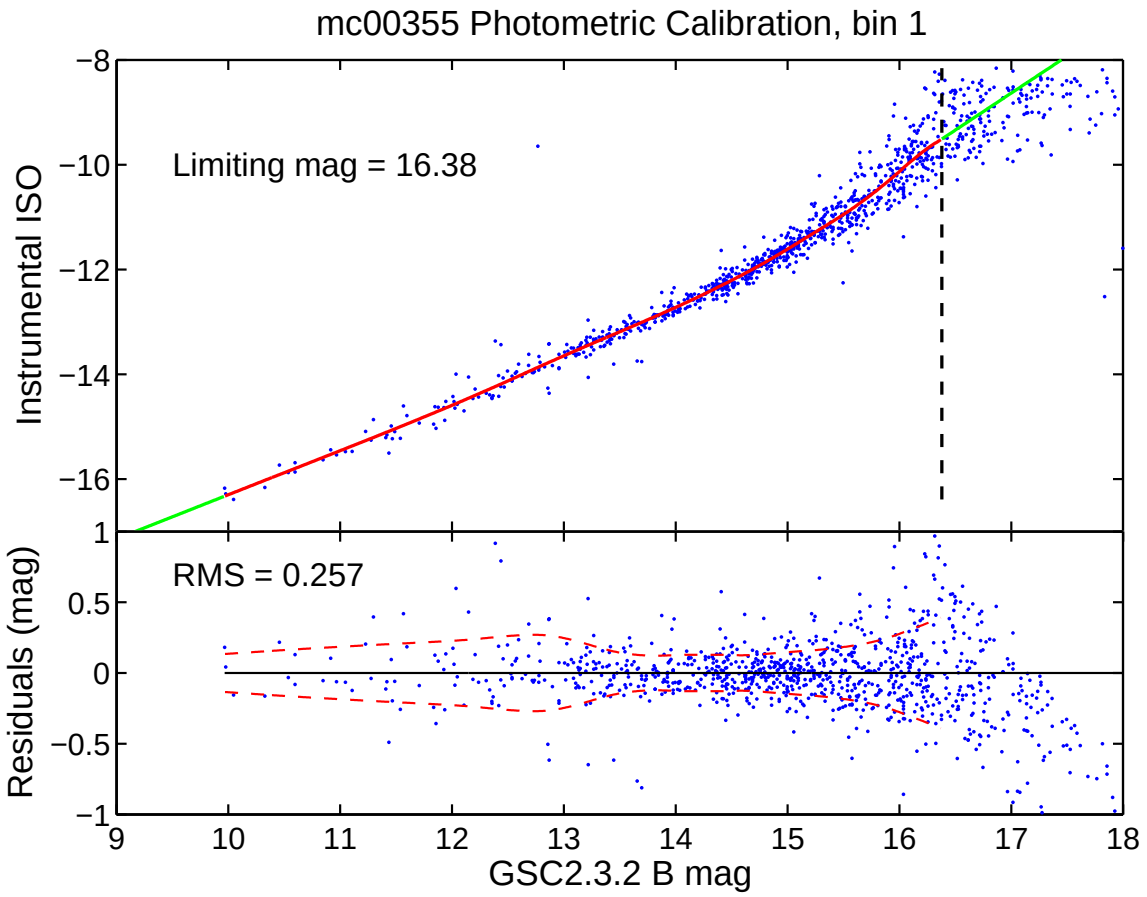

Figure 2.3.— Photometric calibration for bin 1 of plate mc 00355. The upper panel shows isophotal magnitudes from SExtractor vs GSC2.3 B magnitude. Blue dots are images matched with GSC stars, the red line is the calibration curve, and green lines are extrapolation of the calibration curve in bright end where there are no or too few stars, and the faint end beyond the limiting magnitude, which is indicated by the vertical black dashed line. The lower panel shows the calibration residuals vs GSC B magnitude, and the red dashed lines indicate the RMS of residuals at different magnitudes, which is mainly due to the error of GSC catalog.

a small fraction of the plates used red and yellow filters. In order to generate consistent and precise magnitudes, it is essential to understand the color response in each plate and correct it. We derive the color term C, by minimizing rms in the calibration curve. An example is shown in Figure 2.4. GSC2.3 B and R magnitudes are used in the calculation. $C = 0$ means the color response is the same as GSC B, and $C = 1$ means the color response is the same as GSC R. Figure 2.5 shows the color term distribution for M44 plates. Note that there is a color term change for rh plates in 1932, which is probably related to the telescope site move, and hence possible change of plate supply that year.

2.3 Identify blended images

Some scanned fields are crowded, such as the Kepler field, Baade's Window and LMC. Moreover, due to overexposure and trailing on some plates, many bright objects may have their photometry contaminated by nearby objects. The effective brightness of the blended image is the sum of the fluxes of all of the component stars, but since plates are nonlinear, these blended images must be recognized and removed from the Photometry analysis. Otherwise, large errors/deviations from the true magnitude in the blended stars will lead to fake variables, which will severely pollute the pool of variables we are ultimately looking for.

SExtractor is used for object detection and photometry (L10) does some image deblending but requires a saddle point in the point spread function (psf) that is usually lost for saturated stars. Therefore, many blended images are not recognized as blended in SExtractor. To overcome this problem, we use a second criterium to

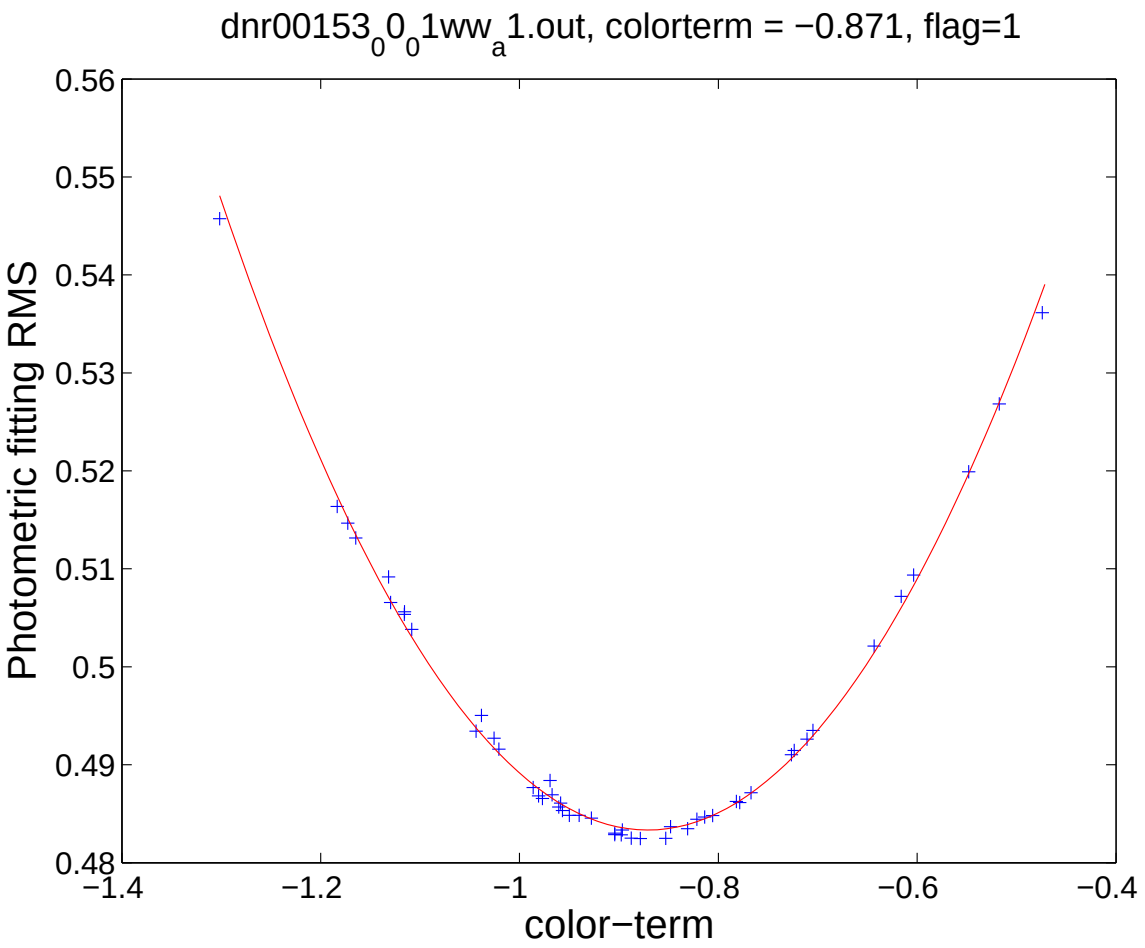

Figure 2.4.— Color-term fitting for damons north red plate dnr00153. The color response of each plate is determined by stepping through a series of values of color term C, repeatedly fitting the calibration curve, so as to locate the C value producing the minimum rms in the residuals. The reference stars are GSC2.3 photoelectric magnitudes and the minimum scatter occurs for $C = -0.873$, meaning that the plate response $= B - 0.873(B - R)$; hence, this is confirmed to be a red-sensitive plate with an effective passband very close to R.

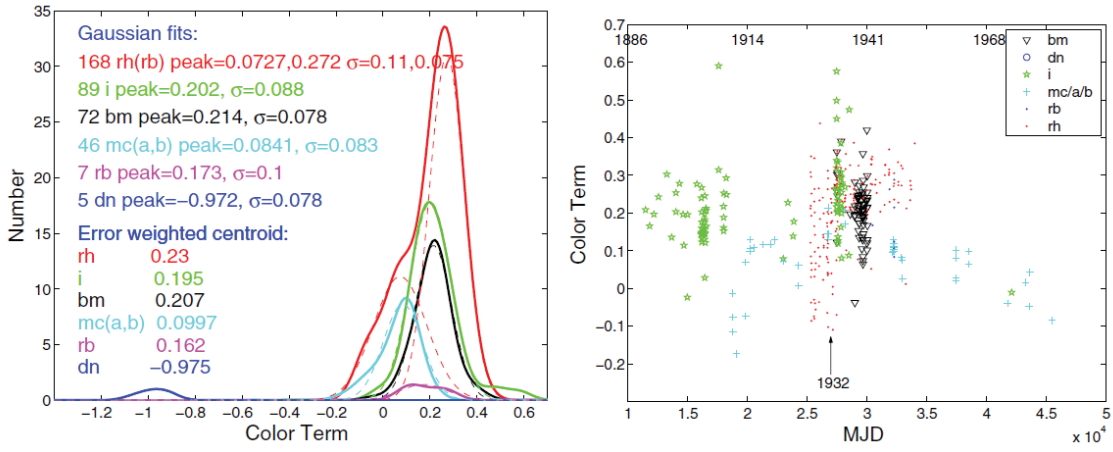

Figure 2.5.— Color term C by plate series and year. The color terms were obtained by minimizing the scatter in the calibration curve for each plate, relative to Johnson B and R magnitudes, such that B magnitude corresponds to $C = 0$, which is very close to the result obtained for most of our sample. Left: each plate series defines a distinct distribution which is well described by a single Gaussian; parameters from these fits are given in the legend. Five dn plates observed through a red filter were included for comparison; these appear at $C \sim -1$, which corresponds closely to Johnson R, confirming the reliability of our technique. Right: the same data are plotted against time, showing the variations in emulsion properties. Note the change in response for rh plates that occurred in 1932, possibly due to the change of plate supply related to the telescope site move that year.

flag blended stars besides the SExtractor flag. We adopt a critical separation radius, Δr_{crit}, which is the sum of one half of the SExtractor full width half maximum (FWHM) radius and the astrometric error. For any SExtractor object, we search the input catalog (which is KIC in this paper) for stars within Δr_{crit}. If there are multiple KIC stars matching one SExtractor object, then only the brightest star is accepted, while all the others are flagged as blended. For the brightest star, if the total flux of all the other stars within Δr_{crit} contribute to more than 10% of the brightest star, then it is also flagged as blended.

The FWHM of a star image on a plate depends on the brightness of the star and the plate properties, as shown in Figure 2.2. It ranges from $10 - 20''$ on small plate scale plates such as the mc plates (with scale 98"/mm), and up to $40 - 100''$ on large plate scale plates such as ac (606"/mm) and dnb (507"/mm). The astrometric error is much smaller than the FWHM, with typical values from sub-arcsecond to a few arcseconds, mostly depending on plate series (L10; Servillat et al. 2011).

2.4 Filter out Dubious Detections

2.4.1 Image Profiles

There are many kinds of defects on the plates, including emulsion defects, scratches, ink marks, dust particles not removed, and even airplane and satellite tracks (post 1957), which all must be "removed" in the search for variables. Ink marks (from visiting astronomers annotations of objects they were working on, and present on about 20% of the Harvard plates), and most of dust particles as well as "smudges"

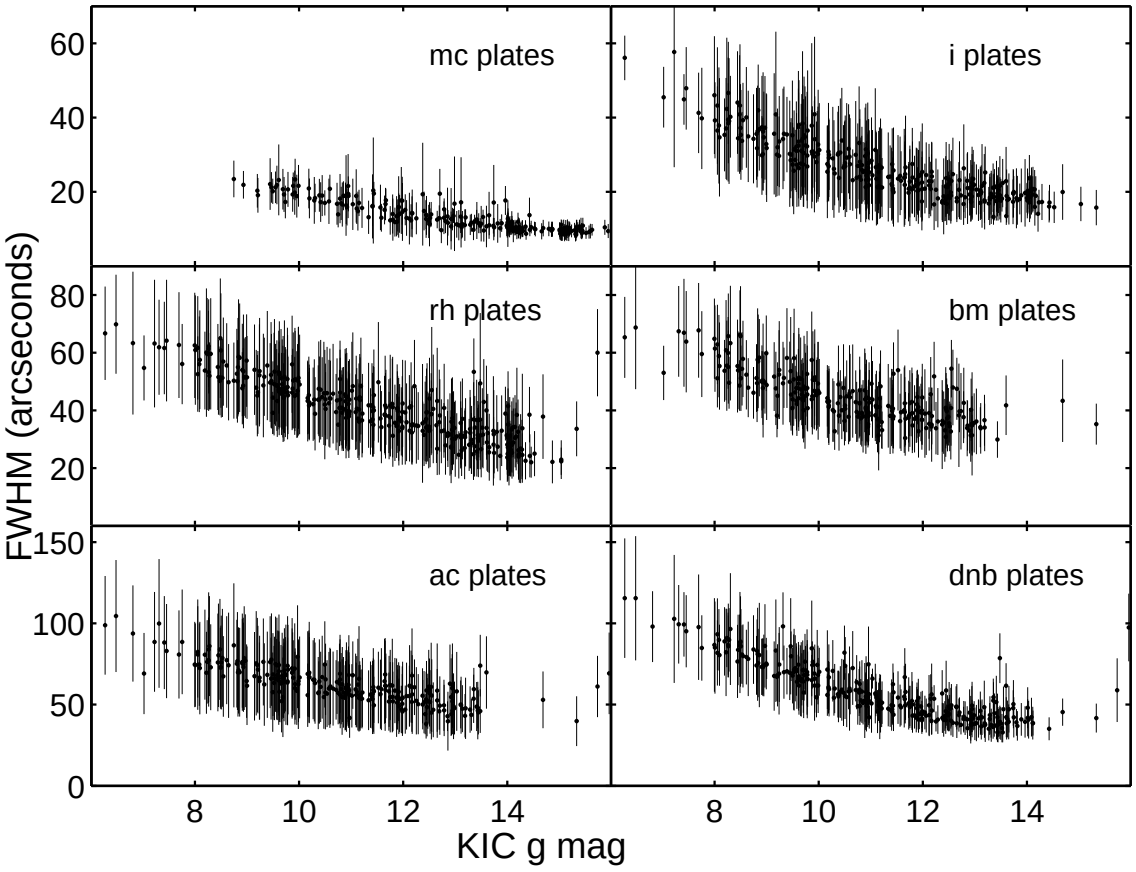

Figure 2.6.— Image size (FWHM) of 400 randomly selected stars vs magnitude over different plate series (6 of the ∼10 principal series). For any given plate series, the solid points present the mean value of FWHM over different plates, and the error bars show the rms.

are removed during the plate cleaning (of the clear glass back side of the plate, which also contains (∼20% of all plates) annotations from the many users of the historical plates) before scanning, but other defects remain there. We have to identify these defects before any scientific study.

Fortunately, most defects have different image profiles from real stars, which provides a way to filter them out. Plates are highly inhomogeneous, and images in different parts of the plate have different profiles, as shown in Fig. 2.7 which shows image parameters (from SExtractor) vs. spatial bin location on the plate. Therefore, we divided each plate into 5×5 bins to do the filtering. Objects at edges (within 5% of the plate width and height to plate edges) and corners (beyond 85% of the distance from the plate center to one of the corners) are excluded in the analysis to avoid contaminations, as they are usually highly distorted. We used SExtractor parameters as profile measurements, including ellipticity, position angle (θ), instrumental isophotal magnitude (MAG_ISO), FWHM (in arcsec), maximum flux with background subtracted (in counts), and isophotal area above the analysis threshold (ISO0, in units of pixel^2). Most defects are located at different regions in at least one or more parameter spaces from real star images, as shown in Figures 2.8-11.

Filters are applied in the following four parameter spaces, as shown in Figures 2.8-11:

1. Ellipticity vs position angle, as shown in Figure 2.8. Objects beyond 2σ in ellipticity and objects beyond 2.5σ in position angle are flagged as defects.

2. log(FWHM) vs instrumental magnitude, as shown in Figure 2.9. Objects are

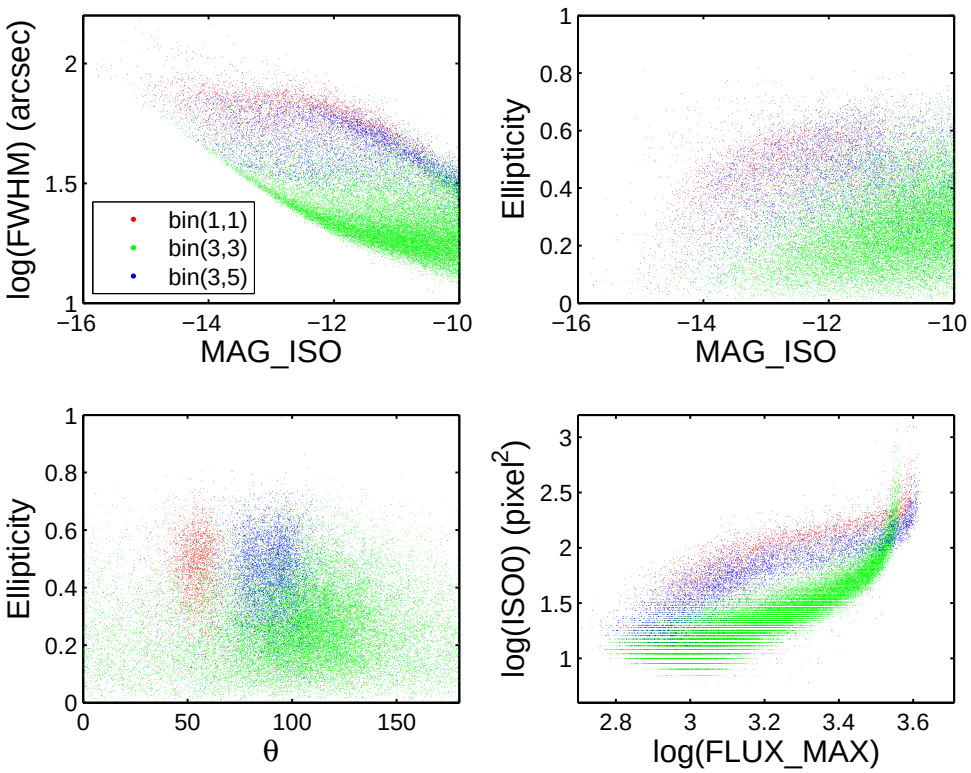

Figure 2.7.— SExtractor parameter distributions for stars in different local bins of plate rh08346.

divided into 15 instrumental magnitude bins. In each bin, median and rms values of log(FWHM) are derived after two iterations of 3σ clipping. Objects beyond 2σ are flagged as defects.

3. Ellipticity vs instrumental magnitude, as shown in Figure 2.10. Objects are divided into 15 instrumental magnitude bins. In each bin, median and rms values of ellipticity are derived after two iterations of 3σ clipping. Objects beyond 2σ are flagged as defects.

4. log(ISO0) vs log(maximum flux), as shown in Figure 2.11. Objects are divided into 20 log(maximum flux) bins. In each bin, median and rms values of log(ISO0) are derived after two iterations of 3σ clipping. Objects beyond 2σ are flagged as defects.

Both real stars and defects have wide distributions in parameter phase spaces, and the ideal goal that all defects are filtered out while all real stars are kept is impossible. Tighter constraints lead to less contamination from defects, while more real stars are lost; looser constraints yield more real stars, but with higher level of contamination from defects. We chose a $2-\sigma$ cut-off to balance, and the resulted ratios are shown in Figure 2.12. The objects identified as defects are flagged, and still kept in the pipeline.

2.4.2 Drad filter

Since we started matching using a search radius ($FWHM/2$+ astrometric error) much larger than our astrometric error, we might include wrong matches, mostly real

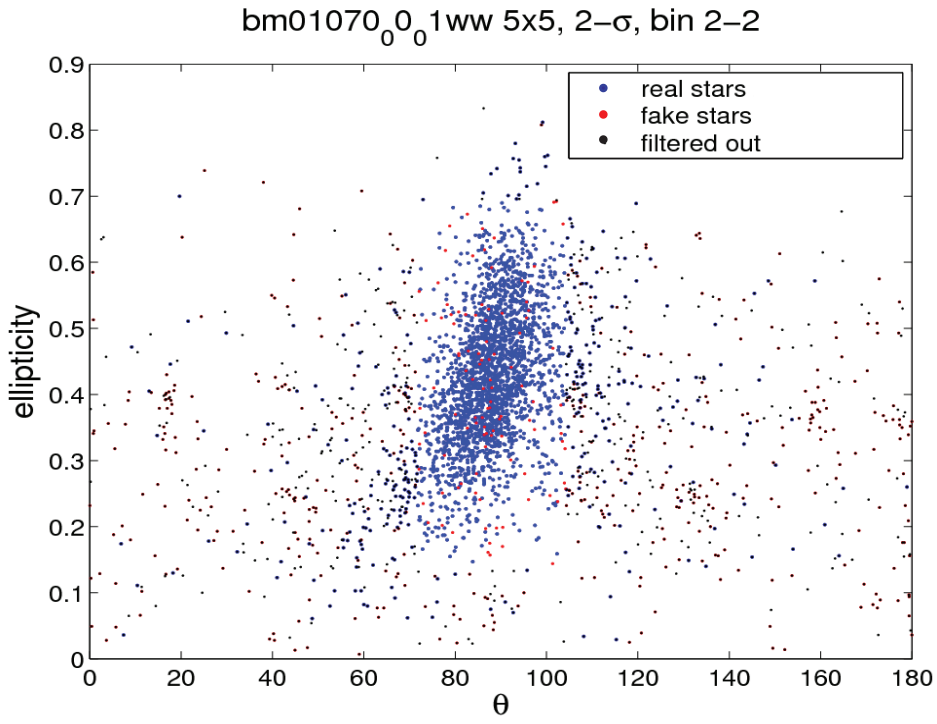

Figure 2.8.— Ellipticity vs PA for stars in a local bins of plate BM01070.

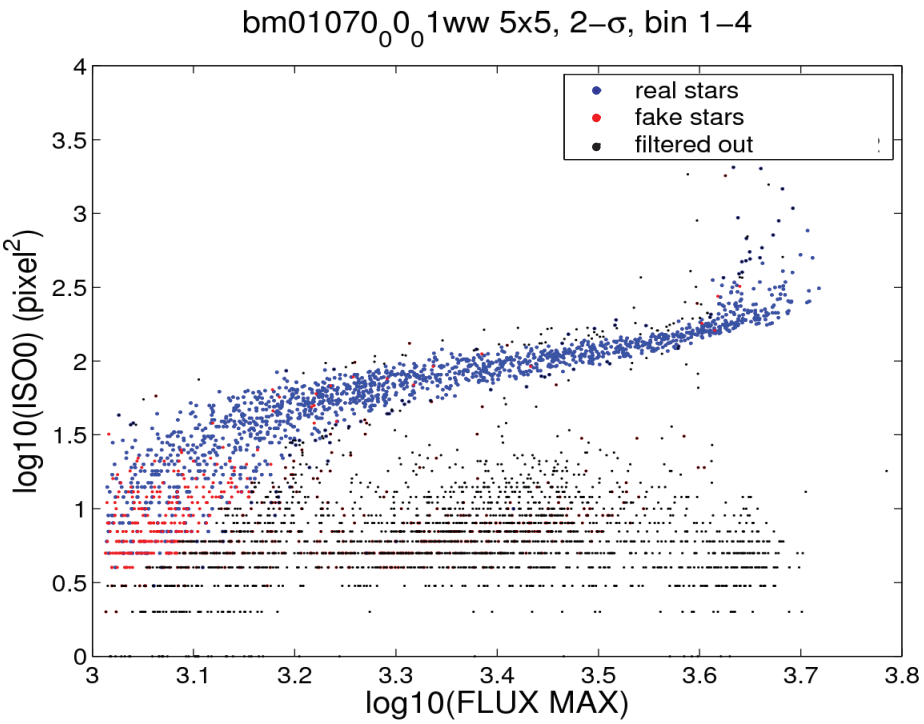

Figure 2.9.— Flux$_{max}$ vs isophotal area above the analysis threshold for stars in a local bins of plate BM01070.

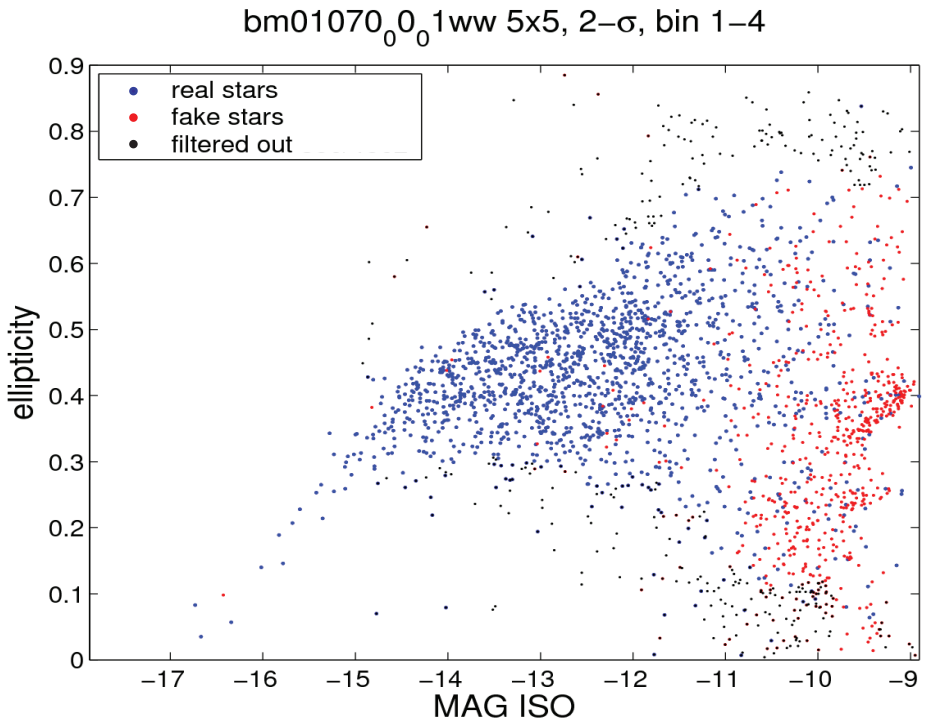

Figure 2.10.— Ellipticity vs Magnitude for stars in a local bins of plate BM01070.

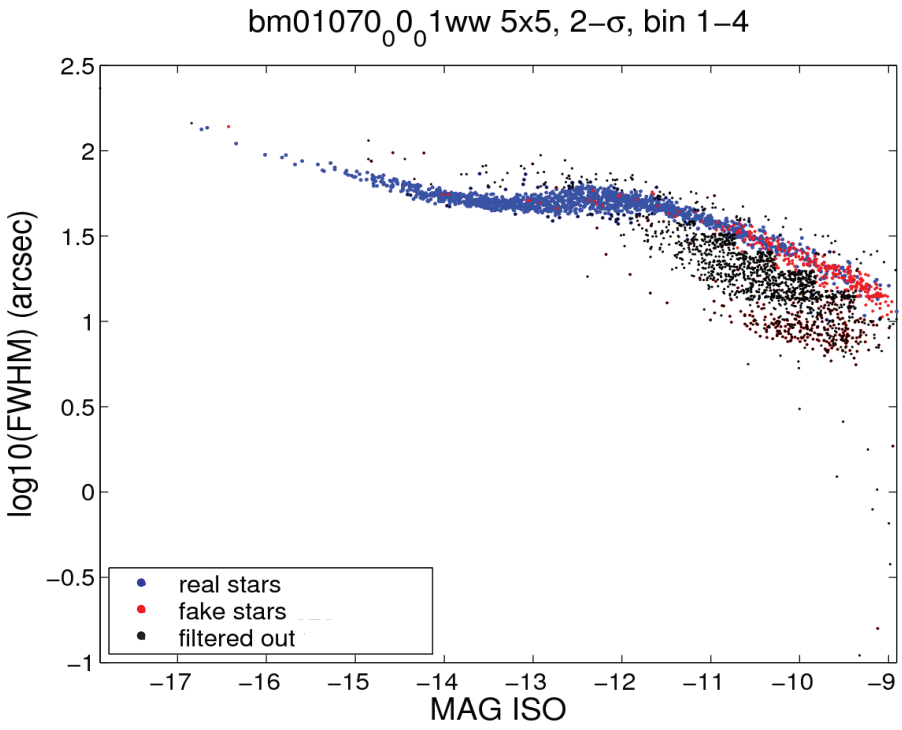

Figure 2.11.— FWHM vs Magnitude for stars in a local bins of plate BM01070.

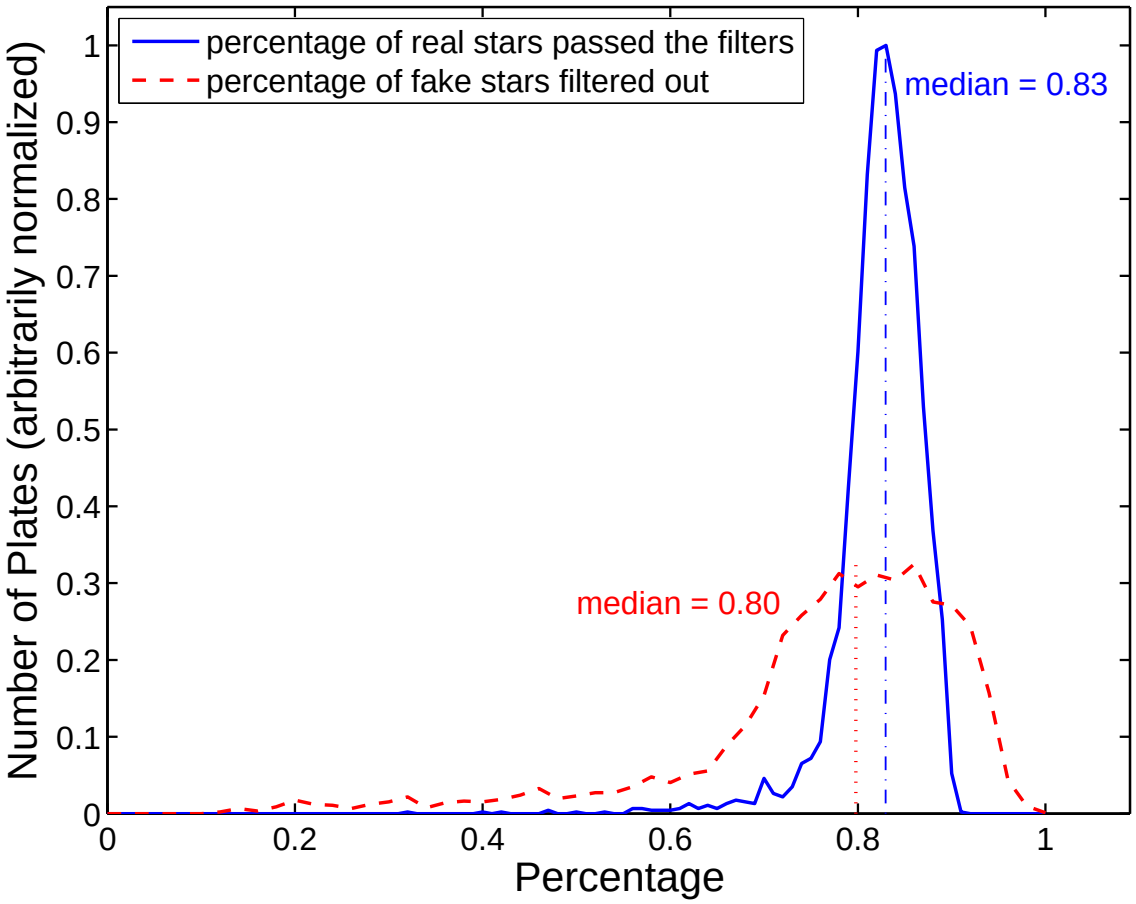

Figure 2.12.— Efficiency of defect filters. They are based on the SExtractor parameters characterizing the image profiles. The blue solid line shows the percentage distribution of real stars, i.e., images matched with KIC objects with similar magnitudes, passed the filters; its median value, i.e. 0.83, is marked by the blue dash-dotted line. The red dashed line shows the percentage distribution of fake stars, i.e., images not matched with KIC objects thus most likely defects, failed the filters; its median value, i.e. 0.80, is marked by the red dotted line. The above results are based on 3898 plates in the Kepler field.

stars matched with noise or defects. We define drad as the difference between the SExtractor image position and the input catalog (KIC, APASS, or GSC catalogs) position. We first find the median $|drad|$ in the local bin defined as 50×50 grids on each plate and the rms dispersion, σ_{drad}, of the $|drad|$ values in this bin, as a measure of our astrometry uncertainty, and then flag stars with a drad greater than $3\sigma_{drad}$ plus a two pixels as wrong matches.

2.5 Improved local calibration using neighbors with similar magnitudes

After defect filtering, we divide each plate into 9 annular bins in order to proceed with photometry calibrations that will naturally take into account radial vignetting effects from the original telescope. In each annular bin, we derive the effective color response by minimizing the scatter in the catalog magnitude vs instrumental magnitude plane, and fit the calibration curve for each bin (Laycock et al. 2010). To correct the localized spatial variations in plate sensitivity, a first round local calibration is performed in 50×50 "local bins", where a clipped median magnitude residual (plate magnitude - catalog magnitude) is computed for each bin, and applied to each star's magnitude (Laycock et al. 2010). As there are many more faint stars in each bin which dominate the median residual, the first round local calibration accounts well for the spatial variations of the fainter stars, but not well for bright stars, especially the ones with $B < 10 - 11$ mag, as shown in Figure 2.13.

To further improve the photometry, we perform a second round local calibration,

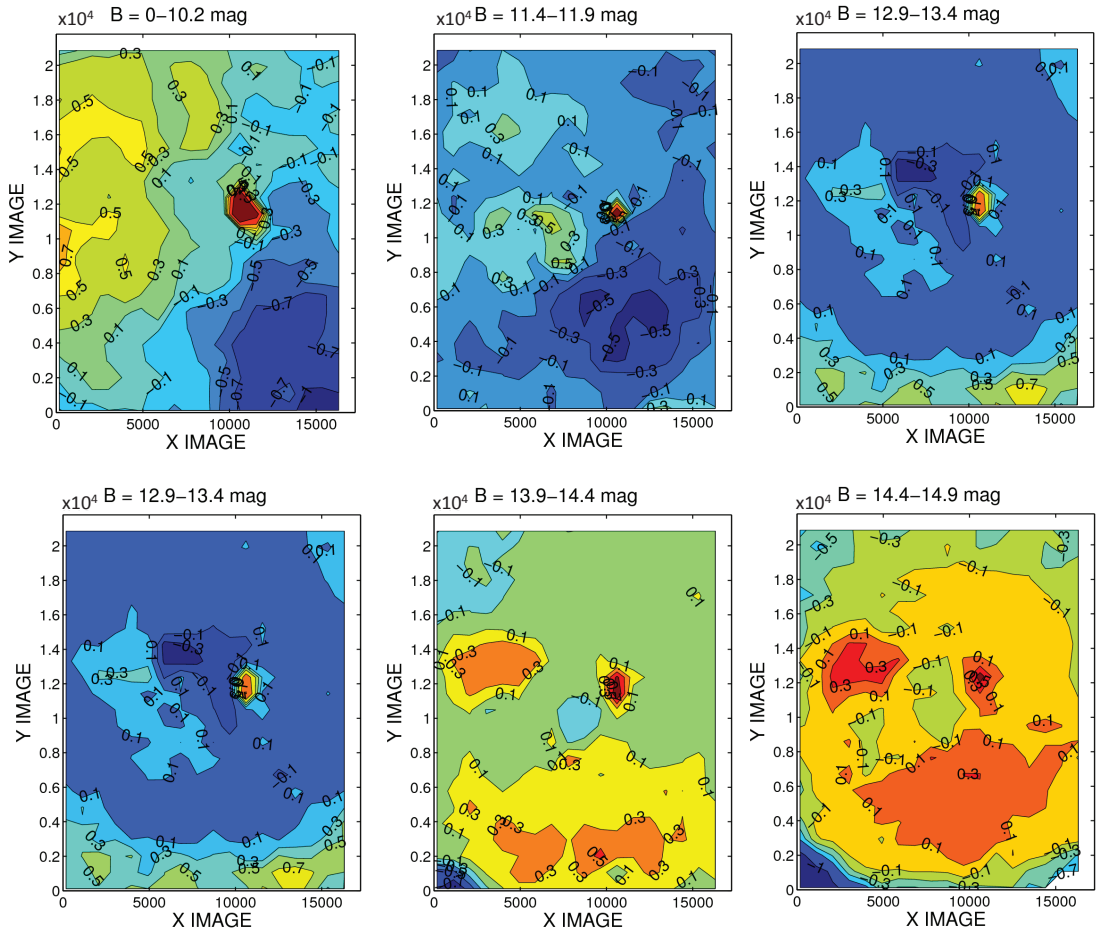

Figure 2.13.— Magnitude residual (plate magnitude - catalog magnitude) contour of plate rh07136 for stars in different magnitude bins. The X and Y axis are in units of pixels. Different colors are for different contour levels.

using neighbor stars with similar magnitudes. We first divide stars in magnitude bins, requiring a minimum number of stars in each magnitude bin of 5000, and a minimum bin size of 0.5 mag. For each magnitude bin, we then divide the plate into ~ 400 quasi-square spatial bins, for example, 17×23 spatial bins for a $8^\circ \times 11^\circ$ plate. If the number of stars in a magnitude-spatial bin is less than 20, we expand the bin until it contains at least 20 stars. We then calculate the clipped median magnitude residual, and apply the residual correction to the magnitude of each star in the bin. Figure 10 shows the magnitude residual correction vs magnitude we derived for 9 example spatial bins on plate rb07136. The median magnitude residual depends on both the spatial location, which reflects the inhomogeneity of the plate, and the magnitudes of stars, which suggests that fitting a dmag vs catalog mag to a sequence of stars around the given star would further improve the photometry. In principle, this is similar to what people do when examining the plates using eyepieces, i.e. comparing the image of the target object with a sequence of neighbor stars with similar magnitudes.

2.6 DASCH Photometry Performance and Sensitivities for Variables

There are two measures of DASCH photometry performance. The first is light curve rms. As most stars are not variable at the ~ 0.1 mag level, the light curve rms is dominated by photometric uncertainty, and the median light curve rms corresponds to the average uncertainty. The second is the number of unrecognized

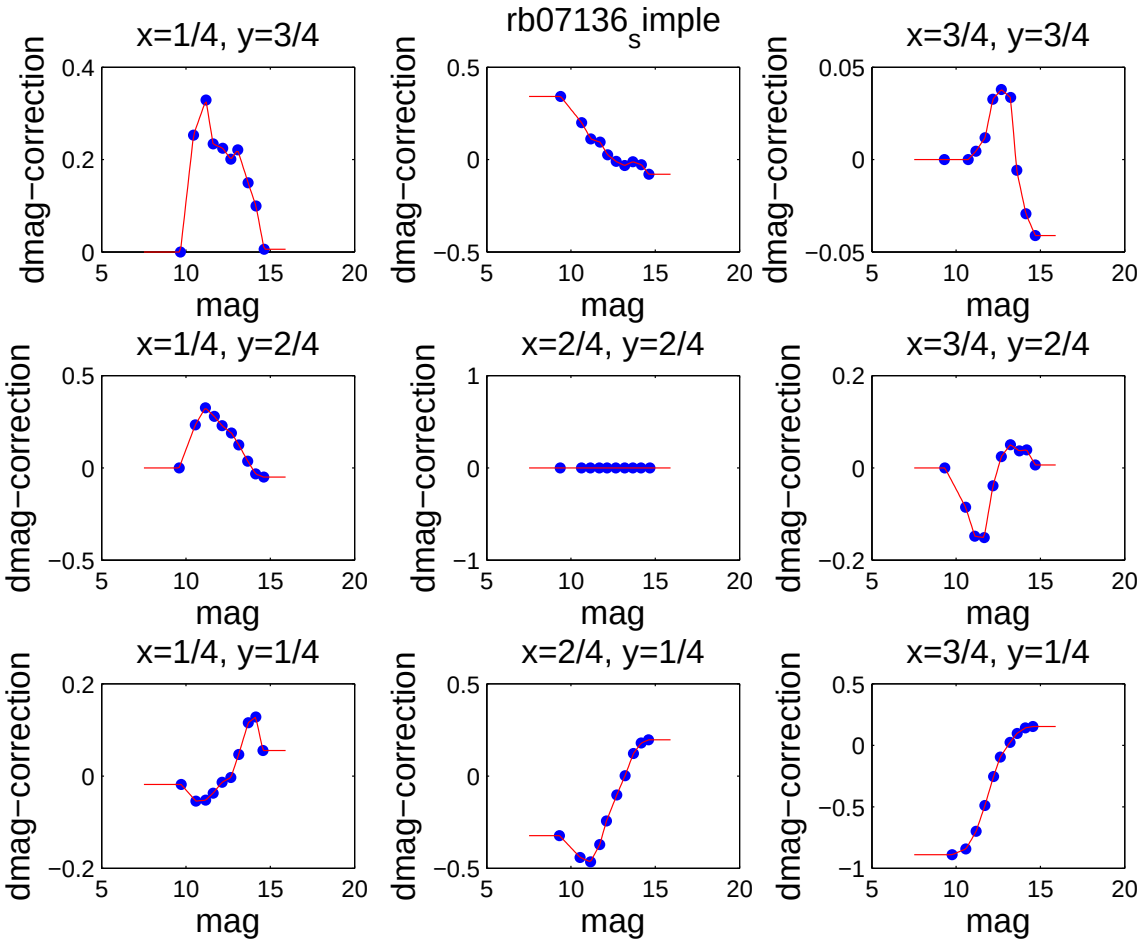

Figure 2.14.— Magnitude residual correction vs magnitude of 9 example spatial bins on plate rh07136. $X = 1/4, Y = 1/4$ means the spatial bin locates at 1/4 of both X and Y axis, $X = 2/4, Y = 2/4$ means the spatial bin locates at the center of the plate, and so on. Positive dmag correction means this must be subtracted to match the catalog value (i.e. stars are being measured as too dim).

bad measurements, which ultimately constrains our ability to find real variables. As shown in Figure 2.15, the second round magnitude-dependent local calibration slightly improves the median light curve rms (upper panel), and greatly reduced the number of bad measurements by one order of magnitude (lower panel). Here we use the number of points in a given light curve of a star that are ≥ 0.4mag brighter than the median magnitude as a measure of the number of "bad" points. In the next section, we describe how real variables are distinguished from this "nburst3" measure of the number of bad points.

As KIC provides $\log(g)$, it is interesting to compare the light curve rms of main sequence stars and giant stars. I selected two groups, a group of main sequence stars with $\log(g) > 4$, and a group of giant stars with $\log(g) < 3$; Only stars with at least 50 good points are used. As shown in Figures 2.16 and 2.17, giant stars show larger light curve rms than main sequence stars. Also note that our overall photometry accuracy as measured by the light curve rms of main sequence stars, is only ~ 0.11 mag, as shown in Figure 2.17.

2.7 Statistical Measurements for Defining Variable Search

We developed a set of statistical measurements for the purpose of selecting variable stars. We first define 'good' points ($AFLAGS == 0$ in the DASCH database; see the DASCH website[1]), excluding the following cases:

[1]http://hea-www.harvard.edu/DASCH/database.php

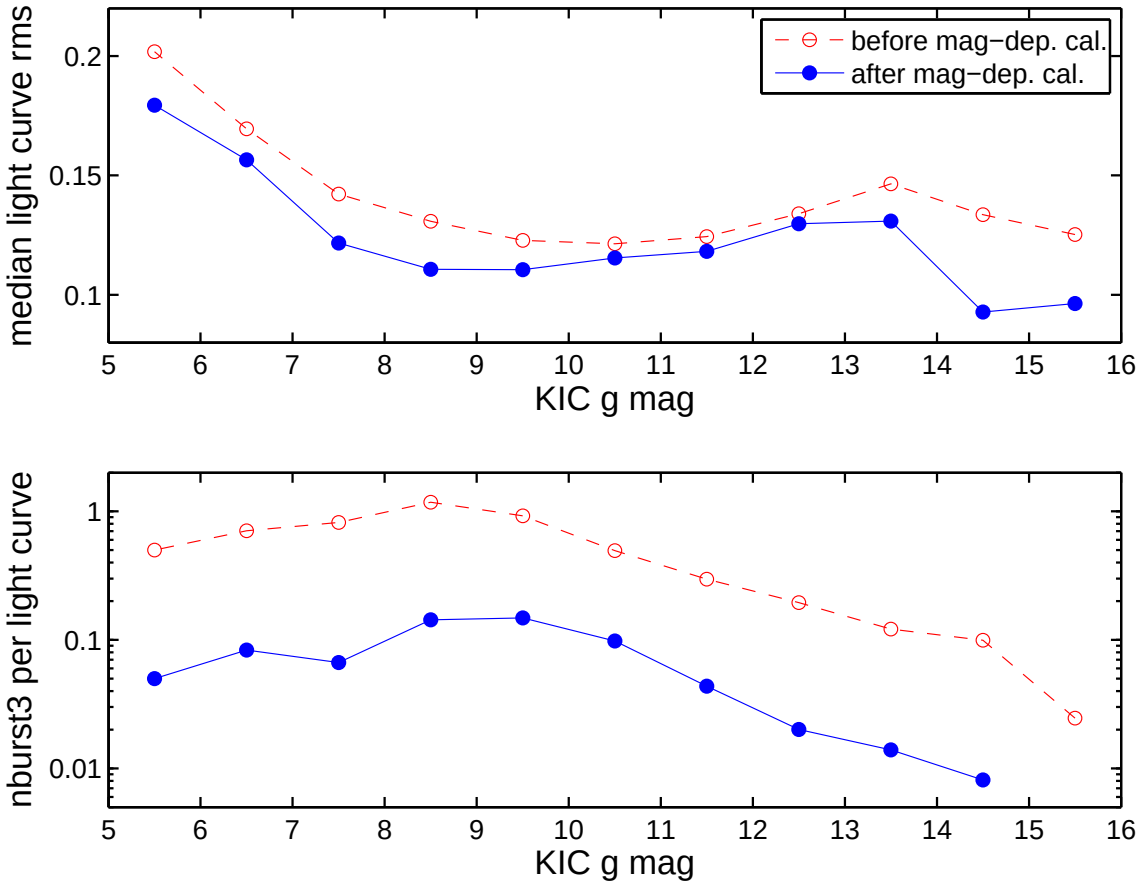

Figure 2.15.— Upper panel: median light curve rms vs KIC g mag in 1 mag bins; Lower panel: number of nburst3 points per light curve vs KIC gmag, where nburst3 points are defined as ≥ 0.4 mag brighter than median mag of a star. The results before magnitude-dependent local calibration are shown in red open circles with dashed lines, and the results after magnitude-dependent local calibration are shown in blue filled circles with solid lines.

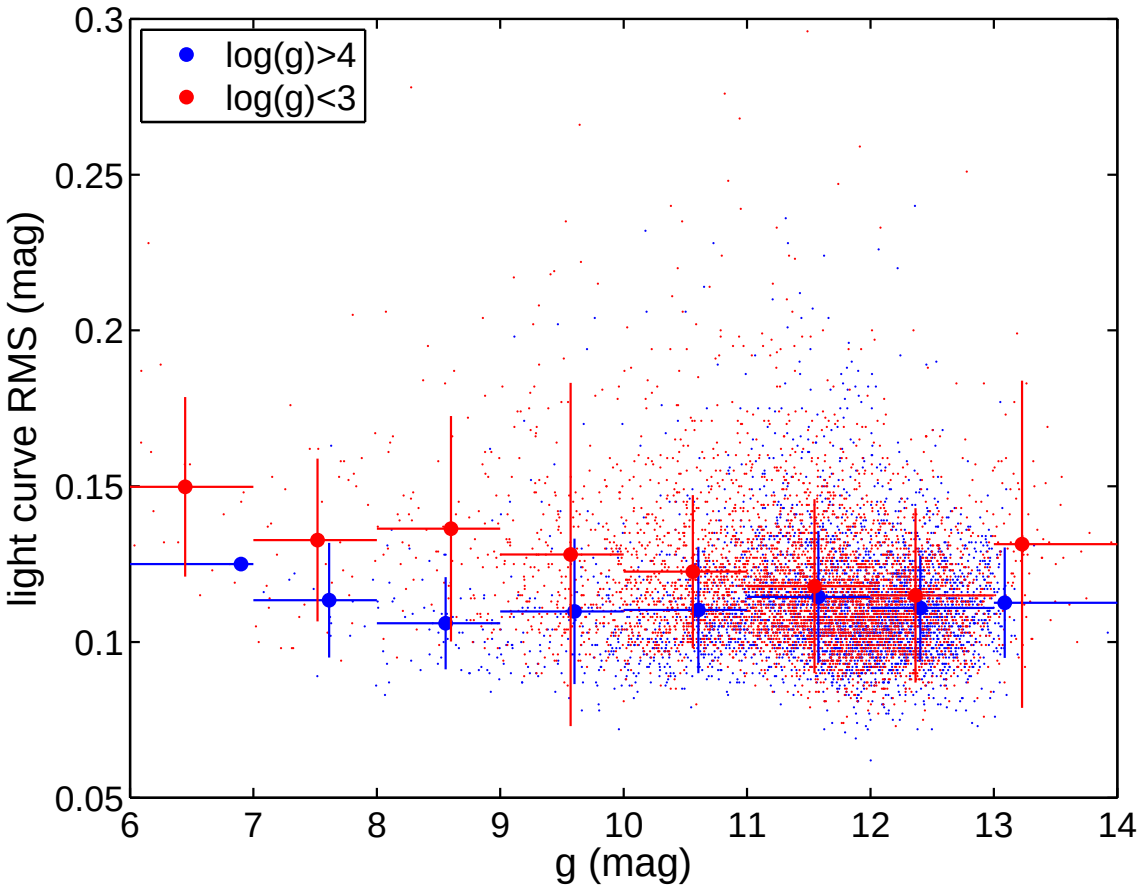

Figure 2.16.— DASCH light curve rms vs KIC g mag for main sequence stars ($\log(g) > 4$; in blue), and giant stars ($\log(g) < 3$; in red). Only stars with at least 50 good points are used. Stars are divided into 1 mag bins. Large solid circles are the mean values, the errorbars along x-axis represent the range of the bin, and the errorbars along y-axis represent the standard deviation of light curve rms in each bin.

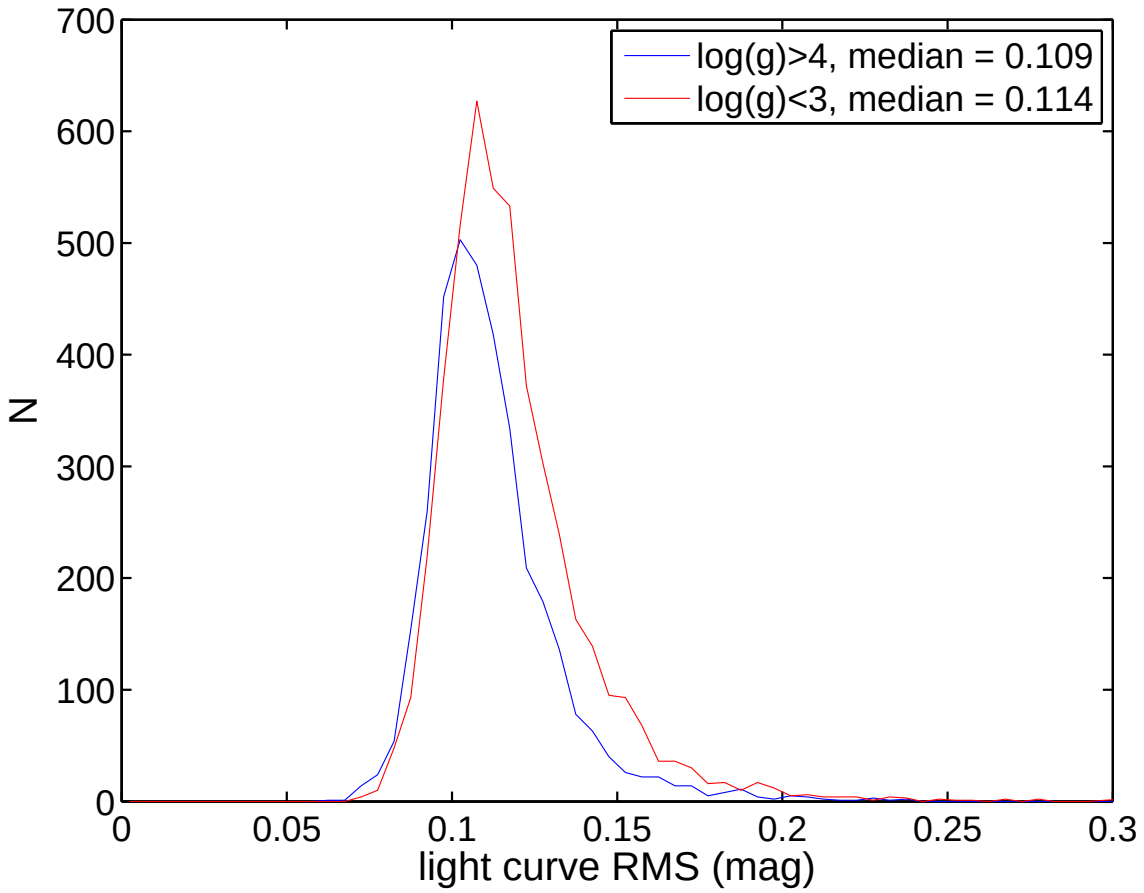

Figure 2.17.— Histogram of DASCH light curve rms for main sequence stars ($\log(g) > 4$; in blue), and giant stars ($\log(g) < 3$; in red). Only stars with at least 50 good points are used.

1. Blended images either flagged by SExtractor or our pipeline (see Chapter 2.3);
2. Images flagged as defects or with a large astrometric position rms (see Chapter 2.4);
3. Images on multiple exposure or Pickering wedge plates (Los et al. 2011);
4. Images in the local bins with extraordinary local bins with anomalously large photometry or astrometry errors, thus likely dubious;
5. Images on plates with uncertain date, or within 23.5 degrees of horizon;
6. Images which are too bright to be calibrated, due to the lack of calibration stars;
7. Images matched with galaxies given by the input catalog (this "galaxy flag" does not eliminate them as candidate variables).

Using these 'good points' (for selecting stellar variables), we then calculate the statistical measurements of each light curve. The measurements used for selecting variables are listed in Table 1, and are described in the following paragraphs. Description of other parameters in the summary table can be found at DASCH website[3].

Two amplitude measurements are calculated. The first one is called *range_local*, which is the difference between the brightest and the faintest points, minus the sum of their errors. The second one is called *range_local*2, which is similar to *range_local*, but after removing the brightest and the faintest points. Light curve rms is calculated after 5σ clipping, and is called *lightcurverms*1 in our database.

We also de-trend the light curves in four different ways and then calculate the rms of the residuals, to look for variables with trends, which have residual rms significantly smaller than their light curve rms. Methods used for de-trending are listed in Table 1. The first two ($lightcurverms2$ and $lightcurverms3$) are sensitive to variables with slow variations over years to decades, while the other two ($lightcurverms4$ and $lightcurverms5$) are sensitive to variables with more than $10 - 15$ adjacent points in the trend.

We use a set of different thresholds to define 'outburst', 'dip', and 'dev' (deviation) points. If there are multiple adjacent points in a 'outburst' or 'dip' in a light curve, then it is more likely to be a true variable. To quantify this, we define parameters ($adjacentburstdip$, $adjacentburstdip2$, and $adjacentburstdip3$) to measure the number of adjacent points in a light curve.

To further exclude possible dubious variables which skipped our blending and defect filters, we calculate a set of correlation measurements, including the correlation coefficients between magnitude and ra, dec, and limiting magnitude. We also calculate the difference between the median DASCH magnitude of 20 deepest plates, and 20 shallowest plates. Blends and noise/defects trends to have significantly higher correlations.

2.8 Summary

In this chapter, I have described the photometry analysis improvements as well as variability search techniques that I have developed to find real variables on the

DASCH digitized images. These developments significantly improved the efficiency of removing dubious measurements, as well as reduced the overall photometric uncertainty. Our variable search starts from the summary table in Chapter 2.7, by selecting candidates with excess variability measurements compared with neighbor stars with similar magnitudes. Details of the algorithms and software for variable searches, and results for the DASCH variables in the Kepler field, are reported in Chapter 7 and Tang et al (in prep.).

Table 2.1: Statistical measurements in the summary table

Parameter	Description
	Light curve amplitude and rms:
range_local	difference between the brightest and the faintest points, minus the sum of their errors
*range_local*2	similar to range_local, but after removing the brightest and the faintest points.
*lightcurverms*1	light curve rms after 4 iterations of 5σ clipping
	rms of light curve residuals after de-trending:
*lightcurverms*2	de-trended using smooth(x,y,0.4, 'lowess')
*lightcurverms*3	de-trended using smooth(y,0.8, 'lowess')
*lightcurverms*4	de-trended using smooth(y,10, 'sgolay')
*lightcurverms*5	de-trended using smooth(y,15, 'loess')
	Number of outburst and dip points:
nburst	number of points ≥ 0.8 mag brighter than the median value
*nburst*2	number of points ≥ 0.5 mag brighter than the median value
*nburst*3	number of points ≥ 0.4 mag brighter than the median value
*nburst*4	number of points $\geq 3\sigma$ brighter than the median value,
	where σ is the median value of photometry uncertainty in the light curve
ndip	number of points ≥ 0.8 mag fainter than the median value
*ndip*2	number of points ≥ 0.5 mag fainter than the median value
*ndip*3	number of points ≥ 0.4 mag fainter than the median value
*ndip*4	number of points $\geq 3\sigma$ fainter than the median value
*ndev*2	number of points $\geq 2\sigma$ brighter or fainter than the median value
*ndev*3	number of points $\geq 3\sigma$ brighter or fainter than the median value
	Adjacent points in 'burst' or 'dip':
adjacentburstdip	a measure of the number of adjacent nburst3/4 and ndip3/4 points
*adjacentburstdip*2	a measure of the number of > 5 adjacent nburst3/4 and ndip3/4 points
*adjacentburstdip*3	a measure of the number of > 7 adjacent nburst3/4 and ndip3/4 points
	Parameters used to remove dubious variables:
magvsracorr	correlation coefficient between light curve magnitude and ra
magvsdeccorr	correlation coefficient between light curve magnitude and dec
magvslimitingcorr	correlation coefficient between light curve magnitude and plate limiting mag
$Malmquist\_factor$	clipped median DASCH magnitude of 20 deepest plates
	− clipped median DASCH magnitude of 20 shallowest plates using 'good' points
$Malmquist\_factorB$	similar to Malmquist_factor but also includes defects, low altitude,
	uncertain date and second quality plates

Chapter 3

Peculiar Long-term K Giant Variables

S. Tang, J. Grindlay, E. Los & S. Laycock *The Astrophysical Journal Letters*, Vol. 710, pp. L77-L81, 2010

Abstract

Here I present the discovery of three unusual long-term variables found in the Digital Access to a Sky Century at Harvard (DASCH) project, with ∼1 magnitude variations in their lightcurves on $\sim 10 - 100$ yr timescales. They are all spectroscopically identified as K2 III giant stars, probably in the thick disk. Their lightcurves do not match any previously measured for known types of variable stars, or any theoretical model reported for red giants, and instead suggest a new dust formation mechanism or the first direct observation of "short" timescale evolution-driven variability. More

theoretical work on the lithium flash near the Red Giant Branch (RGB) bump and the helium shell ignition in the lower Asymptotic Giant Branch (AGB), as well as long term monitoring of K2 III thick disk stars is needed.

3.1 Introduction

The time domain, especially on 10-100 yr timescales, is poorly explored despite its astrophysical importance. The Harvard College Observatory (HCO) maintains a collection of more than 500,000 glass astrophotographic plates from the 1880s to the 1980s, constituting the only continuous record of the whole sky in existence. Every point on the sky has been observed between 500 and 1000 times. This 100 years coverage is a unique resource for studying temporal variations in the universe on ∼10-100 yr timescales. The Digital Access to a Sky Century at Harvard (DASCH) collaboration has developed an ultra-high speed digital plate scanner (Simcoe et al. 2006), and will ultimately enable the full Harvard plate collection to be digitized. We have developed the astrometry and photometry pipeline, and scanned 7000 plates in six different fields. An overview of the DASCH project is presented in Paper I (Grindlay et al. 2009), and the photometry and astrometry pipelines are described in paper II (Laycock et al. 2010) and paper III (Tang et al. in prep).

Here we present the discovery of three unusual long-term variables found in the DASCH scans near the open cluster M44, which showed ∼1 mag dimmings and recoveries on $\sim 10 - 100$ yr timescales in their lightcurves. Such variations are very unusual and haven't been seen in any other common classes. We present their lightcurves and spectra in Chapter 3.2. Discussion on individual objects are in

Chapter 3.3 and summary is in Chapter 3.4.

3.2 Discovery of Three Unusual Variables

3.2.1 Candidate Selection

Three unusual long-term variables presented here were found from $\sim$ 400 variables found on $\sim$ 1200 M44 plates by their peculiar long-term variabilities. These plates cover 5$-$25 degrees on a side with typical limiting magnitudes $14 - 15$ mag (Laycock et al. 2010). There are $\sim 1.2 \times 10^5$ objects with more than 100 magnitude measurements. Details of our variable selection procedure and general properties of variables found in DASCH scans near M44 are described in Tang et al. (in prep.).

3.2.2 DASCH lightcurves

These variables showed unusual $\sim$1 mag dimmings on timescales from 10 to 100 yr in their lightcurves, as shown in black dots in Figure 3.1. DASCH J083038.5+140713 (hereafter J0830; named by its equatorial coordinate in J2000; GSC2.3.2 catalog name N2313102243) declined for 1 mag in a century. It is classified as a 'MISC' variable in ASAS (ASAS J083038+1407.3 Pojmanski 2002) since it became 0.3 mag brighter in V gradually from 2003 to 2007, and then became 0.1 mag fainter from 2008 to 2009. DASCH J075445.9+164141 (hereafter J0754; GSC2.3.2 name N2211330177; ASAS J075446+1641.7) showed a sharp decrease around 1930, and then slowly recovered in 10 years. Another dip was shown around 1892, but

unfortunately we can not constrain the lightcurve profile of the dip due to the lack of data. DASCH J073606.5+211411 (hereafter J0736; GSC2.3.2 name N2230030699; ASAS J073607+2114.2) showed a 1 mag dip from 1930s to 1950s. Both J0754 and J0736 are new variables found with DASCH.

3.2.3 Possible Color Evolution Derived from Plates

The lightcurves of color variations back in time would constrain variable extinction, but is difficult to derive from DASCH. The majority of the Harvard plate collection are blue sensitive plates, and a small fraction of plates used filters to produce red and yellow sensitive measurements with details of wavelength responses unavailable. In order to generate consistent magnitudes, we did color-term fitting for the plates in annular bins to derive the effective color-term C in plates (Laycock et al. 2010), where C of a given plate is defined by

$$m = B + C(B - R),$$

where m is the effective magnitude in the plate, B is the GSC2 B magnitude and R is the GSC2 R magnitude. We then derive the (B-R) color of a given object by comparing its magnitudes with its neighbor stars (with B-R color from GSC2 catalog) in pairs of blue vs red/yellow plates taken from the same night or very close in time (mostly within a week). Each pair of plates gives a (B-R) color of the object at that time. More details are described in Tang et al. (in prep.).

We bin some plate pairs close in time, and plot the color evolution of the three variables by the red open squares in Figure 3.1. The color evolution data are limited mainly by the small number of red and yellow plates usually available. Both J0830

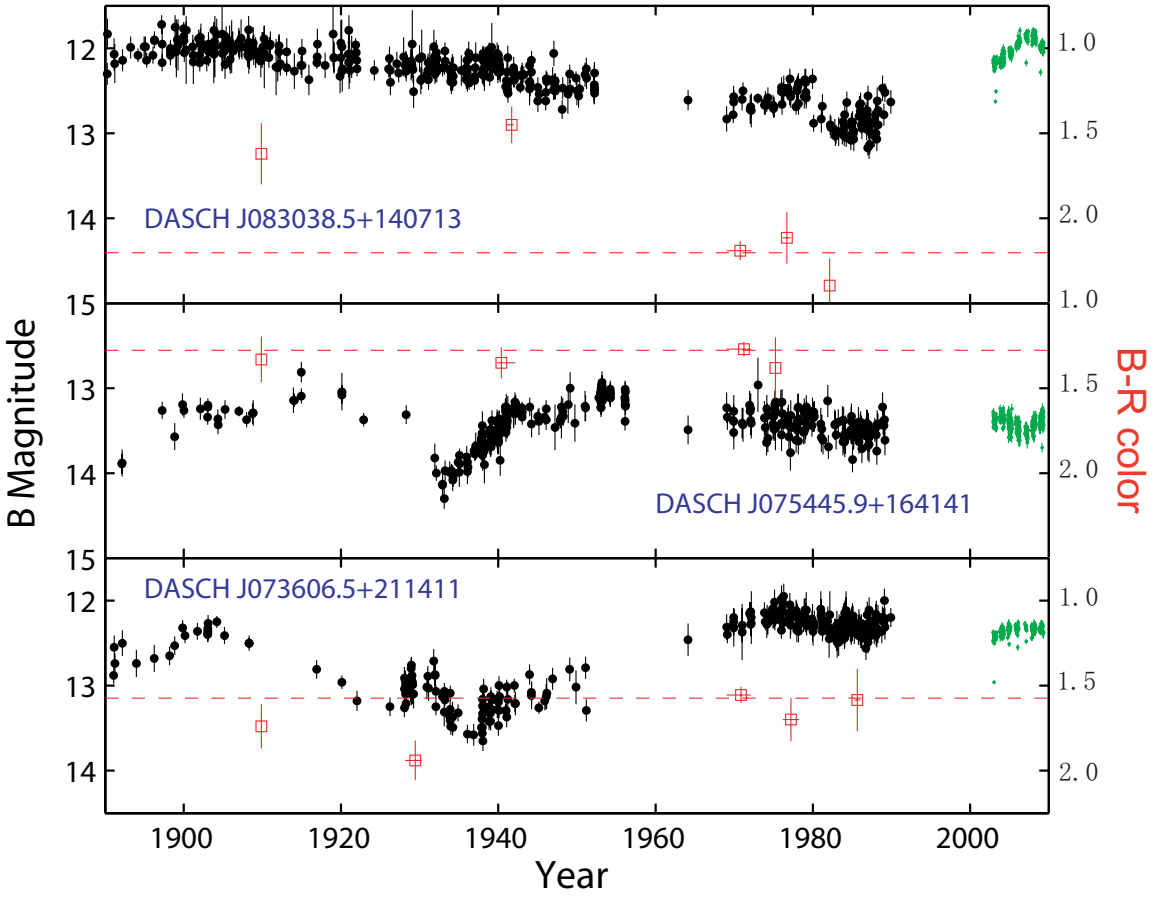

Figure 3.1.— Lightcurves and color evolution of 3 unusual long-term variables which were found in DASCH scans near M44. Black dots with errorbars are the lightcurves from DASCH, small green dots are the lightcurves from ASAS. Since ASAS data are in V band, while DASCH magnitudes are B, we added 1.16 mag to the ASAS V magnitudes in the plots which is the mean B-V value for K2 III stars (Cox 2000). Red open squares are the B-R color derived from plates with y-axis labeled in the right, and red dashed lines mark the weighted mean B-R color values from 1970s to 1980s.

and J0736 are redder when they are fainter, at 7σ and 3σ level, respectively. We didn't detect any color change in J0754, although we do not have red or yellow plates available during its major dimming phase (1930-1940).

3.2.4 Spectroscopic Observations

Spectra were acquired with FAST spectrograph on the 1.5 m Tillinghast reflector telescope at the F. L. Whipple Observatory (FLWO) and GMOS long-slit spectroscopy blue channel on Gemini North. They are wavelength-calibrated with standard packages, and are shown in Figures 3.2 and 3.3. According to their spectra, they are all K2-type stars. By comparing the region between $4900 - 5200$ Å with FAST spectra of several K2 standards with different luminosity classes, we found all of them are giants (luminosity class III; Estimated uncertainties in luminosity class are II-IV. Luminosity class I and V are ruled out). We estimated metallicities [Fe/H]$\sim -0.3 \pm 0.3$ for J0830, and [Fe/H]$\sim -0.9 \pm 0.4$ for J0754 and J0736, by comparing with FAST spectra of several standard K giant stars with known metalicities (Faber et al. 1985). We also found that J0830 and J0754 do not show velocity changes within measurement errors (~ 8 km/s), while J0736 showed significant radial velocity changes in three different epochs, i.e. 11 ± 6 km/s on Feb 4th, -18 ± 6 km/s on Feb 19th, and 22 ± 6 km/s on April 18th, 2009, and is then probably in a close binary.

As shown in Figure 3.3, all three variables show Ca II K and H emission lines in the absorption core, indicating the presence of active chromospheres. Ca II K and H emission lines are common among cool dwarf and evolved stars, signaling the

magnetic dynamo activity in chromospheres (Kraft 1967; Soderblom 1983; Dupree & Smith 1995). Their fluxes correlate with stellar rotational velocities (see Strassmeier et al. 1994; Pasquini et al. 2000, and references therein). Followed (Linsky et al. 1979), assuming $V - R = 0.84$ for K2 III stars (Cox 2000), we calculated the net chromospheric loss in the K lines, which are $\log \mathcal{F}'(K) = 6.35$, 6.13 and 5.98, indicating rotation velocities about 40 km/s, 25 km/s and 16 km/s (Strassmeier et al. 1994, the uncertainty is large though, about 0.5 dex), for J0830, J0754 and J0736, respectively.

3.2.5 Occurrence Fraction of K2 III Long-term Erratic Variables

The plates we analyzed are centered around the open cluster M44. The coverage decreases when the region is farther away from the center of M44. There is roughly a 40×40 deg^2 region with good coverage (i.e. more than 100 scans). From Keplercam photometry of a 3.2 deg^2 region near M44, we estimate there are about 4000-6000 stars with $12 < B < 13.5$ and $0.85 < g - r < 1.02$ in this 40×40 deg^2 region. If we assume that objects with $0.85 < g - r < 1.02$ are K2 III stars (Covey et al. 2007; Smith et al. 2002, note that some dwarfs and supergiants are also included, but there are many more giants than supergiants, and at 12-13 magnitude, we are seeing more giants than dwarfs), then the event rate of such long-term variables among K2 III stars is about $3/5000 \sim 0.06\%$.

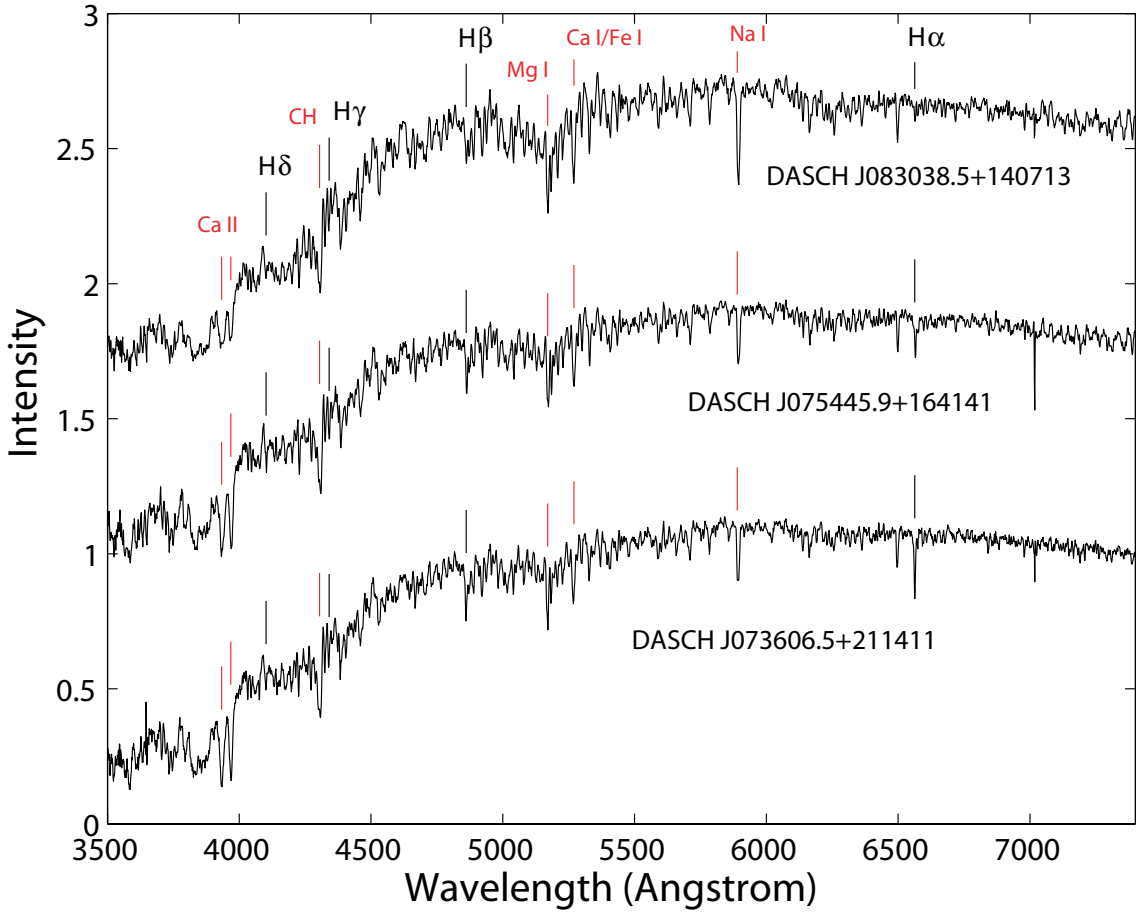

Figure 3.2.— FAST 300 grating spectra of the 3 erratic variables with lightcurves shown in Figure 3.1. All of them are K2 III stars. Spectral resolution is about 7Å.

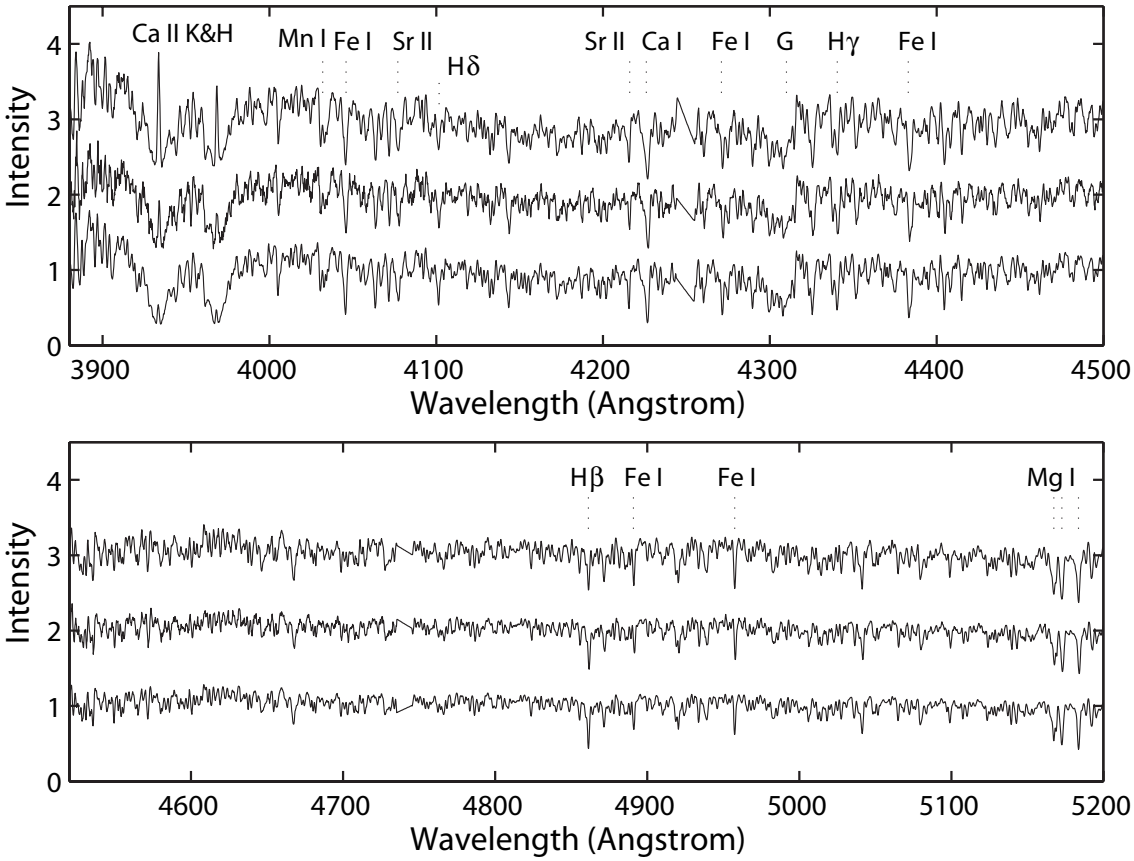

Figure 3.3.— Gemini B1200 grating spectra of the 3 erratic variables. From top to bottom are spectra of J0830, J0754, and J0736, respectively. Continuum are removed by a sixth-order polynomial fit. Spectral resolution is about 1.2 Å ($R = 3744$).

3.3 Discussion of Individual Objects

Table 1 lists the galactic coordinates, GSC2.3.2 B-R colors, GSC B, ASAS V and 2MASS JHK magnitudes, [Fe/H], proper motions, radial velocities, distances, and galactic velocities for the three variables. J0830 and J0754 have high proper motions ($>$ 10 mas/yr), while J0736 has no proper motion within its error of 2 mas/yr. The 3 stars are about $500 - 800$ pc above the galactic plane. J0830 and J0754 have velocities about 100 km/s, while J0736 probably has smaller velocity $<$ 30 km/s. Our spectra indicate metallicities [Fe/H]~ -1 to 0. They are most probably thick disk giants (Carollo et al. 2010). The 2MASS $H - K$ color of J0830 is 0.27, which is redder than $H - K = 0.04$ expected for a K2 giant (Covey et al. 2007). Note that J0830 also showed large reddening in the 1970s and 1980s in our plates during its dimming, as shown in Figure 3.1. As K2 III stars with [Fe/H]~ -1 to 0, the 3 erratic variables could be on the Red Giant Branch (RGB), but not near the tip, on the Horizontal Branch (HB), or early asymptotic giant branch (AGB).

Timescales of 10-100 year are too long to be pulsations driven by ionization (Percy 2007), or convective instabilities which have timescales in the order of a year for a K giant (Prialnik 2000). The lightcurves of these 3 erratic variables look somewhat like R Coronae Borealis (RCB) stars. RCB stars are rare, hydrogen deficient, carbon-rich supergiants which undergo large amplitude ($3 - 8$ mag) fading events lasting weeks to a few years as dust condensates to block the light along the line of sight (Clayton 1996). Our variables share some of these typical RCB lightcurve features, and the lightcurve of J0830 is similar to some hot ($T \sim 20000$ K) RCB stars (De Marco et al. 2002). Dust obscuration events have also been observed

in some other carbon rich stars. Whitelock et al. (2006) found about one-third of the Carbon-rich Miras and other AGB stars undergo dimming episodes.

However, all of the three variables presented here are very different from normal RCB stars in the following aspects, and therefore are not RCB stars (or any other type of carbon-rich AGB stars): They are not post-AGB supergiants like RCB stars (Alcock et al. 2001); much cooler than most RCBs; have much longer variability timescales and much smaller amplitudes than average RCB stars; have no strong carbon absorption bands, and have strong hydrogen absorption lines. J0830 has weaker Hα absorption which might due to the chromospheric emission in the core, since the Ca II emission lines are very strong in J0830 and Hα emission is usually strongly correlated with Ca II lines (Cincunegui et al. 2007).

Some symbiotic stars also show irregular long-term variations (see e.g. Sokoloski et al. 2006; Skopal 2008). However, there is no symbiotic signature in our variables, such as nebula emission lines or combination spectra. There is no common model that works well for these 3 erratic variables, as we discuss below.

3.3.1 J0830

[1] The first possible model is dimming caused by obscuration of dust shells ejected from the star, which is consistent with our observation that the object became redder when it was fainter and its redder 2MASS $H-K$ color. However, how to produce and maintain the dust for such a long time is not clear. For RGB stars,

[1]Some of the models in this subChapter 3.may also apply to J0754 and J0736

significant mass loss occurs only at the very tip (Origlia et al. 2002), which is much too luminous for the three erratic variables. Bedding et al. (2002) found a 5-yr dimming event in the oxygen-rich, Mira-like variable L_2 Pup, likely due to absorption by a dust shell containing silicates. L_2 Pup is located near the tip of the AGB, and thus has high mass-loss rate (5×10^{-7} $M_\odot$ yr $^{-1}$), which if applied to our K2 III stars would require they have low metallicity and be halo stars. Tsuji (2009) found excess absorption in CO lines of Arcturus (K1.5III), and proposed it might be caused by the formation of molecular clouds in the outer atmosphere. Arcturus only shows low amplitude optical variations of a few percent (Bedding 2000) and thus the absorption due to such molecular clouds is not enough to account for the 1 magnitude dimming events in the three erratic variables.

A second possible model, is the lithium flash near the RGB luminosity bump (Palacios et al. 2001), which proposed that rotation induced mixing leads to a thin and unstable lithium burning shell, which leads to an increase of nuclear luminosity, and mass loss which might account for the formation of a dust shell around the star and thus the reddening of the star. All of our 3 variables are chromospherically active and probably fast rotators, which fit to this model. However, the variation timescale and amplitude of surface luminosity in this model is unknown.

A third possible model, which may be the most plausible one, is the evolution phase when the star is leaving the HB and beginning to ascend the AGB, at the point that helium is exhausted in the core and helium burning is ignited in a surrounding shell. This could apply to the point L in Figures 2 and 4 of Sackmann et al. (1993). We plotted the evolutionary tracks for $[Z = 0.008, Y = 0.25]$ ([Fe/H]$\sim$-0.4 if assume the same composition as the Sun) from Girardi et al. (2000), and found

stars with mass $0.8 - 1.2\ M_{\odot}$ are crossing this evolutionary phase near $T \sim 4400$ K and $L \sim 10^{2.2} L_{\odot}$ (which is the temperature and luminosity for K2 III stars Cox 2000). The ignition of the helium-burning shell causes expansion and makes the hydrogen-burning shell expand and cool, which makes the surface luminosity decline and the color redden, and then recover later. If this process is similar to thermal pulses in He-burning shell of later AGB stars, then first the surface luminosity decreases by a factor of 2 over 50-100 yr, and then increases by a factor of 2 over 200 yr (Mowlavi 1999), which is roughly consistent with J0830 and J0736. More theoretical study and simulations of this evolution phase may clarify the nature of our variables.

Two other interesting observations might be related to the three erratic variables. Edmonds & Gilliland (1996, hereafter EG96) found a new class of variable stars in K giants with amplitudes $5 - 15$ mmag and periods of days clumped in the color-magnitude diagram with B-V=1.1-1.2, which is the location of K2 III stars. They lie on both the AGB and the RGB. Bedin et al. (2000) found a 'heap' in the luminosity function which is about 1.4 magnitude brighter than the RGB bump, and in the case of 47 Tuc, the heap is in a similar location on the RGB to the variables found by EG96. The heap and the new class variables are not well understood yet (see e.g. Salaris et al. 2002), and it is surprising that they have similar color and luminosity class as our erratic variables, which show much longer timescale and larger amplitude variations. There might be some intrinsic link between the objects in the three independent observations. In Figure 4 of Sackmann et al. (1993), the location of the He-shell ignition is just about 0.6 dex, i.e. 1.5 magnitude, brighter than the RGB bump, consistent with the luminosity of K giant variables in EG96.

3.3.2 J0754

This star is not yet included in any known variable catalogs. The sharper decline and slower recovery are similar to what is seen in RCB stars. It might be puffing off outer layers at irregular intervals, which blocks the light from the star.

3.3.3 J0736

This variable is probably a binary. Given its possible orbital period of $\sim\leq$ 15 days ($\sim$ 30 km/s change in radial velocities from Feb. 4 th to Feb. 19th) and its Ca K and H line emission, it might share some properties in common with RS CVn systems. It is not yet included in any known variable catalogs. Similar to J0830 and J0736, it might be puffing off out layers which blocks the light from the star, as supported by the measured reddening during dimming; it might also be lithium flash near the RGB bump, or the He-shell ignition in the lower AGB, as discussed in Chapter 3.3.1.

3.4 Summary

We have found three very interesting long-term variables, which do not resemble known classes of variables previously reported. We found no model reported for red giants which could explain both their timescales and amplitudes. The underlying causes of their 10-100 yr variations might be related to evolutionary nuclear shell-burning instability and/or variable dust obscuration. Higher resolution spectra and Infra-Red observation in future are needed to constrain surface gravity, mass, and possible dust properties. More theoretical work on the lithium flash near the

Table 3.1: List of the three unusual long-term variables found in DASCH.

DASCH Name	Gal. coord.		GSC[a]	GSC[a]	ASAS[b]	2MASS[c]			[Fe/H]	PMRA[d]	PMDec[d]	v_r[e]	D[f]	u[g]	v[g]	w[g]
	l	b	B	B-R	V	J	H	K		mas/yr	mas/yr	km/s	kpc			
J083038.5+140713	211	28	12.90	1.40	10.85	8.82	8.20	7.93	-0.3 ± 0.3	9.0	-10.8	0 ± 8	1.8	-82	-79	37
J075445.9+164141	205	21	13.30	1.61	12.24	10.42	9.83	9.70	-0.9 ± 0.4	-3.0	-10.2	22 ± 8	2.1	-2	-81	-48
J073606.5+211411	198	19	12.66	1.29	11.19	9.30	8.78	8.67	-0.9 ± 0.4	-1.8	-2.3	-[e]	1.6	-	-	-

[a]From GSC2.3.2 catalog (Lasker et al. 1990).

[b]Median ASAS V magnitudes (Pojmanski 2002).

[c]2MASS J, H and K magnitudes with typical uncertainty about 0.02 mag (Skrutskie et al. 2006).

[d]Proper motion in RA and Dec, from Tycho-2 catalog with typical uncertainty about 2 mas/yr (Høg et al. 2000).

[e]Radial velocity. The radial velocity of J0736 is variable.

[f]Distances of the objects assuming absolute B magnitude of 1.66 for K2 III stars (Cox 2000).

[g]Galactic space velocity in km/s, corrected to the local standard of rest. u - positive toward the Galactic anti-center; v - positive in the direction of Galactic rotation; w - positive toward the North Galactic Pole. We didn't estimate the Galactic space velocity for J0736, due to the uncertain nature of its radial velocity and its small proper motion velocity which is consistent with zero within uncertainty.

RGB bump and the helium shell ignition in the AGB, including surface luminosity variation and possible dust formation, will be helpful to understand their nature. As most likely thick disk stars with [Fe/H]~ -0.9 to -0.3, they are likely to have ages $8 - 16$ Gyr (Bensby et al. 2004), and therefore likely to be $\sim 0.8 - 1.1\ M_{\odot}$ (Girardi et al. 2000). If all 3 stars are ~ 1 $M_{\odot}$ for which the RGB is nearly vertical, their similar spectral type is expected. The evolutionary timescales of variations in models 2 and 3 (Chapter 3.3.1) are both in the range $\sim 200 - 1000$ yr. A ~ 1 $M_{\odot}$ star with Z=0.004 to 0.008 ([Fe/H]~ -0.7 to -0.4) spends $\sim 10^{7.2}$ yr during RGB and $\sim 10^{6.4}$ yr during AGB phases as K2 giants (T$\sim$4300 to 4500 K Cox 2000;

Girardi et al. 2000). Therefore, the predicted rate of such erratic variables among K2 giants is $\sim 600/10^{7.2} \sim 0.004\%$. This is ~ 15 times smaller than our estimated occurrence fraction of our K2 III variables (0.06%), indicating other mechanisms beyond the evolutionary models we discussed in the paper might be relevant.

We did a general search for long-term variables and it turned out surprisingly that three most interesting objects with drops in timescales $\sim 10 - 100$ year are all K2 giants. Is this a coincidence or are thick disk K2 giants special? Due to the small size of the sample, we cannot answer the question for sure yet. We are working on a larger sample of similar long-term variables over more plates, and hopefully we will have more knowledge about the demographic very soon. We note that ~ 1200 plates covering M44 field are only $\sim 0.2\%$ of the whole Harvard plate collection, and there is huge potential to find more interesting objects and new classes of variables.

Stellar evolution proceeds on astronomical, not human, timescales (except for pulsations and eruptive events). However, evolution-driven changes on ~ 100 yr timescales, such as shell burning flashes and core helium flash in giants, are rare but can be observed with the DASCH database with both long-term data coverage and very large stellar samples. Note that AAVSO also provides invaluable long-term data, but mostly for a few thousand much brighter sources, see `http://www.aavso.org`. Instead of waiting for another century to gather data to study 100-yr variability, we could make it available for bright objects (B<15 mag) in several years from DASCH, provided support for this full digitization scanning can be found.

Chapter 4

DASCH on KU Cyg: A ∼5 Year Dust Accretion Event in ∼1900

S. Tang, J. Grindlay, E. Los & M. Servillat *The Astrophysical Journal*, Vol. 738, pp. 7-10, 2011

Abstract

KU Cyg is an eclipsing binary consisting of a F-type star accreting through a large accretion disk from a K5III red giant. Here I present the discovery of a 5-yr dip around 1900 found from its 100 yr DASCH light curve. It showed a ~ 0.5 mag slow fading from 1899 to 1903, and brightened back around 1904 on a relatively shorter timescale. The light curve shape of the $1899 - 1904$ fading-brightening event differs from the dust production and dispersion process observed in R Coronae Borealis (RCB) stars, which usually has a faster fading and slower recovery, and for KU Cyg

is probably related to the accretion disk surrounding the F star. The slow fading in KU Cyg is probably caused by increases in dust extinction in the disk, and the subsequent quick brightening may be due to the evaporation of dust transported inwards through the disk. The extinction excess which caused the fading may arise from increased mass transfer rate in the system, or from dust clump ejections from the K giant.

4.1 Introduction

KU Cyg is an Algol-type eclipsing binary system with an orbital period, P= 38.4 days (Popper 1964, 1965). The gainer is a 3.85 $M_{\odot}$ F−type star with a near main-sequence surface gravity, but is over-massive for its luminosity, and is surrounded by a large accretion disk (Olson et al. 1995). The donor is a 0.48 $M_{\odot}$ K5III red giant which probably fills its Roche Lobe (Olson et al. 1995). The accretion disk around the gainer led to abnormally wide secondary eclipses, and is found to be large (close to or filling the primary star Roche lobe), thick, dusty, and probably eccentric (Olson 1988; Zola 1992; Smak & Plavec 1997). Double-peaked Hα emission is visible at all orbital phases with chaotic fluctuations, which strongly supports the presence of a disk (Olson 1991; Olson & Etzel 1995). The inclination of the binary orbital plane is $\sim 86 - 86.5$ degree (Olson et al. 1995; Smak & Plavec 1997).

Here I report the discovery of a 5-yr dip in brightness of KU Cyg between 1899 and 1904 as determined from the Digital Access to a Sky Century at Harvard (DASCH) project. DASCH is a project to digitize and analyze the scientific data contained in the $\sim 530,000$ Harvard College Observatory (HCO) plates taken

between the 1880s and 1990s, which is a unique resource for studying temporal variations in the universe on $\sim 10-100$ yr timescales (Grindlay et al. 2009). We have developed the astrometry and photometry pipeline, scanned $\sim$ 13,000 plates in several selected fields (Laycock et al. 2010; Los et al. 2011; Servillat et al. 2011, Tang et al. in prep.), and discovered new types of variable stars (e.g. Tang et al. 2010). We present the DASCH light curve of KU Cyg in Chapter 4.2. Discussion is given in Chapter 4.3.

4.2 DASCH light curve

The Kepler field is one of our primary target fields for our initial scanning, selected in order to take advantage of the unprecedented Kepler data on short timescales (Borucki et al. 2010) which complements DASCH data on long timescales. We have scanned $\sim$ 3000 plates in or covering part of the Kepler field. These plates cover $5-25$ degrees on a side with typical limiting magnitudes $13-15$ mag, and are mostly blue sensitive (Tang et al. in prep.). KU Cyg (RA=20:12:45.11, Dec=+47:23:41.4, J2000) is a few degrees outside the Kepler field of view, but fortunately, is still covered by the Kepler Input Catalog (KIC Brown et al. 2011). The KIC ID of KU Cyg is 10311340 with $g = 11.675$ and $g-r = 0.622$. We used the KIC for photometric calibration, and the measurements are calibrated to the g band. We have 827 plates taken from 1890 to 1990 with good calibrations covering KU Cyg, which yield 800 detections and 27 upper limits. The typical photometric uncertainty is $\sim 0.1-0.15$ mag. Each measurement is locally re-calibrated using 38 clean neighbor stars with similar magnitudes and colors ($g = 10.5-13$ and $0.2 < g-r < 1$) within 20 arcmin.

More details on DASCH photometry and calibration are described in (Laycock et al. 2010) and Tang et al. (in prep.).

The resulting DASCH light curve of KU Cyg is shown in Figure 4.1. The upper panel shows the whole light curve from 1890 to 1990. The lower-left panel shows the light curve from 1897 to 1906 to better display the fading-brightening event. The lower-right panel shows the light curve from 1980 to 1990 binned in 1 year increments, where error bars represent the standard deviation of the mean, to better illustrate its yearly variability (primary eclipses are excluded; the secondary eclipses are broad and shallow and thus not excluded). Black dots with errorbars are DASCH measurements, and blue arrows (colors in electronic version) are upper limits. Red circles mark primary eclipses with orbital phase $0.965 - 0.035$, using the ephemeris from Olson (1988) of $\mathtt{JD} = 2433884.840 + 38.439484\mathtt{E}$. In all three panels, blue dashed lines show a constant magnitude of 11.53, which is the median magnitude of KU Cyg from 1910 to 1990 with phases $0.05 - 0.95$ (excluding the primary eclipses). All the measurements and upper limits fainter than 12.5 mag (i.e. 1 mag below its normal high state) were taken during the primary eclipses, well in agreement with the ephemeris given in Olson (1988).

The most striking feature in the light curve is the 5-year dip around 1900, as shown in Figure 4.1. KU Cyg started to show fading around 1899, and dropped from ~ 11.4 mag (as before 1895) to ~ 12.0 mag in $1902 - 1903$, and then in about half a year, it brightened to ~ 11.5 mag in early 1903. After that, it showed fluctuations between $11.5 - 12.0$ mag from 1903 to 1905.

KU Cyg is also variable on year-timescales outside primary eclipses with

fluctuations ~ 0.1 mag, as shown in the yearly binned light curve in the lower-right panel of Figure 4.1. Note there is a ~ 0.15 mag brightening bump around 1984, which has been discovered by Olson (1988), and is verified by DASCH. There seems to be a slight trend of $0.1 - 0.2$ mag brightening from 1910 to 1990, however, given our systematic uncertainty over 100 years of ~ 0.1 mag (Tang et al. in prep.), it is not convincing. Compared with its ~ 2000 neighbors with $g = 11 - 12$ within 5 degrees, the brightening trend from 1910 to 1990 in KU Cyg is only at the 2σ level. We have also visually checked the light curves of all these neighbors, and none of them showed similar dip around 1900 as KU Cyg, which further supports that the 5-year dip is real.

The light curve of KU Cyg, folded on the 38.439484 days period (Olson 1988) is shown in Figure 4.2, with the upper panel for $1910 - 1990$ and the lower panel for $1890 - 1910$. Black dots are DASCH measurements, and blue arrows are upper limits. Both the deep primary eclipse and the shallow, wide secondary eclipse can be seen in the folded light curve from 1910 to 1990. KU Cyg showed larger variability on non-eclipse phases $(0.05 - 0.95)$ during $1890 - 1910$ than during $1910 - 1990$, with rms of 0.20 mag and 0.15 mag, respectively. The 0.15 mag rms on non-eclipse phases during $1910 - 1990$ further illustrates that our typical photometric errors are below 0.15 mag. Note that our coverage during eclipse phases (Figure 4.2) would allow a period measurement precision of $dP \sim P^2 dN/T \sim 4 \times 10^{-4}$ days for a phase uncertainty $dN \sim 0.01$ over the $T \sim 100$ years duration and so it is not possible to further refine the binary period given by Olson (1988).

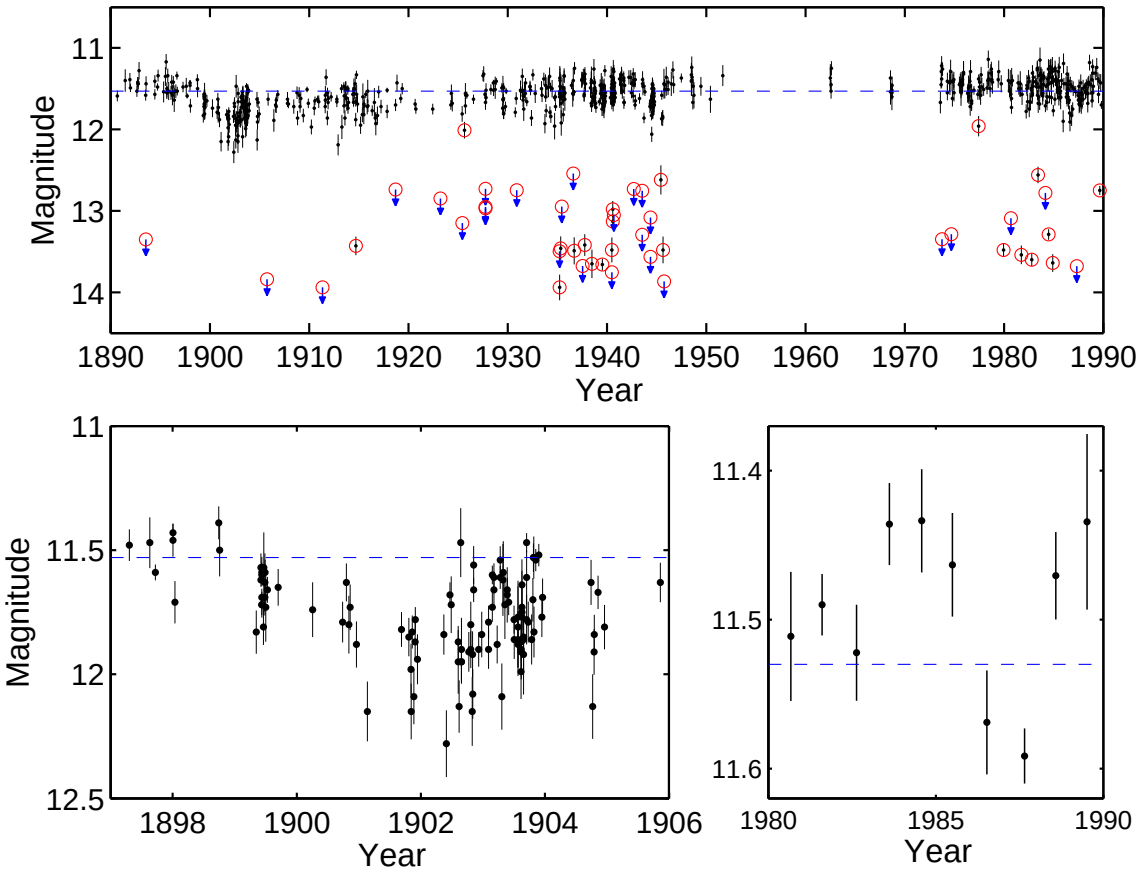

Figure 4.1.— DASCH Light curve of KU Cyg. The upper panel shows the whole light curve from 1890 to 1990. The lower-left panel shows the light curve from 1897 to 1906 for the dimming event, and the lower-right panel shows the light curve from 1980 to 1990 binned in 1 year increments with error bars showing the standard deviation of the mean (primary eclipses excluded). Black dots with errorbars are DASCH measurements calibrated to g band, and blue arrows are upper limits. Red circles mark primary eclipses with orbital phase $0.965 - 0.035$. In all three panels, blue dashed lines show a constant magnitude of 11.53, which is the median magnitude of KU Cyg from 1910 to 1990 with phases $0.05 - 0.95$ (excluding the primary eclipses).

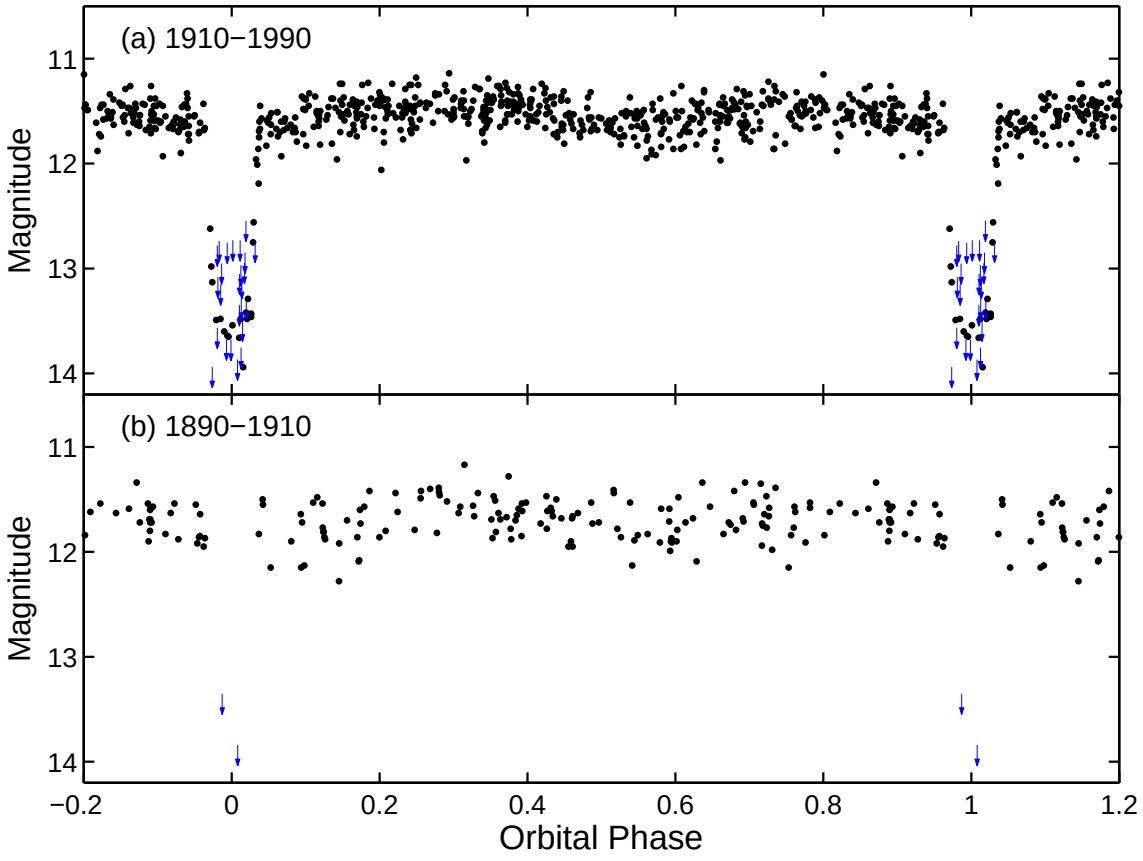

Figure 4.2.— DASCH folded light curve of KU Cyg, using the adopted ephemeris from Olson (1988). The upper panel shows the folded light curve from 1910 to 1990, and the lower panel shows the folded light curve from 1890 to 1910. Black dots are DASCH measurements, and blue arrows are upper limits.

4.3 Discussion

Since the orbital period of KU Cyg is $\sim$ 38.4 days, the $\sim$ 5-yr fading-brightening event we found from 1899 to 1904 must come from sources other than eclipses. Our plates are blue sensitive, where the flux is dominated by the F star; This is also illustrated in the folded light curve, where there are up to 2.4 mag decreases during the primary eclipses, which means the K5III giant contributes $< 10\%$ of the total flux. Therefore, the $\sim$ 0.5 mag dimming must be related to the F star and its accretion disk.

4.3.1 Higher mass transfer rate?

The simplest explanation of the fading-brightening event, perhaps, is increasing disk extinction of the F star arising from increasing mass transfer rate. RX Cas is an edge-on mass-transfering eclipsing binary system (P = 32.3 days), similar to KU Cyg. Kriz et al. (1980) suggested in RX Cas that when the rate of mass transfer increases, the disk density and consequently optical depth increases, leading to attenuation of the central star and resulting in fading in its light curve. Similar effects have been observed in Be shell stars (edge-on Be stars with high $v \sin i$), where fadings are seen in mass ejection events (see e.g. Hubert & Floquet 1998; Gutierrez-Soto et al. 2008).

It has been found that the accretion disk surrounding the F star in KU Cyg is thick and dusty, with dust to gas ratio $\sim 10^{-6}$, and a total disk mass $\sim 10^{-8} - 10^{-5}\ M_{\odot}$ (Olson 1988; Smak & Plavec 1997). Smak & Plavec (1997)

estimated an extinction of 1.3 mag in V of the F star by the disk, with ~ 0.75 mag extinction due to the full obscuration of about half of the F star by the disk, and the remaining ~ 0.55 mag due to the absorption in the disk atmosphere. To cause a $0.5 - 0.6$ mag dimming observed in KU Cyg, and assuming the same gas-to-dust ratio, the disk mass excess would be on the order of the accretion disk mass, i.e. $\sim 10^{-8} - 10^{-5}\ M_{\odot}$. The timescale of accretion in the disk of KU Cyg is a few years (Smak & Plavec 1997). If we assume a $\sim 10^{-8} - 10^{-5}\ M_{\odot}$ ejection from the K5III star arrives at the outer region of the accretion disk around 1899, during the next few years, the ejected mass would move inwards, so that dust grains would be levitated above the disk by radiation pressure and photophoresis (see e.g. Vinković 2009; Wurm & Haack 2009). This would result in an increased covering factor and a larger extinction.

Later, when the dust moves to smaller radii in the disk and gets closer to the F star, it should reach the evaporation temperature and most dust particles at high scale heights would evaporate, leading to a brightening. Additionally, some of the dust particles may be transported outwards (Takeuchi & Lin 2003; Ciesla 2007), cool down to condensate, and disperse, leading to more extinction. Moreover, when the clump of excess mass is accreted onto the F star, the energy release on the boundary layer also leads to a brightening, as discussed in Olson (1988) and Smak & Plavec (1997) to explain the ~ 0.2 mag brightening bump around 1984. The above three processes may together produce the fluctuations from 1903 to 1905 in KU Cyg.

4.3.2 Higher dust to gas ratio?

An alternative explanation is that the dimming is caused by dust excess rather than mass excess, i.e., higher dust to gas ratio, in the disk surrounding the F star. In a similar way to the above discussion, when the dust clumps move inwards and are levitated above the disk, extinction of the F star becomes larger, and the system becomes fainter. The system brightens when the dust grains move closer to the F star and evaporate.

However, where the dust excess comes from is a challenging question. It might arise from clumps of dusty gas ejected from the K5III giant. We have discovered a group of K2III giants with ~ 1 mag dimming over $10 - 100$ years, which do not match any known classes of variables (Tang et al. 2010). We suggested that the dimming might be caused by dust extinction in a certain evolution stage of K giants, though how the dust gets ejected is still unclear. The dimming of KU Cyg in 1899 might arise from similar dust ejection processes in the K5III giant. The dust clumps then move to the accretion disk around the F star through Roche Lobe overflow.

4.3.3 Summary

In summary, the 5-year dip in brightness of KU Cyg observed around 1900 is unique in the way that it faded slowly and brightened relatively quickly, which is contrary to the dust production and dispersion process observed in RCB stars, where it usually takes longer for the dust to disperse and thus longer for the star to brighten (Clayton 1996). This fading-brightening event in KU Cyg is probably related to the accretion disk surrounding the F star, which provides interesting clue for the study

of dust confinement, levitation and evaporation in an accretion disk.

Chapter 5

DASCH Discovery of A Possible Nova-like Outburst in A Peculiar Symbiotic Binary

S. Tang, J. Grindlay, M. Moe, J. Orosz, R. Kurucz, S. Quinn & M. Servillat *The Astrophysical Journal*, in press (arXiv:1110.0019)

Abstract

I present photometric and spectroscopic observations of a peculiar variable (designated DASCH J075731.1+201735 or J0757) discovered from our DASCH project using the digitized Harvard College Observatory archival photographic plates. It brightened by about 1.5 magnitudes in B within a year starting in 1942, and then slowly faded back to its pre-outburst brightness from 1943 to the 1950s.

The mean brightness level was stable before and after the outburst, and ellipsoidal variations with a period of $P = 119.18 \pm 0.07$ days are seen, suggesting that the star is tidally distorted. Radial-velocity measurements indicate that the orbit is nearly circular ($e = 0.02 \pm 0.01$) with a spectroscopic period that is the same as the photometric period. The binary consists of a 1.1 ± 0.3 $M_\odot$ M0III star, and a 0.6 ± 0.2 $M_\odot$ companion, very likely a white dwarf (WD). Unlike other symbiotic binaries, there is no sign of emission lines or a stellar wind in the spectra. With an outburst timescale of ~ 10 years and estimated B band peak luminosity $M_B \sim 0.7$, J0757 is different from any other known classic or symbiotic novae. The most probable explanation of the outburst is Hydrogen shell-burning on the WD, although an accretion-powered flare cannot be ruled out.

5.1 Introduction

Symbiotic stars are interacting binaries consisting of an evolved red giant and a hot object, which is usually a White Dwarf (WD; see e.g. Kenyon 1986, 1994; Nussbaumer 2000; Mikołajewska 2007, and references therein). Mass is transferred from the red giant to its hot companion via stellar wind in most cases, but could also be Roche lobe overflow in some cases. They usually show low temperature absorption features from the red giant, and strong emission lines from surrounding circumstellar material ionized by the hot component. Most symbiotic stars have red giant masses $0.6 - 3.2$ $M_\odot$, hot component masses $0.4 - 0.8$ $M_\odot$, and orbital periods $\sim 200 - 1000$ days (Mikołajewska 2003).

Symbiotic stars are highly variable sources with variation timescales from

minutes to decades. The most common type of outburst, called a classical symbiotic outburst, recurs multiple times on decades-long time scales with amplitudes of $1-3$ mag, and with each outburst lasts from months to a few years (Kenyon 1986; Mikolajewska 2010). The nature of these outbursts is not entirely clear, and may be related to instabilities in the accretion disks (Mikołajewska 2003; Sokoloski et al. 2006). Another relatively rare type of outburst is symbiotic nova (also called slow nova), which shows a single long outburst lasting from years to decades due to thermonuclear runaways at the surface of the WD (Allen 1980; Paczynski & Rudak 1980; Kenyon & Webbink 1984). The peak luminosities range from 4000 to 40,000 $L_{\odot}$, depending on the mass of the WD (Murset & Nussbaumer 1994; Iben 2003). They mimic classical novae but with much longer timescales. Only 9 symbiotic novae are known so far (Belczyński et al. 2000; Mikolajewska 2010).

DASCH (Digital Access to a Sky Century @ Harvard) is a project to digitize and analyze the scientific data contained in the Harvard College Observatory (HCO) photographic plates taken from the 1880s through the 1980s. The motivation is to explore the temporal variations of stars and active galaxies on the relatively poorly explored $\sim 1-100$ yr timescales (but extending down to ~ 1 week timescales as well), as summarized by (Grindlay et al. 2009). We developed the astrometry and photometry pipeline (Laycock et al. 2010; Los et al. 2011; Servillat et al. 2011, Tang et al. in prep.), and have scanned $\sim$ 19,000 plates in five initial fields. Here we report the discovery of an unusual 10-yr outburst in a peculiar symbiotic system, DASCH J075731.1+201735 (named after its equatorial J2000 coordinate; hereafter J0757).

5.2 Observations and Results

5.2.1 DASCH and ASAS light curves

J0757 was measured on 694 plates near the M44 field noted by its peculiar long-term variability. These plates cover 5−25 degrees on a side with typical limiting magnitudes $B \sim 14 - 15$ mag, and most of them are blue sensitive emulsions. We used the GSC2.3.2 catalog (Lasker et al. 1990) for photometric calibration, and our typical uncertainty is $\sim 0.1 - 0.15$ mag (Laycock et al. 2010, Tang et al. in prep.). There are $\sim 1.2 \times 10^5$ objects with more than 100 magnitude measurements distributed over ~ 100 years from these plates covering the M44 field. J0757, which is N2211021132 in the GSC catalog, is the only one found with > 1 magnitude outburst on a ~ 10 year timescale above a well-defined quiescence level.

The DASCH light curve of J0757 is shown in Figure 5.1. We supplement the figure with V-band data from ASAS starting in the year 2000 (J0757 has the designation ASAS J075731+2017.6 Pojmanski 2002). J0757 is classified by ASAS as a semi-detached/contact binary with best-fit period of 119.2 days with 0.16 mag variations in the V band. Since ASAS data are in the V band, while DASCH magnitudes are in B, we added 1.5 mag to the ASAS V mag in the plot, which is about the sum of the maximum galactic extinction ($E(B-V) = 0.06$ Schlegel et al. 1998) and the typical $B - V$ value for a M0III star (1.43 Pickles 1998). We will discuss the spectral classification in Chapter 5.2.2.

As shown in Figure 5.1, J0757 was in quiescence until about March 1942. J0757 then brightened over the rest of the year of 1942, and slowly decayed until about

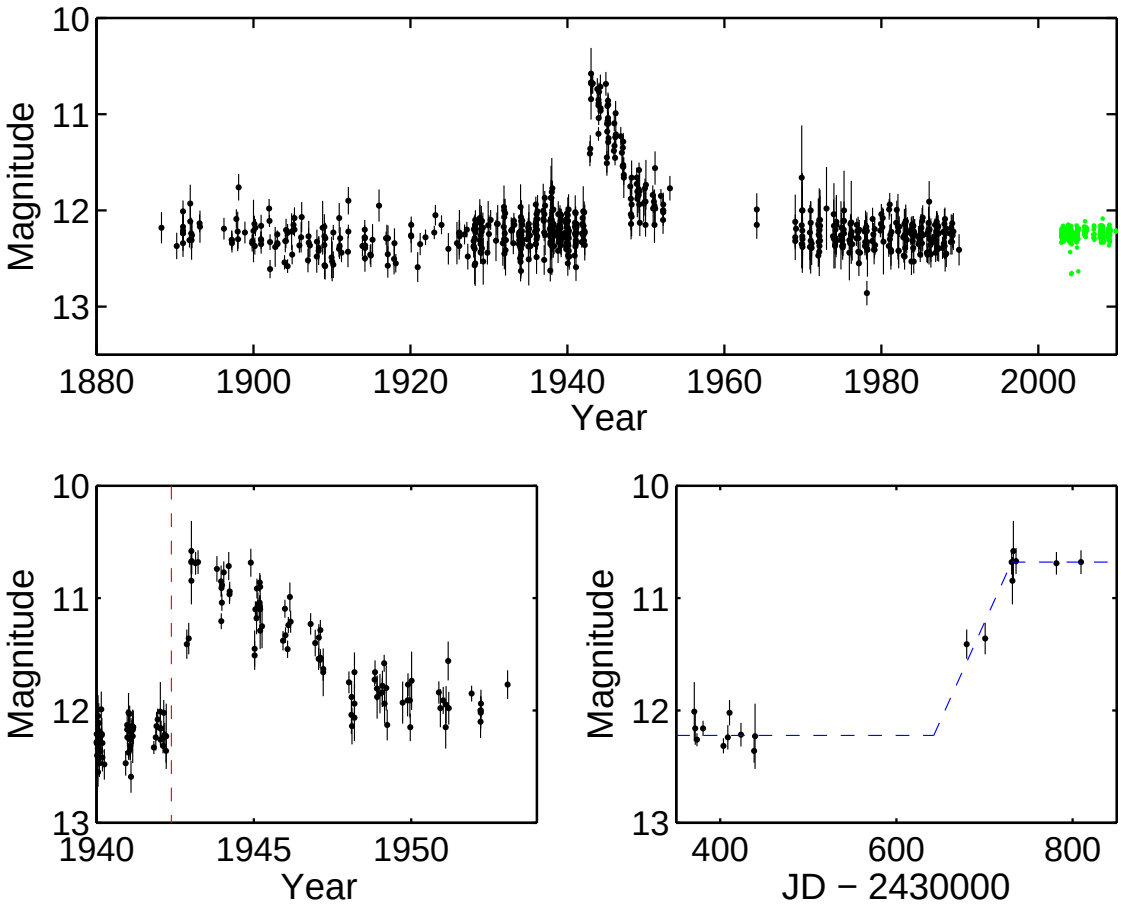

Figure 5.1.— Light curve of DASCH J075731.1+201735. The upper panel shows the whole light curve. Black dots with error bars are the light curves from DASCH, and small green dots after Year 2000 are the light curves from ASAS. Since ASAS data are in the V band, while DASCH magnitudes are in the B band, we added 1.5 mag to the ASAS V mag in the plot to convert it to B, as described in the text. The lower left panel shows the light curve from 1940 to 1954 for the outburst event; Data before the red dashed line (May 1942) are used as before the outburst. The lower right panel shows the light curve around 1942 for the rising of the outburst. The blue dashed line marks the median magnitudes in JD $2430250 - 2430440$ (12.22 mag; quiescence state) and JD $2430730 - 2430850$ (10.68 mag; brightest state), and a naive linear increase in between; The time span of the linear increase is 88.5 days.

1950. The peak magnitude was reached around January, 1943. There is a seasonal gap between April and October in 1942 when the star was low or not visible in the night sky, and thus we do not know when exactly the outburst started. If we naively assume that its magnitude increased linearly, then the outburst rise time is ~ 88.5 days (see the lower right panel in Figure 5.1).

Before and after the outburst when data are available (i.e. 1890−1942 and $1962 - 1990$), the magnitudes of J0757 were reasonably stable (note that the relatively constant B$\sim$ 11.9 from $\sim 1950 - 1954$ was not yet the quiescent value). The median DASCH magnitude before the outburst (e.g. before June 1942) is 12.24 and the median magnitude after the outburst (after 1960) is 12.26. The median magnitude of the entire DASCH light curve excluding the period between June, 1942 and the start of 1960 is 12.25, with rms scatter = 0.14 mag for the 607 data points outside the outburst. The median ASAS V magnitude is 10.75 mag, which corresponds to B=12.24, assuming the typical colors of an M0III star with galactic extinction.

5.2.2 Light curve folding and the photometric period

Both the DASCH and ASAS light curves show ellipsoidal variations. The ellipsoidal variation amplitude is ~ 0.11 mag in the DASCH data (B band, 1890−1942 and $1962 - 1990$), and ~ 0.16 mag in the ASAS data (V band, $2003 - 2009$).

We folded the light curves of J0757 to search for its photometric period. We divided DASCH light curve into two phases, i.e. before the outburst and after the outburst, as described in Chapter 5.2.1. We then got four sets of light curve data:

ASAS light curve, DASCH light curve excluding the outburst (before or after the outburst), DASCH light curve before the outburst, and DASCH light curve after the outburst.

We first folded the ASAS light curve with a given period, and fit it with a 3 harmonics Fourier model (an example is shown as the blue line in the upper panel of Figure 5.2). We fixed the model line in shape, but allow two free parameters, i.e. median magnitude and amplitude, for adjustments. Next, we fit the four sets of light curve data to the 3 harmonics Fourier model, and derived the reduced χ^2 as a function of different trial periods, as shown in the lower panels in Figure 5.2. DASCH data were binned by phase at the given period in the fitting. Our best fit period is 119.18 ± 0.07 days. The fact that the binary period is unchanged (within the errors) sets limits on the change of the orbit (due to mass transfer or onset of common envelope evolution). The resulting value for $\dot{a}/a$ is $0 \pm 4 \times 10^{-6}$ yr^{-1}.

5.2.3 Optical Spectroscopy

Spectra were obtained with the FAST spectrograph (Fabricant et al. 1998) on the 1.5-m Tillinghast reflector telescope at the F. L. Whipple Observatory (FLWO) for spectral classification. The spectra were reduced and wavelength-calibrated with standard packages (Tokarz & Roll 1997). Figure 5.3 shows the FAST 300 grating spectrum, which has a resolution of about 7 Å. The upper panel shows the whole spectrum, which suggests that its spectral type is M0; The lower panels show two luminosity indicators, which suggest that DASCH J0757 belongs to luminosity class III. The lower-left panel shows Ca I at 4226 Å, which disappears with increasing

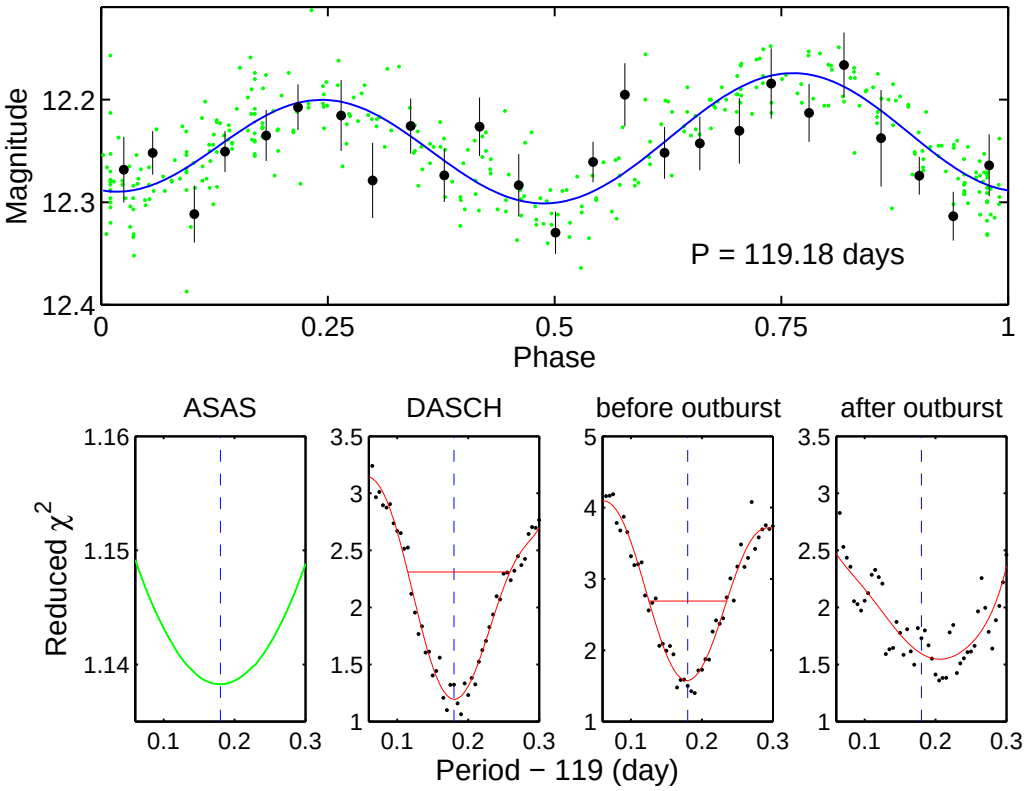

Figure 5.2.— Folded light curve and period search of DASCH J0757. The upper panel shows the foled light curve with $P = 119.18$ days and $T_0 = 2455597.98$. Black solid dots are DASCH data binned by phase, with error bars represent the standard deviation of the mean. Small green dots are ASAS data. Blue solid line is the best fit 3 harmonics Fourier model derived from the ASAS data. The lower panels show the reduced χ^2 as a function of folding period. From the left to the right are the reduced χ^2 using ASAS data, DASCH data excluding the outburst, DASCH data before the outburst (before June 1942, as indicated as red dashed line in the lower left panel in Figure 5.1), and DASCH data after the outburst (after 1960). The black dots are the reduced $\chi-$square values, and the red lines are a sixth order polynomial fit. In the two lower middle panels, i.e. DASCH data excluding the outburst, and DASCH data before the outburst, $1-\sigma$ confidence levels by assuming χ^2 distribution are marked as red horizontal lines. The more limited DASCH data after the outburst may suggest a ~ 0.02 days longer period, but this is not a significant deviation. The vertical blue dashed lines mark the best fit period of 119.18 days.

luminosity, indicating that DASCH J0757 is not a luminosity class I star. The lower-right panel shows the CaH B-band at 6385 Å, and the blend near 6362 Å consisting of Ti, Fe, and Cr. The weakness of CaH B-band suggests that DASCH J0757 is not a main sequence star. We therefore adopt a spectral type of ∼M0III for DASCH J0757, with uncertainties of $\sim \pm 1$ in both spectral type and luminosity class.

We also obtained spectra using the MIKE echelle spectrograph (Bernstein et al. 2003) on the 6.5 m Magallen/Clay telescope with a 0.7" ×5" slit on January 17, 2011. The spectral resolution is $R \sim 30,000$. The spectra were extracted using an IDL pipeline developed by S. Burles, R. Bernstein, and J. S. Prochaska[1]. The reduced spectra have $S/N \sim 50 - 100$ in 4300-9000 Å and $S/N >\sim 10$ in 3700-4300 Å. We computed a grid of spectrum templates for a range of abundances, effective temperatures, and gravities using Kurucz's programs ATLAS12 and SYNTHE (Kurucz 2005). We derived the projected rotation velocity of 10 ± 1 km s^{-1}. In M giants the continuum opacity is mainly H- which varies with metal abundance. The ratio of line to continuum does not change strongly with abundance. The TiO background is strong at any abundance because both Ti and O are alpha-enhanced at low abundances. We estimated an effective temperature of $T_{eff} = 3850 \pm 50$ K; a surface gravity of $log\ g = 1.0 \pm 0.5$ cgs; and a metallicity of $[Fe/H] = -0.6 \pm 0.1$, assuming J0757 is a population II star with alpha enhancements. The spectra can also be fit with Population I solar abundance templates. There is no sign of emission lines or wind in its spectra.

[1] http://web.mit.edu/∼burles/www/MIKE/

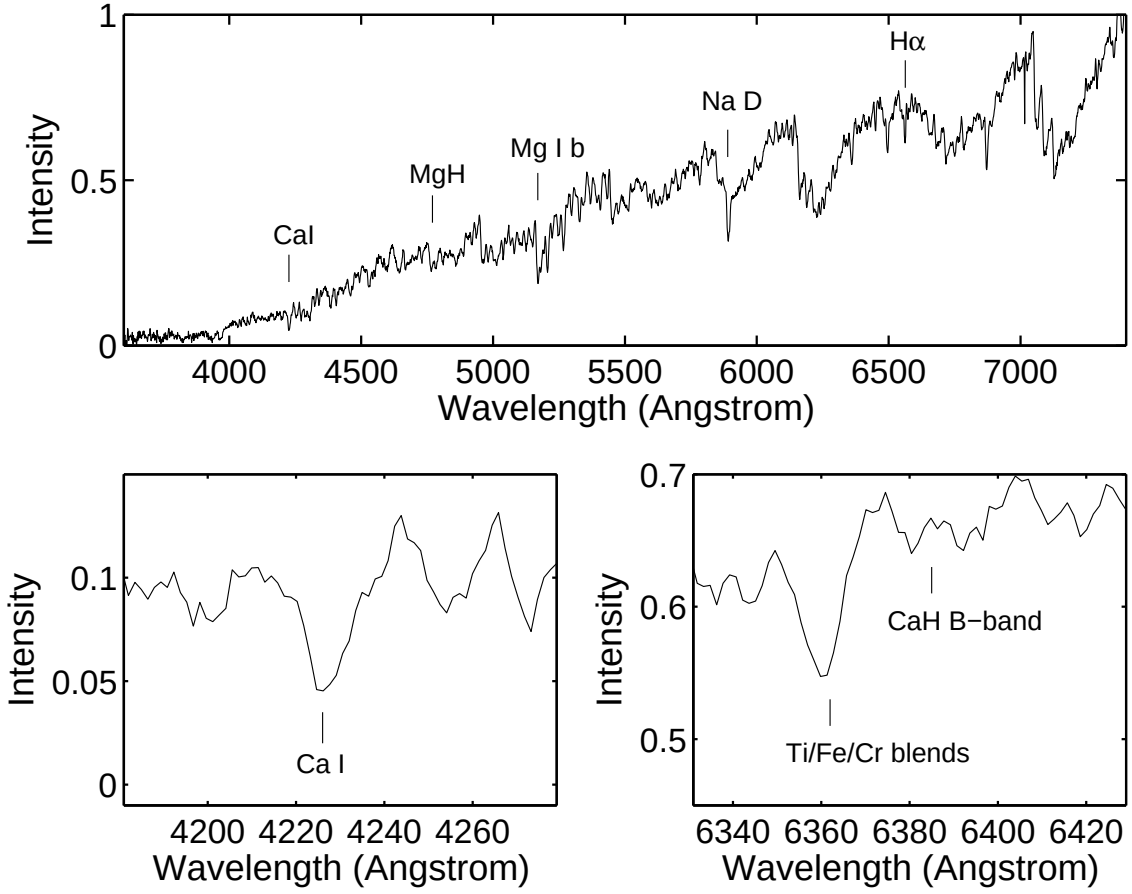

Figure 5.3.— FAST 300 grating spectrum of DASCH J0757. Spectral resolution is about 7 Å. The upper panel shows the whole spectrum. The lower panels show two luminosity indicators, Ca I at 4226 Å, and the CaH B-band at 6385 Å with the blend near 6362 Å consisting of Ti, Fe, and Cr on the left.

To measure the radial velocity curve of J0757, we obtained spectra on 15 different nights from October, 2010 through April, 2011 with the Tillinghast Reflector Echelle Spectrograph (TRES Szentgyorgyi & Furész 2007) on FLWO 1.5 m. These spectra were reduced and wavelength-calibrated with standard packages (Mink 2011). The spectral resolution is $R \sim 44,000$. The reduced spectra have typical S/N $\sim 10-30$ in 4500-9000 Å, and S/N $\sim 5-10$ in 4000-4500 Å.

Radial velocities of DASCH J0757 were derived from the TRES spectra, and were fitted to a model velocity curve using the derived photometric period (see Figure 5.4).

The derived orbital parameters are listed in Table 1. The resulting mass function is

$$f_1(M_2) = (3.31 \pm 0.02) \times 10^{-2}\ M_\odot, \tag{5.1}$$

and

$$M_2 \sin i = (0.3211 \pm 0.0006)(M_1 + M_2)^{2/3}\ M_\odot, \tag{5.2}$$

where subscript 1 denotes the red giant, and 2 denotes its companion.

For comparison, we have also fit a model velocity curve without using the photometric period of $P = 119.18 \pm 0.07$ days, and got similar results: $T_0 = 2455597.969 \pm 0.06$, $P = 118.89 \pm 0.080$ days, $\gamma = -33.57 \pm 0.04$ km s^{-1}, $K = 13.885 \pm 0.023$ km s^{-1}, $e = 0.024 \pm 0.015$, and $\omega = 70.38 \pm 0.09$ deg. In the following discussion throughout the paper, we adopt the parameters obtained using the photometric period of $P = 119.18 \pm 0.07$ days, as listed in Table 1.

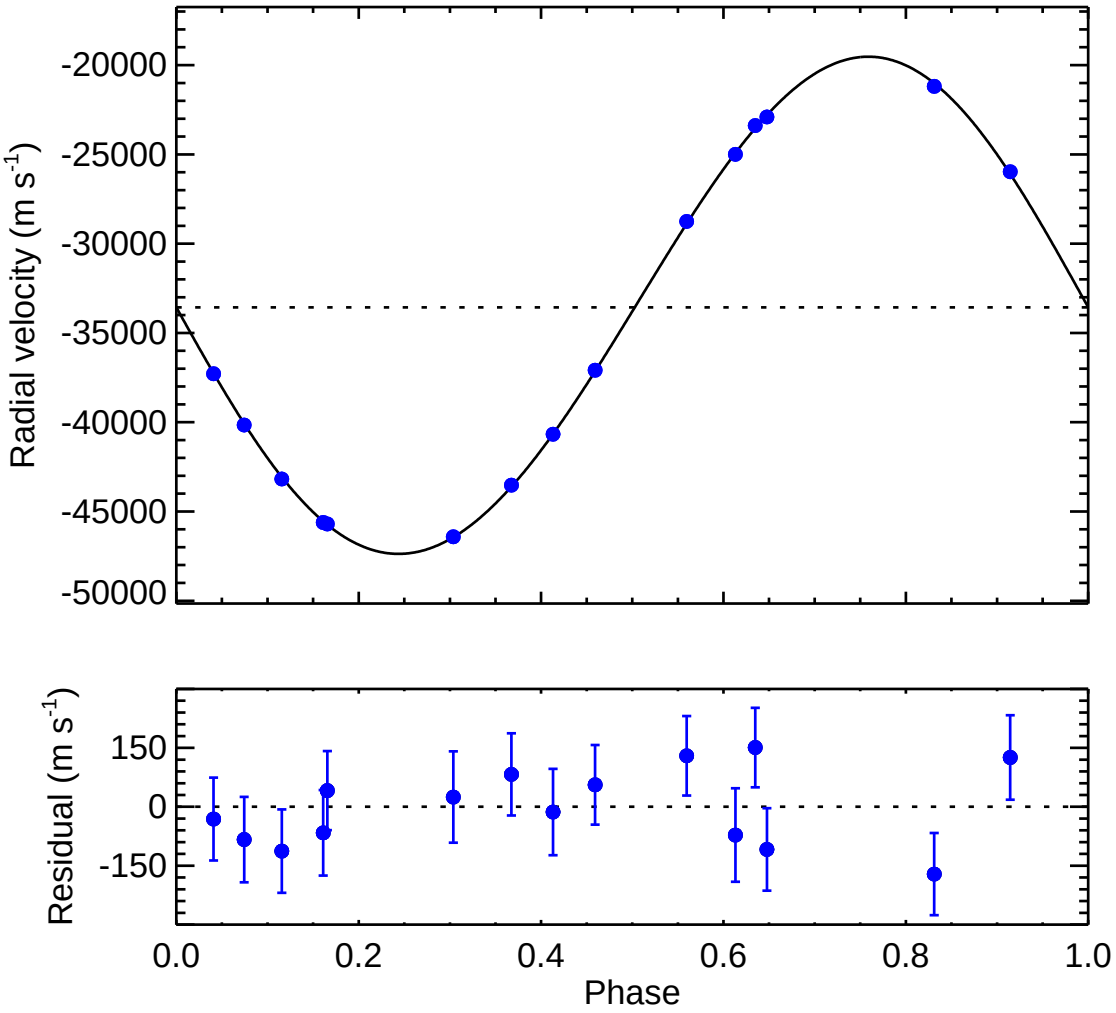

Figure 5.4.— Radial velocity of DASCH J0757 as a function of orbital phase, using the ephemeris in Table 1. Blue solid dots are observation data using the TRES spectrograph at the FLWO 1.5m, and the smooth curve is the best-fitting model. Residuals from the fit are given in the lower panel.

5.2.4 SED from archival data

Using archival data from WISE, IRAS, AKARI/IRAC, 2MASS, FON, SDSS, GALEX and ROSAT, we plotted the spectral energy distribution (SED) of J0757, as shown in Figure 5.5. The phase of the GALEX observation is 0.603 ± 0.01, and the phase of ROSAT observation is 0.426 ± 0.02. Here phase 0.5 is defined as inferior conjunction of the red giant. The SED is well matched by a synthetic spectrum of a $T_{\rm eff} = 3750$ K, and $\log g = 1.5$ giant (Lejeune et al. 1997), from IR to optical, as shown in black line in Figure 5.6. However, there is an excess in the GALEX NUV ($\sim 1900 - 2700$Å), which suggests a hot component in addition to the giant.

5.3 System parameters

5.3.1 Ellipsoidal models

We derive system parameters from the light and velocity curves. For this purpose we used the ELC code of Orosz & Hauschildt (2000) to model the ASAS V-band light curve and the TRES radial velocity curve. The ELC model is based on standard Roche geometry and uses specific intensities from model atmospheres, in particular the NextGen models of Hauschildt et al. (1999). ELC's use of the model atmosphere specific intensities eliminates the need for a parameterized limb darkening law, which is important in cases with red giants where the limb darkening near the stellar limb is very nonlinear (Orosz & Hauschildt 2000). We don't have model atmosphere specific intensities appropriate for white dwarfs. However, since

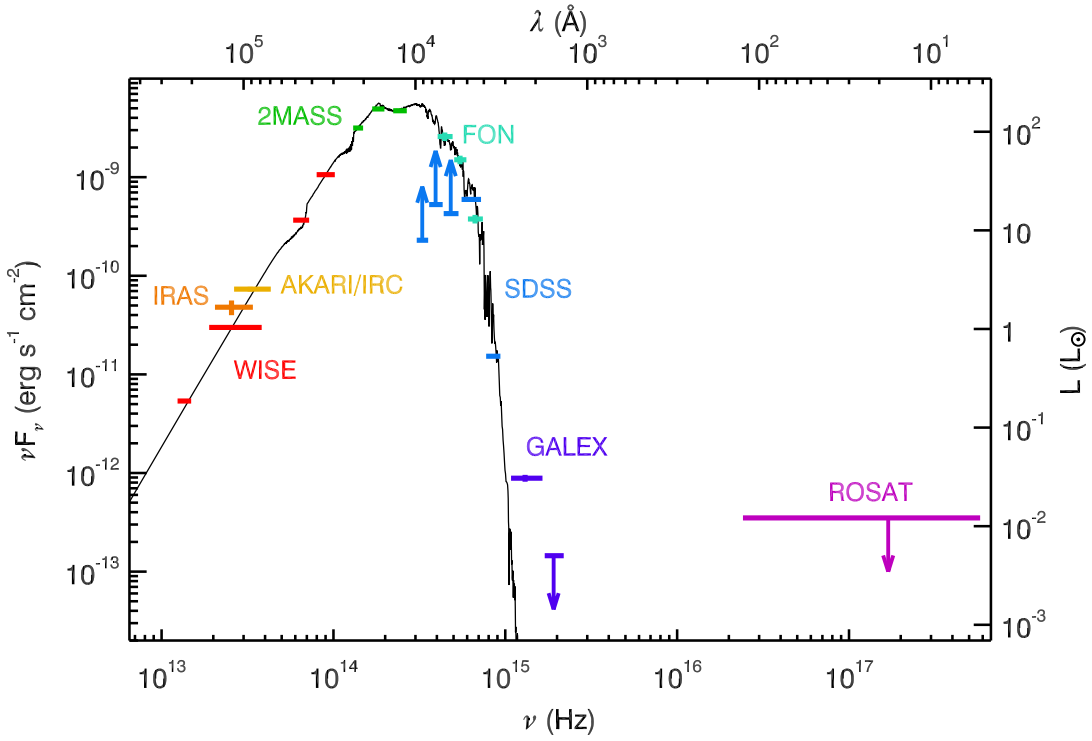

Figure 5.5.— SED of DASCH J0757 using archival data. The black line represents a synthetic spectrum of a T_{eff} = 3750 K, and log g= 1.5 giant (Lejeune et al. 1997). Note that SDSS riz bands are saturated; It was not detected by GALEX FUV and ROSAT.

the red giant dominates the V-band flux, this is not a serious limitation.

In our initial runs, we had 8 free parameters: the orbital period P, the time of periastron passage T_0, the inclination i, the Roche lobe filling factor f_1, the eccentricity e, the argument of periastron ω, the K-velocity of the red giant K, and the mass of the red giant M_1. We assumed synchronous rotation. The models are somewhat insensitive to the temperature of the red giant, and that parameter was held fixed at $T_1 = 3720$ K. In addition to the light and velocity curve, we used the projected rotational velocity of the red giant as an extra constraint.

The model fits were optimized using ELC's genetic code and its Monte Carlo Markov Chain code. After inspection of the post-fit residuals, additional free parameters were considered. We allowed the red giant's rotation to be asynchronous with the orbit, where Ω is the ratio of the spin frequency to the orbital frequency. We also accounted for heating by the WD. In this case, we fixed the luminosity of the irradiating source to $\log L_i = 36.6$ (c.g.s. units) and allowed the albedo A_1 to be a free parameter (the choice of A_1 is somewhat arbitrary since different combinations of L_i and A_1 can give identical light curves). Finally, we included an accretion disk that is parameterized by the outer radius in terms of the Roche radius $r_{\rm out}$, the temperature at the inner rim T_d, and the exponent of the disk temperature distribution ξ, where $T(r) = T_d(r/r_i)^{\xi}$.

Some typical results are shown in Figure 5.6. The binned ASAS light curve has maxima with different heights, which could be indicative of an eccentric orbit. However, the simultaneous fit to the radial velocities indicates a small eccentricity (0.012). Also, the minimum near phase 0.5, corresponding to the inferior conjunction

of the red giant, is deeper than the minimum at phase 0.0. For a pure ellipsoidal light curve, the minimum at phase 0.0 would be the deeper one. Heating by the irradiating source "fills in" the minimum near phase 0. However, in all of the models considered, we never had a case where the model curve had a deeper minimum near phase 0.5, so simple heating cannot explain the difference in the observed minima.

An accretion disk could potentially eclipse the red giant near phase 0, thereby making the minimum there deeper. This is opposite of what we want. Normally, the accretion disk does not give phase modulated light in the ELC model (if it is not eclipsed by the star). However, a "hot spot" on the disk rim can be used to mimic the place where the matter transfer stream impacts the disk. As the binary turns in space, different areas of this spot are visible, giving rise to extra light at certain phases. An example model is shown in Figure 5.6. The hot spot has an angular width of 18°, an azimuth (measured from the line of centers in the direction or the orbital motion) of 66°, and has a temperature of 3800 K, which is 4.3 times hotter than the rest of the disk rim. The maximum near phase 0.75 is fit, but the minimum near phase 0.5 is still not well-fit.

We did two runs of fitting with a Monte Carlo Markov chain, one with an external constraint on the rotational velocity, and one without the constraint. Results from both runs are similar. The best-fit ellipsoidal models have inclination of $60° \pm 5°$, WD mass of $0.5 \pm 0.1\,M_{\odot}$, red giant mass of $1 \pm 0.3\,M_{\odot}$, and red giant radius of $43 \pm 4\,R_{\odot}$.

We note that in order to match the observed rotational velocity of $V_{rot}sini = 10 \pm 1$ km s^{-1} derived from the MIKE spectra, the red giant must be

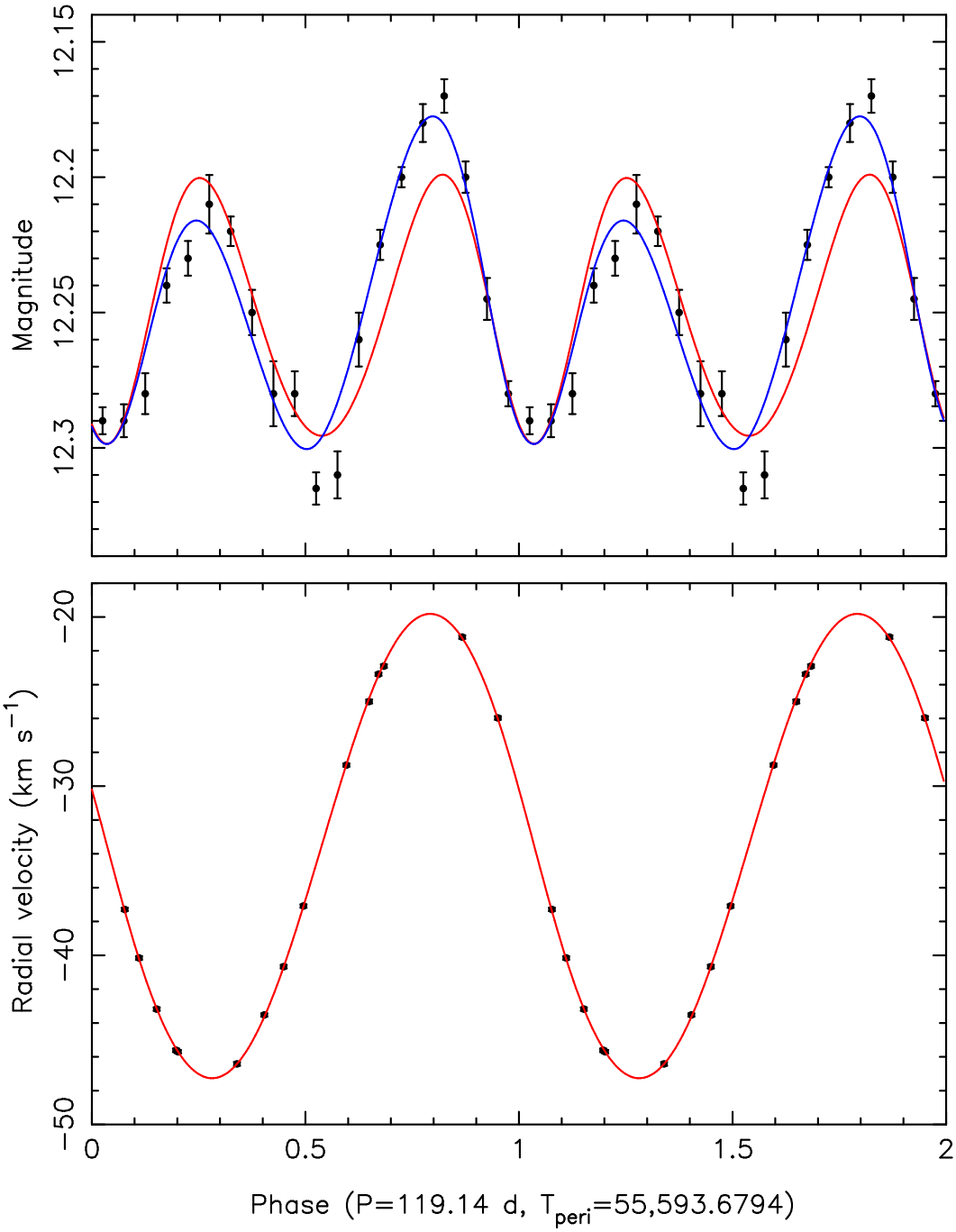

Figure 5.6.— Top: The phased and binned ASAS V-band light curve of J7057 and some representative ellipsoidal models. The red line is a model that includes irradiation and non synchronous rotation, and the blue line is a model that has an accretion disk with a hot spot. Bottom: The TRES radial velocity measurements phased on the same ephemeris (which uses the time of periastron passage as the zero-point) and the best-fitting model.

rotating 0.7 times slower than its synchronous velocity. Given the typical tidal synchronization timescale of $\sim 10^5$ yr (Zahn 1989) adopting the parameters listed in Table 1, the red giant is expected to be co-rotating with the binary. Consequently, the size of the giant should be $R_1 = PV_{rot}/2\pi = 23.5/\sin i\ R_\odot$, which is 27 $R_\odot$ if $i = 60°$, which are smaller than the radius derived from ellipsoidal fitting. Such a discrepancy has been seen in many symbiotic binaries, and is an unresolved "embarrassing problem" (Mikołajewska 2007). It probably comes from the extended atmosphere, and that limb darkening near the limb is very nonlinear. The light curve models with near-linear limb darkening produce ellipsoidal light curves with amplitudes that are too small. Also, the rotational broadening kernel can be a lot different than the usual analytic kernel, which in turn leads to strange biases in the $V_{rot}sini$ value (Orosz & Hauschildt 2000).

5.3.2 Estimates from the spectroscopic observations

Here we estimate the astrophysical parameters of DASCH J0757, based on the results in Sections 2 and 3.1. Since the galactic extinction is small ($E(B-V) = 0.06$ Schlegel et al. 1998), we do not take it into account for simplicity. The following estimated parameters are summarized in Table 1.

The inclination from the ellipsoidal fitting is $i \sim 55° - 65°$, and we adopt a more tolerant value of $i = 45° - 75°$ in the following estimates. The radius of the red giant ranges from $\sim 25 - 33\ R_\odot$ (from V_{rot} assuming synchronized rotation) to $\sim 43\ R_\odot$ (from ellipsoidal fitting), as discussed in Chapter 5.3.1. Therefore, we adopt a radius and error bar that encompasses both methods as $R_1 = 35 \pm 9\ R_\odot$. At

$T_{eff} = 3850 \pm 50$ K, the bolometric luminosity of the red giant is $L = 250 \pm 130\ L_{\odot}$, and its distance is 1.0 ± 0.3 kpc. The absolute magnitude of the system in quiescence is then $M_B = 2.2 \pm 0.6$.

Combining the radius, effective temperature, $log\ g = 1.0 \pm 0.5$ cgs and $[Fe/H] = -0.6 \pm 0.1$, the red giant mass inferred from stellar evolutionary models (Bertelli et al. 2008) is $M_1 \sim 0.9 \pm 0.4\ M_{\odot}$. This mass estimate for the giant is determined solely from the equations of stellar structure and is therefore independent of its prior evolution. The mass of the giant may have been greater in the past. However, considering the giant is only partially filling its Roche lobe as inferred from the ellipsoidal fitting, and given the M0III wind loss rate of $\sim 10^{-9} - 10^{-8}\ M_{\odot}$ yr^{-1} (Cox 2000), we do not expect it has lost a significant fraction of its current mass over the $\sim 10^7$ yr lifetime of the giant in its current phase of evolution. Requiring $0.8\ M_{\odot}$ to turn-off from main sequence within a Hubble time, we then have $M_1 \sim 1.1 \pm 0.3\ M_{\odot}$. From equation (2) and our adopted $i = 45 - 75°$, this implies the secondary mass is $M_2 \sim 0.6 \pm 0.2\ M_{\odot}$, and the orbital separation $a \sim 120 \pm 11\ R_{\odot}$. Therefore, the Roche lobe radii of the two stars are $R_{RL,1} \sim 53 \pm 4\ R_{\odot}$, and $R_{RL,2} \sim 38 \pm 6\ R_{\odot}$, for the M giant and the secondary, respectively (Eggleton 1983). The Roche lobe filling factor of the M giant is then $f_{RL} = R_1/R_{RL,1} = 0.66 \pm 0.17$.

If the deviation of the ASAS folded light curve and the ellipsoidal model with a giant alone is caused by a hot component due to a WD companion, its accretion disk and/or a tidal stream, then it is about 3% the luminosity of the giant in the V band. The luminosity of the hot component is then $2 - 8\ L_{\odot}$, for an effective temperature in the range of $3800 - 10,000$ K. For a $M_2 \sim 0.6\ M_{\odot}$ WD with $R_2 \sim 0.01\ R_{\odot}$, assuming all the gravitational potential energy is converted to thermal radiation, the

corresponding accretion rate is $1 - 4 \times 10^{-9}$ $M_\odot$ yr^{-1}.

During the 1942-1950s outburst, the B magnitude of J0757 increased by ~ 1.5 mag at the peak. At a distance of $D \sim 1$ kpc, the absolute B magnitude of the outburst is $M_{B,outburst\ peak} \sim 0.7$ mag. The peak bolometric luminosity of the outburst, $L_{outburst\ peak}$ depends on its SED. If the outburst has similar SED as a M0III star, then $L_{outburst\ peak} \sim 750\ L_\odot$. The minimum required bolometric luminosity would be when the radiation is peaked in the B band, i.e. $L_{outburst\ peak} \sim 100\ L_\odot$ at $T \sim 8100$ K. Such a temperature is consistent with the observed hot component temperature of CH Cyg during its 1992 outburst powered by accretion (Skopal et al. 1996). If the outburst is powered by Hydrogen shell-burning, the temperature during the outburst would be much hotter, i.e. $T_{outburst} \sim 10^5$ K as observed in some symbiotic stars (Muerset et al. 1991). For example, Z And is found to have a temperature of $\sim 9 \times 10^4$ K during its 2000-2002 outburst (Sokoloski et al. 2006). If the outburst in J0757 has a temperature of 9×10^4 K, most of the radiation is in the UV, and the corresponding bolometric luminosity of $\Delta B = 1.5$ mag increase is $L_{outburst\ peak} \sim 2.5 \times 10^4\ L_\odot$ assuming black body radiation.

5.4 Discussion

The amplitude and timescale of the 1940s outburst, and its stability during quiescence phases (except the periodic ellipsoidal variation), is very unusual. The mass loss rate of a M0III star is $\sim 10^{-9} - 10^{-8}$ $M_\odot$ yr^{-1} (Cox 2000). With a Roche lobe filling factor $\sim 0.5 - 0.8$ as discussed in Chapter 5.3.2, a significant fraction of the wind could be transferred to its companion via wind Roche lobe overflow

(Podsiadlowski & Mohamed 2007). If the secondary is a 0.6 $M_\odot$ Main Sequence (MS) star with $R \sim 0.6\ R_\odot$, the only way to power the outburst is by gravitational energy release. The least required accretion rate to power the 1940s outburst of J0757 is then $3 \times 10^{-6}\ M_\odot\ \mathrm{yr}^{-1}$ ($L_{peak} \sim 100\ L_\odot$ if $T \sim 8100$ K), which is 2 to 3 orders of magnitude higher compared with the typical mass loss rate of the M giant. Therefore, a compact object, almost certainly a WD (at $\sim 0.6\ M_\odot$, it cannot be a Neutron star or a black hole), is needed to power the outburst.

If the outburst was powered entirely by accretion on to a 0.6 $M_\odot$ WD, the least required accretion rate to power the 1940s outburst of J0757 is $5 \times 10^{-8}\ M_\odot\ \mathrm{yr}^{-1}$, assuming all the potential energy is converted into radiation ($L_{peak} \sim 100\ L_\odot$ if $T \sim 8100$ K). However, J0757 only showed one single outburst and was stable before and after the outburst, which is different from other symbiotic systems with accretion-powered outbursts, such as PU Vul (before its nuclear runaway outburst in 1977), which was highly variable with multi-epoch outbursts (Liller & Liller 1979). Another symbiotic variable powered by accretion, CH Cyg, was stable prior to 1963 for several decades, but later showed a series of outbursts since the onset of activity in 1963 (Mikolajewski et al. 1990).

The most probable explanation of the J0757 outburst, is then Hydrogen burning on the surface of the WD. The outburst profile of J0757, i.e. a relatively sharp rise and exponential-like decay, closely resembles that of Z And and CI Cyg, which are believed to be related to the presence of unstable accretion disk around a white dwarf with hydrogen burning shell (Mikołajewska 2003; Mikolajewska et al. 2002). A "combination nova" outburst on Z And has been reported by (Sokoloski et al. 2006), which is triggered by an accretion instability and resulted in increased thermonuclear

burning. The outburst of J0757 may have started at the stable burning zone ($\dot{M} > \dot{M}_{crit} = 3.3 \times 10^{-8}\ M_\odot\ \mathrm{yr}^{-1}$ for a 0.6 $M_\odot$ WD Nomoto et al. 2007; Shen & Bildsten 2007) with an increased accretion rate due to an accretion disk instability (King et al. 2003), when the accumulated envelope mass on the WD exceeded the critical value ($3 \times 10^{-5}\ M_\odot$ Townsley & Bildsten 2004). Then, consequently, hydrogen was ignited and started quasi-steady burning to power the outburst. The luminosity of such a quasi-steady burning increases with higher WD mass, as well as higher accretion rate. For a 0.6 $M_\odot$ WD, the theoretical luminosity at $\dot{M}_{crit}$ is $L \sim 10^{3.4}\ L_\odot$, and the effective temperature is $\sim 2.5 \times 10^5$ K; If $\dot{M} \sim 4\dot{M}_{crit}$, then the luminosity is $\sim 10^4\ L_\odot$, and the effective temperature is $\sim 8 \times 10^4$ K (Nomoto et al. 2007). Such a range of luminosity and corresponding temperature is consistent with the estimated peak luminosity of J0757, which is $\sim 10^4\ L_\odot$ if $T \sim 10^5$ K.

The timescale of the Hydrogen shell burning strongly depends on the mass of the WD, accretion rate, and whether a optically thick wind occurs (Kato & Hachisu 1994; Prialnik & Kovetz 1995). Kato et al. (2011) suggested that the companion star plays an important role in producing a wind, and thus affects the timescale of the outburst. As shown in Figure 5.6 in Kato et al. (2011), in wide symbiotic binaries like PU Vul ($P_{orb} = 4900$ days), the expanded WD envelope is not affected by the companion, resulting in a quiet evolution without strong winds in the outburst, and thus longer outburst (peak plateau timescale of ~ 10 yr); On the other hand, in close binaries such as V723 Cas and HR Del ($P_{orb} < 1$ day) with similar WD masses as PU Vul ($\sim 0.6\ M_\odot$), the companion would have been deeply embedded in the nova envelope, resulted in strong winds and much shorter outburst (peak plateau timescale of ~ 200 days). We note that J0757, with $P_{orb} = 119.2$ days and a

peak plateau lifetime of $\sim$ 1 yr (as shown in the lower-left panel in Figure 5.1), lies interestingly in the region between the canonical symbiotic novae such as PU Vul, and novae in close binaries such as V723 Cas.

The absence of emission lines in the spectra of J0757 is peculiar, but not incompatible with the Hydrogen burning powered outburst picture. Nova emission lines disappear quite rapidly after the outburst (Downes et al. 2001), and it is not surprising that we do not see emission lines 60 years after the outburst. The lack of emission lines could be due to either or both of the following: The first possible reason is that there is no significant surrounding material. This may be either due to small amount of mass loss in the system even during the nova outburst, which is consistent with the recent results by Starrfield et al. (2012); or due to the fact that ejected shells disappear very fast, such as observed in V723 Cas (Krautter et al. 2002). The second possible reason is the lack of ionizing UV photons. A post-nova WD can cool off fast, for example, the white dwarf in DQ Her has been found to be below 10 $L_{\odot}$ 40 years after the nova outburst (Stasińska & Tylenda 1990). As discussed in sections 2 & 3, the luminosity of the hot component in J0757 is only a few $L_{\odot}$, while the luminosity of the M giant is $\sim$ 250 $L_{\odot}$, which dominates the spectrum. Similar cases have been found in a few symbiotic X-ray binaries, where the hot component is $\sim$ 3 orders of magnitude fainter than the red giant, and emission lines are absent in the optical spectra (Masetti et al. 2002, 2007).

In summary, DASCH J0757 is an intriguing system with many unusual properties. It differs from other known classic or symbiotic novae, and is more likely a new type of nova-like variable located in the gap region between classic novae and symbiotic novae. Unlike most other symbiotic stars, it does not contain a luminous

hot component or nebula emission lines, and its magnitude is stable after the 1940s outburst. Its current photometric and spectroscopic profile is not different from a normal red giant binary. It would not be picked out without the detection of its long outburst in 1940s, made possible by the long timescales observed with DASCH. Future observation in the UV and X-ray will help understand its mass transfer and accretion processes.

Given the lack of other observations during the outburst of J0757, it is hard to reach a definite conclusion whether it was powered by Hydrogen shell burning or accretion. If it was indeed Hydrogen burning with no significant mass loss, it could be a promising channel of accumulating mass on the WDs. Systems similar to DASCH J0757, but with more massive WDs ($>\sim 1\ M_{\odot}$), could thus be promising type Ia SNe progenitors. They are not luminous supersoft X-ray sources in quiescence (see also Di Stefano 2010), and would not be picked out by the usual searches for symbiotic stars, but could be detected by the study of their long-term light curves. Note that J0757 is found from ~ 700 plates, while there are nearly half a million plates available to be scanned and analyzed in DASCH. With its 100 year light curve coverage, DASCH has a great potential to find more of such sources, which will shed light on the understanding of type Ia SNe progenitors, as well as the study of binary evolution and accretion physics.

Table 5.1: Astrophysical parameters for DASCH J0757. Details are discussed in Sections 2&3.

Parameter	Value
Observational parameters with highest confidence:	
Spectral type	M0III
T_0 (HJD)	2455597.980 ± 0.054
Period (days)	119.18 ± 0.07
γ (km s^{-1})	-33.57 ± 0.04
K_1 (km s^{-1})	13.906 ± 0.025
Eccentricity	0.025 ± 0.01
ω (deg)	70.49 ± 0.09
$V_{rot} \sin i$ (km s^{-1})	10 ± 1
Parameters derived from atmosphere fitting:	
T_{eff} (K)	3850 ± 50
log g (cgs)	1.0 ± 0.5
`[Fe/H]`	-0.6 ± 0.1
Estimates based on models:	
i (deg)	60 ± 15
M_1 ($M_\odot$)	1.1 ± 0.3
M_2 ($M_\odot$)	0.6 ± 0.2
Orbital seperation ($R_\odot$)	120 ± 11
R_1 ($R_\odot$)	35 ± 9
L_1 ($L_\odot$)	250 ± 130
Distance (kpc)	1.0 ± 0.3
h_z (pc)	400 ± 110
M_B in quiescence	2.2 ± 0.6
M_B outburst	0.7 ± 0.6
$L_{\texttt{outburst peak}}$ ($L_\odot$)	$10^2 - 10^4$ (if no constraint on T_{hot})
	100 (if $T_{hot} \sim 8100$ K)
	2.5×10^4 (if $T_{hot} \sim 90,000$ K)
L_{hot} in quiescence ($L_\odot$)	$\sim 2 - 8$
$\dot{M}$ in quiescence ($M_\odot$ yr^{-1})	$\sim 1 - 4 \times 10^{-9}$

Chapter 6

100-year DASCH Light Curves of Kepler Planet-Candidate Host Stars

S. Tang, D. Sasselov, J. Grindlay, E. Los & M. Servillat *The Astronomical Journal*, submitted

Abstract

I present 100 year light curves of Kepler planet-candidate host stars from the Digital Access to a Sky Century at Harvard (DASCH) project. 240 out of 997 host stars have at least 10 good measurements on DASCH plates. 111 of them have at least 100 good measurements, including 73% (74 out of 102) of all host stars with $g \leq 13$ mag, and 45% (102 out of 226) of all host stars with $g \leq 14$ mag. Our typical

photometric uncertainty is $\sim 0.1 - 0.15$ mag. No variation is found at 3σ level for these host stars, which is good for the habitability of these planets.

6.1 Introduction

In 2011 the Kepler Mission has announced 997 stars with a total of 1235 planetary candidates that show transit-like signatures (Borucki et al. 2011). It is estimated that more than 95% of these candidates are planets (Morton & Johnson 2011). Kepler has completed 3 years of observations and with a 4-year extension will accumulate 7.5 years of data for these host stars. Searching the host stars for significant very long-term variations on timescales of decades and for rare flare events is important for understanding fully the environments of their planets and for constraining the habitability of exoplanets in general. Here we present the 100-year light curves of Kepler planet-candidate host stars from the Digital Access to a Sky Century at Harvard (DASCH) project (Grindlay et al. 2009).

The photometric variability of about 105,000 Kepler target stars, including the sample with planetary candidates, shows low-level variability due to modulation by spots and other manifestations of magnetic activity, e.g., white light flares (Basri et al. 2011). None of these have amplitudes that would be detectable (> 0.2 mag) in the DASCH data. Here we aim to complement the short-timescale and high-precision photometry by Kepler with much longer timescales. The DASCH project can reveal stars with rare flare events or extremely slow changes in luminosity; it is of interest to find out if any such star happens to have planetary candidates. This paper provides DASCH light curves for the current Kepler sample.

6.2 DASCH light curves

In order to take advantage of the unprecedented Kepler data on short timescales (Borucki et al. 2010), which complements DASCH data on long timescales, we have scanned and processed 3653 plates taken from the 1880s to 1990 in or covering part of the Kepler field. Each plate covers 5−40 degrees on a side, and most of them are blue-sensitive (close to Johnson B). These plates are from 16 different series, each typically represents a single telescope (except mb series which consists of data from multiple telescopes). Table 1 lists information on number of plates in each series, telescope aperture, field of view (FOV), and median limiting magnitude of the plates used in this work. The errorbar in the limiting magnitude represents the rms of the limiting magnitude distribution in each plate series. These plates were selected by their overlap with the Kepler field, and most of them only cover part of the Kepler field. Most plates have limiting magnitudes $12 - 14$ mag, while $\sim 9\%$ of them (mc series) are down to ~ 17 mag. We used the Kepler Input Catalog (KIC; Brown et al. 2011) for photometric calibration. The typical photometric uncertainty is $\sim 0.1 - 0.15$ mag, and astrometric uncertainty $\sim 0.8 - 5''$ (Laycock et al. 2010; Los et al. 2011; Servillat et al. 2011, Tang et al. in prep.).

Example DASCH light curves of 4 Kepler planet-candidate host stars are shown in Figure 6.1. Fainter stars have fewer DASCH measurements, due to smaller number of deeper plates available. All the light curve data and plots are available at the DASCH website (http://hea-www.harvard.edu/DASCH/papers/Kepler-planet-host-star-lightcurves). Only good measurements are included. Blended images, measurements within 0.75 mag of the limiting magnitude which are more likely to be

Table 6.1: List of 3653 processed plates in the Kepler field.

Series[a]	Number of plates	Lens aperture (inches)	FOV (°)	Limiting magnitude
ac	1577	1.5	34×43	12.1 ± 0.9
i	690	8	9×12	13.8 ± 0.9
dnb	428	1.6	33×41	14.2 ± 0.7
rh	342	3	22×28	13.4 ± 1.1
mc	320	16	6×7	17.0 ± 1.2
bm	96	1.5	22×27	13.6 ± 0.9
ay	63	2.6	39×49	12.4 ± 0.8
dnr	47	1.6	33×41	11.7 ± 0.7
ca	40	2.5	34×42	12.3 ± 0.7
ma	19	12	5×7	16.0 ± 1.5
dny	12	1.6	33×41	13.8 ± 1.0
mb	8	3 to 6	22×28	13.4 ± 0.7
aco	5	1	35×43	12.6 ± 1.1
ax	4	3	39×49	12.9 ± 0.7
am	2	1	34×43	12.9 ± 0.4

[a]There are 89 recently scanned 'a' series plates not included in the paper.

contaminated by noise, images within the outer border of the plates whose width is 10% of the plate's minor-axis length (the so called the ninth annular bin in Laycock et al. 2010), and dubious points with image profiles different from neighbor stars and thus are suspected to be emulsion defects or dust, are excluded. Stars with strong correlation between magnitude measurements and plate limiting magnitudes, or between magnitude measurements and plate astrometry uncertainties, are also excluded, which are very likely to be polluted by noise or blends. More detailed description can be found at Tang et al. (in prep.). For comparison, their Kepler light curves (Q0−Q6 for 8478994, 11623629 and 11086270, and Q1−Q6 for 4951877) are also shown in Figure 6.1 as green dots. We used the PDC corrected flux, which are converted to magnitudes and shifted to the mean magnitudes of DASCH light curves (See http://keplergo.arc.nasa.gov/CalibrationSN.shtml). Note that these stars have variations at $0.01\% - 0.1\%$ level in the Kepler light curves, which are much smaller than the plotting symbols and our photometric accuracy.

Among 997 host stars, 240 stars have at least 10 good measurements on DASCH plates, and 111 stars have at least 100 good measurements. Distributions of g band magnitudes for all the host stars and host stars with at least 10 or 100 DASCH measurements, are shown in Figure 6.2. We have at least 100 measurements for 73% (74 out of 102) of all host stars with $g \leq 13$ mag, and 45% (102 out of 226) of all host stars with $g \leq 14$ mag. Most stars brighter than $g = 13$ mag were lost due to blending with neighbor stars, as expected in such a crowded field, with 70% of them have close neighbor stars brighter than $g = 14$ mag within 1 arcmin, while only 18% of $g < 13$ stars with at least 100 good measurements have $g < 14$ mag neighbor stars within 1 arcmin.

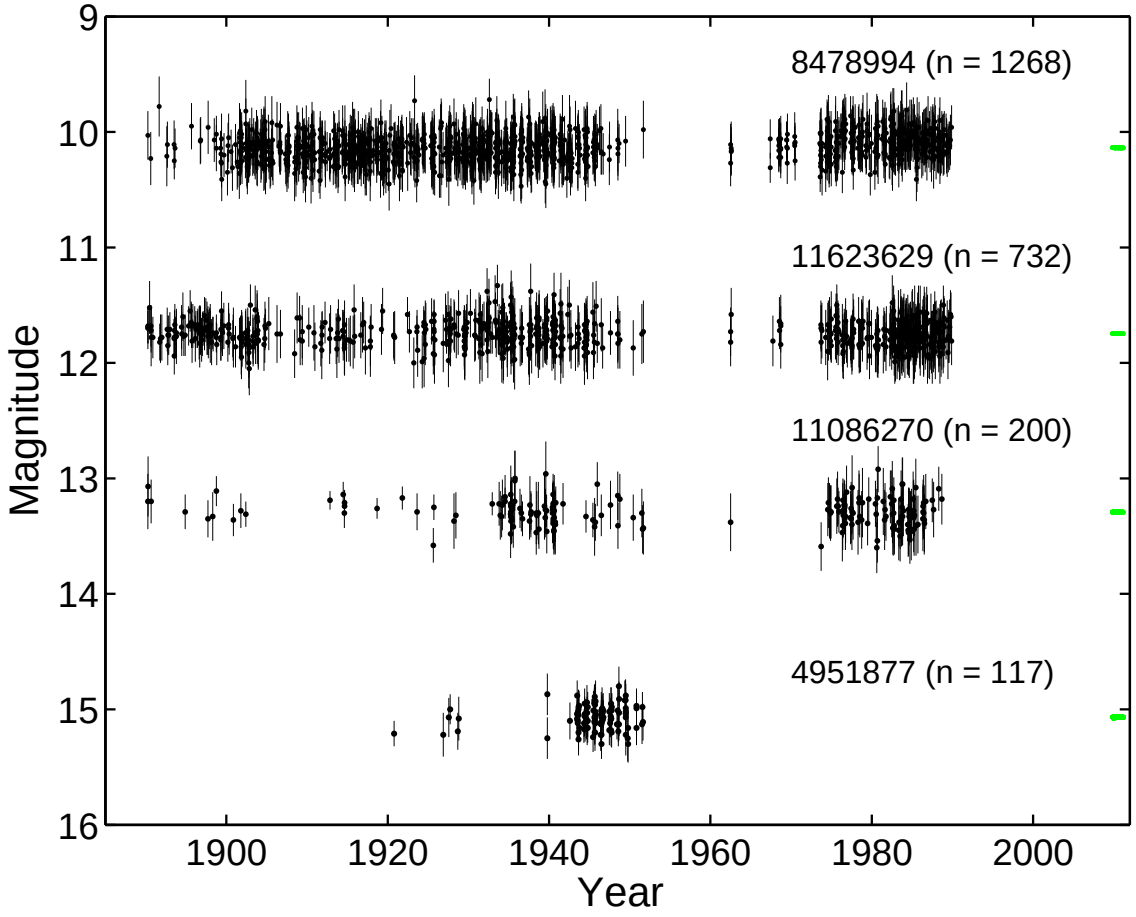

Figure 6.1.— Example DASCH Light curves of 4 Kepler planet-candidate host stars. From top to bottom: KIC 8478994, 11623629, 11086270, and 4951877. Number of measurements (n) in each light curve are also shown, which drops for fainter stars due to smaller number of deeper plates available. Kepler PDC corrected light curves are also shown in green dots for comparison; note that the variation in the Kepler light curves for these stars are at 10^{-4} to 10^{-3} level, much smaller than the plotting symbols.

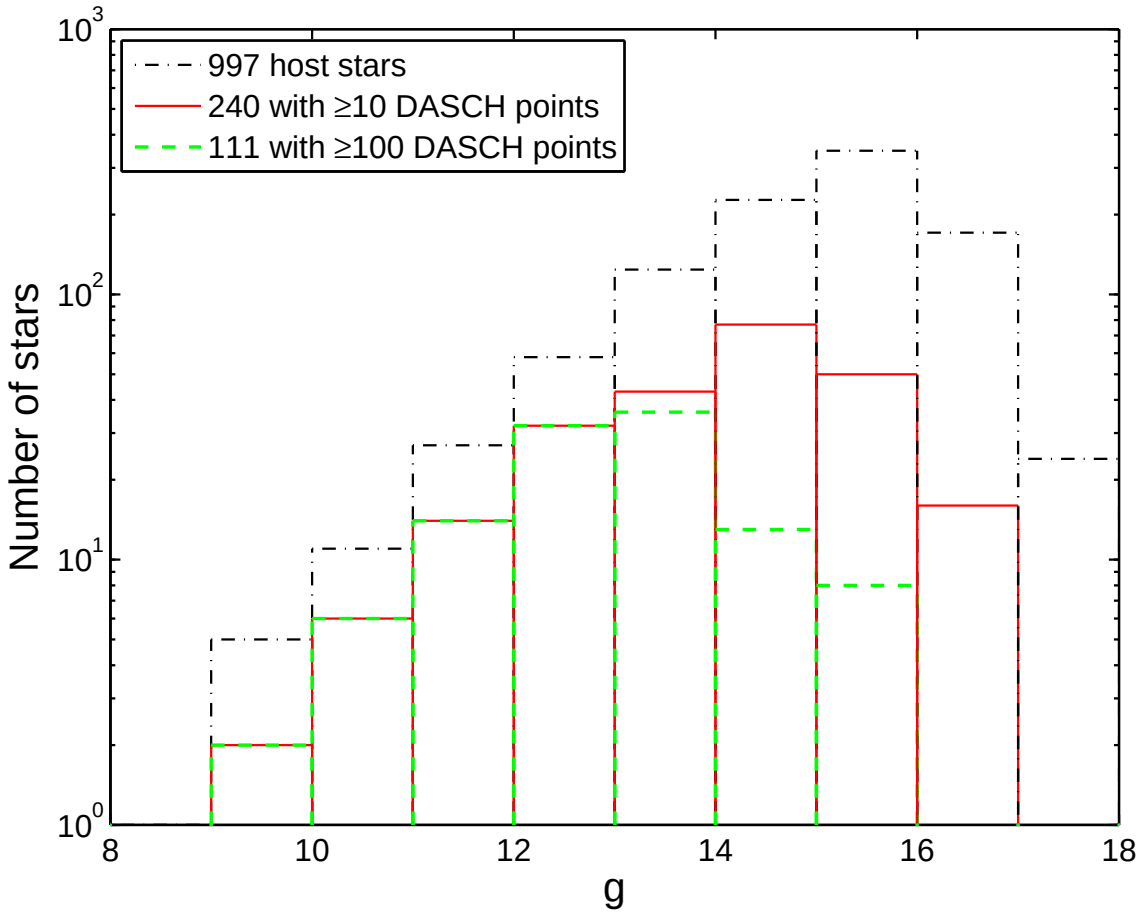

Figure 6.2.— Distribution of g band magnitudes for 997 Kepler planet-candidate host stars from Borucki et al. 2011 (black dash-dotted line), 240 host stars with at least 10 DASCH measurements (red solid line), and 111 host stars with at least 100 DASCH measurements (green dashed line).

The light curve rms vs. g band magnitude for the 240 host stars with at least 10 DASCH measurements are shown in Figure 6.3. The black solid line shows the median light curve rms of all the stars with at least 10 DASCH measurements in the Kepler field, and the red dashed lines and green dash-dotted lines show the 1σ and 2σ distribution, respectively. The median, 1σ, and 2σ distributions of light curve rms are calculated in 0.5 magnitude bins, after three iterations of 4σ-clipping. No variation is detected in any of the host stars at $> 3\sigma$ level. There is one planet host star, i.e. KIC 3632418 ($g = 8.74$), with light curve rms above the 2σ distribution. Further examination show that some images are lightly polluted by a $g = 11.43$ mag neighbor star located at 51" away from the star, and thus its rms excess is dubious.

6.3 Summary

The Kepler mission has discovered more than 2000 planetary candidates and provided unparalleled precision light curves for their host stars. Here we complement that database with much longer timescale 100-year light curves from the DASCH project. Despite their inferior photometric accuracy, the DASCH light curves sample such an extended period of time (e.g., tens of solar-like cycles of activity), that rare or very slow phenomena can be studied. As a sample statistics, such long-term variations and rare flare events help us understand the planetary environments around main sequence stars and the habitability of exoplanets in general.

We have scanned and processed 3653 plates taken from the 1880s to 1990 in or covering part of the Kepler field, and studied the light curves of 240 planet host stars that have at least 10 good measurements on DASCH plates. We find no variation

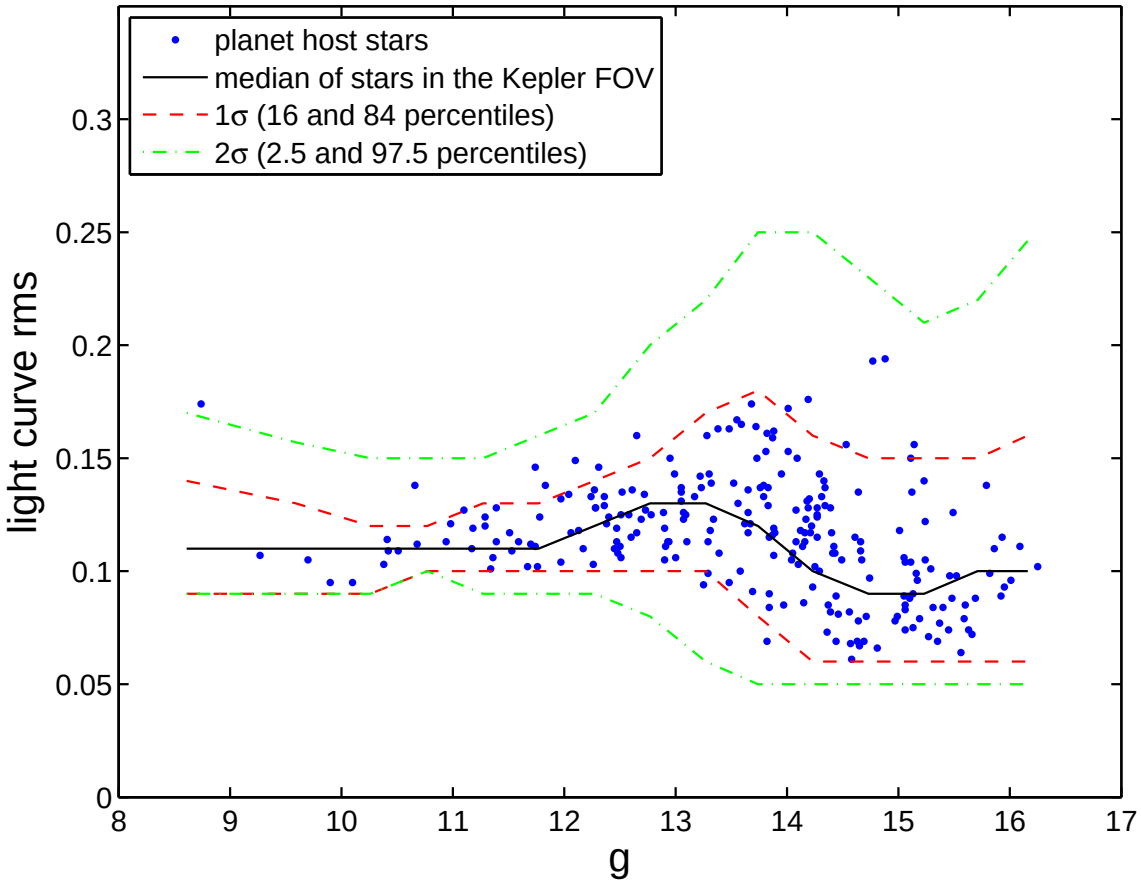

Figure 6.3.— DASCH light curve rms vs. g band magnitude. The 240 Kepler planet-candidate host stars with at least 10 DASCH measurements are plotted as blue dots. Light curve rms percentiles of 80,024 stars with at least 10 DASCH measurements in the Kepler field are shown for comparison. The 50th percentile (median) is shown in black solid line, the 16th and 84th percentiles (1σ) are shown in red dashed line, and the 2.5th and 97.5th percentiles are shown in green dash-dotted lines. The analysis is divided into 0.5 magnitude bins, and variable candidates with $> 3\sigma$ rms are excluded.

at 3σ level. All the light curve data and plots are available at the DASCH website (http://hea-www.harvard.edu/DASCH/papers/Kepler-planet-host-star-lightcurves). As the Kepler data extends in the next 4 years, it will be possible to improve on the determination of rotation modulation and small flares, as well as partial coverage of activity cycles, for the Kepler planet host stars. DASCH light curves over 100 year timescales will continue to provide unique constraints on long-timescale variability for planet host stars.

Chapter 7

DASCH Variable Search in the Kepler Field

S. Tang, J. Grindlay, & E. Los *The Astronomical Journal*, in prep.

Abstract

Here I present the DASCH variable search in the Kepler field of view (FOV). We have scanned over 3000 plates in or covering part of the Kepler FOV, with typical magnitude uncertainty of $\sim 0.1 - 0.13$ mag down to $B \sim 13 - 14$. I describe the variable search algorithms, and a preliminary DASCH variable catalog in the Kepler field. Most bright ($g < 13$ mag) and large amplitude ($\Delta V > 0.5$ mag) known ASAS variables are recovered by DASCH. Among the objects with more than 10 good measurements in DASCH, 92% of ASAS variables with DASCH light curve rms > 0.25 mag are found to be variables in DASCH. Some variables not included in the

ASAS variables are also found. Several example variables are presented.

7.1 Introduction

A primary motivation of the DASCH project is to find variable objects, analyze their variability, and to study the physical processes involved. We have scanned and processed over 3000 plates in the Kepler field of view (FOV), chosen to overlap with the Kepler mission. The Kepler and DASCH surveys have similar brightness range (V$\sim 9-16$). Combining the long-term variations from DASCH, and the short-term variations from the extremely accurate Kepler data, enables a unique study of stellar variability on the widest range of timescale.

In this chapter, I describe the variable search algorithms, and present the preliminary results in a Catalog of Kepler-DASCH variables in the Kepler FoV. Several example variables are also shown.

7.2 Variable Search Algorithms

7.2.1 Division of sub-fields

The search for variables makes use of the light curve statistics in the summary ID table, as described in Chapter 2.7. Due to the inhomogeneous coverage of the plates, as shown in Figure 2.1, we need to compare the light curve statistics locally. We first divided the Kepler FOV into 21 sub-fields, each corresponds to 4 CCDs in the Kepler mission, as shown in Figure 7.1. Note that the star number density differs

from sub-field to sub-field, for example, sub-field 18 has the highest star number density as it is closest to the galactic plane.

7.2.2 Excluding spurious light curves

Next, we remove the highly spurious light curves with much larger variations in RA and Dec, or much stronger correlation between magnitude measurements and positions, compared with other neighbor stars. These objects show higher level of variability, high likely polluted by blends, or wrong matches. We also remove the spurious light curves with strong negative correlation between magnitude measurements and plate limiting magnitudes, i.e. appear brighter on deeper plates, which are likely polluted by blending of neighbor faint stars, or non-point sources such as galaxies or nebulae. The distribution of the above qualities are shown in Figures $7.2 - 8$. We used 4σ as the threshold, as shown in vertical black lines in Figures $7.2 - 8$.

7.2.3 Outliers in light curve statistics

After removing dubious light curves in last subsection, we now select variable candidates with excess variability compared with neighbor stars with similar magnitudes. I used 21 different sets of criteria, to select objects with excess variability as indicated by their statistical measurements, including light curve rms, amplitude, number of dip or outburst points with different thresholds, number of adjacent points in a single dip or outburst, and trends in the light curves. The definition of these measurements are listed in Chapter 2.7. I applied the criteria

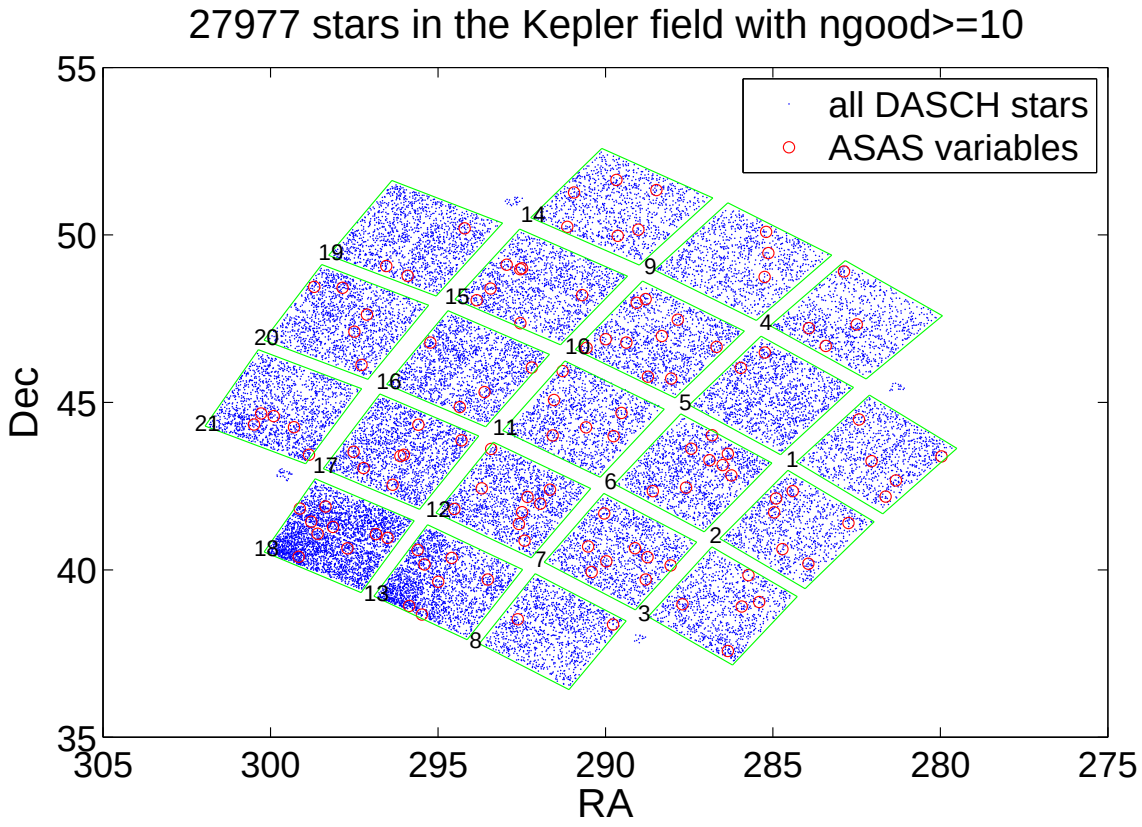

Figure 7.1.— The Kepler field FOV and the division of 21 sub-fields. Blue dots are stars with ≥ 10 good points in DASCH light curves, and red open circles are ASAS variables (Pigulski et al. 2009) with $\Delta V \geq 0.4$ mag and ≥ 10 good points in DASCH light curves.

to the 20 sub-fields separately, as defined in Figure 7.1. The selection in sub-field 19 are shown in Figures $7.9 - 29$ as examples. Light curves are divided into 8 bins in number of good points (upper panels), or KIC g mag (lower panels), with equal number (exact or ± 1) of objects in each bin. Then the σ and the thresholds are calculated separately for each bin after two iterations of 5σ clipping. Blue dots are all objects, red circles are ASAS variables with $\Delta V \geq 0.4$ mag. Stars are divided into 8 bins in number of good points (upper panel), or KIC g mag (lower panel), Green horizontal dashed lines marks the threshold, which differs from 5σ to 8σ, or are different number of points, in different measurements. Green diamonds are variable candidates which are above the threshold and get selected. In sub-field 19, all the three ASAS variables with $\Delta V > 0.4$ mag are above the thresholds in at least one measurements, and thus are selected for further study.

Different statistical measurements are sensitive to different types of variables. For example, light curve rms and amplitude are sensitive to pulsating stars, numbers of outburst points are sensitive to flare stars, numbers of dip points are sensitive to eclipsing binaries, while the light curve rms ratios before and after detrending are sensitive to long-term variables. Large amplitude variables such as Miras, stand out as outliers in most of the measurements, as shown in Figures $7.9 - 29$, while smaller amplitude variables may only be selected by one or a few of the measurements.

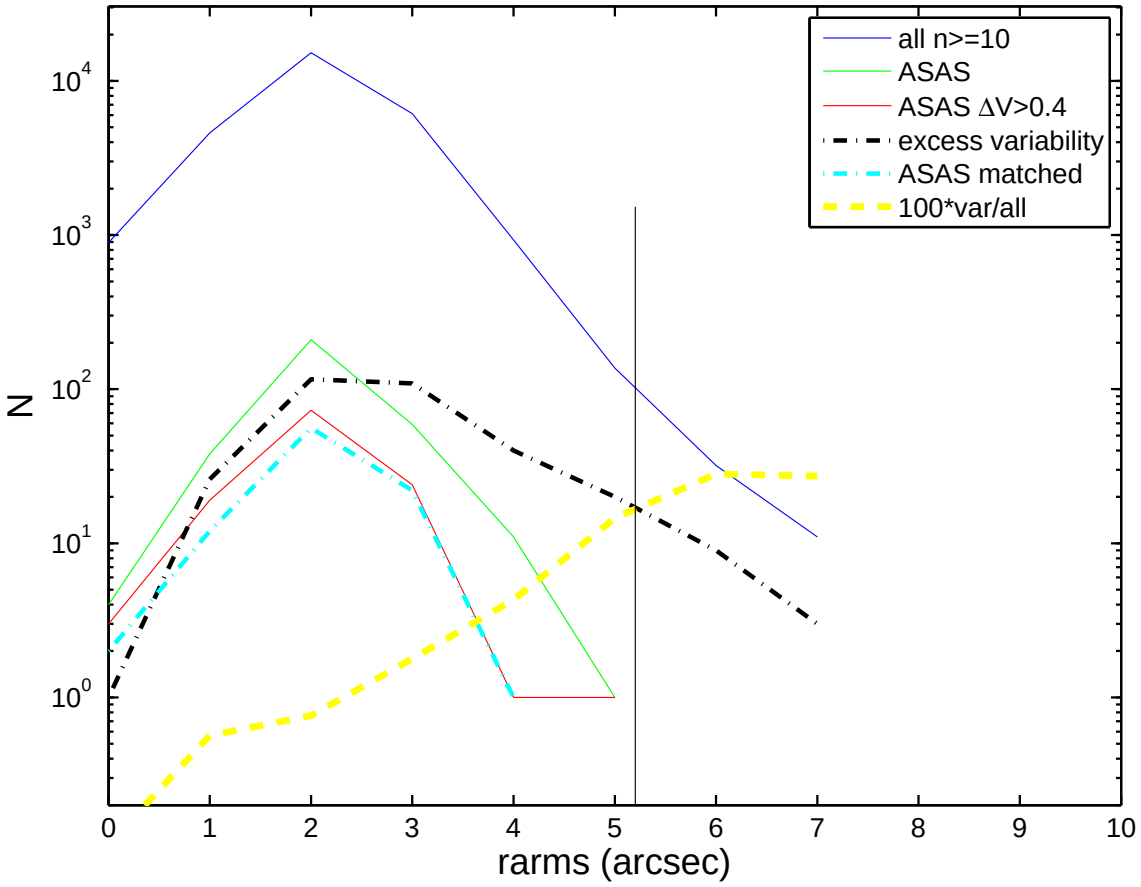

Figure 7.2.— Histogram of rms in RA for stars with $n \geq 10$ good points in the Kepler field. Objects with higher rms in RA are more likely to be contaminated by blending or mis-match. Blue solid line is for all stars with $n \geq 10$, green solid line is for ASAS variables (Pigulski et al. 2009), red solid line is for ASAS variables with $\Delta V \geq 0.4$ mag, black dash-dotted line is for stars showing excess variations in DASCH light curves, cyan dash-dotted line is for ASAS variables which are included in the preliminary variable candidates, and yellow dashed line is the percentage of the preliminary variable candidates over all stars. The rising of the yellow dashed line suggests that stars with large rms in RA show higher level of variability in their light curves, which are dubious due to possible contamination from blends.

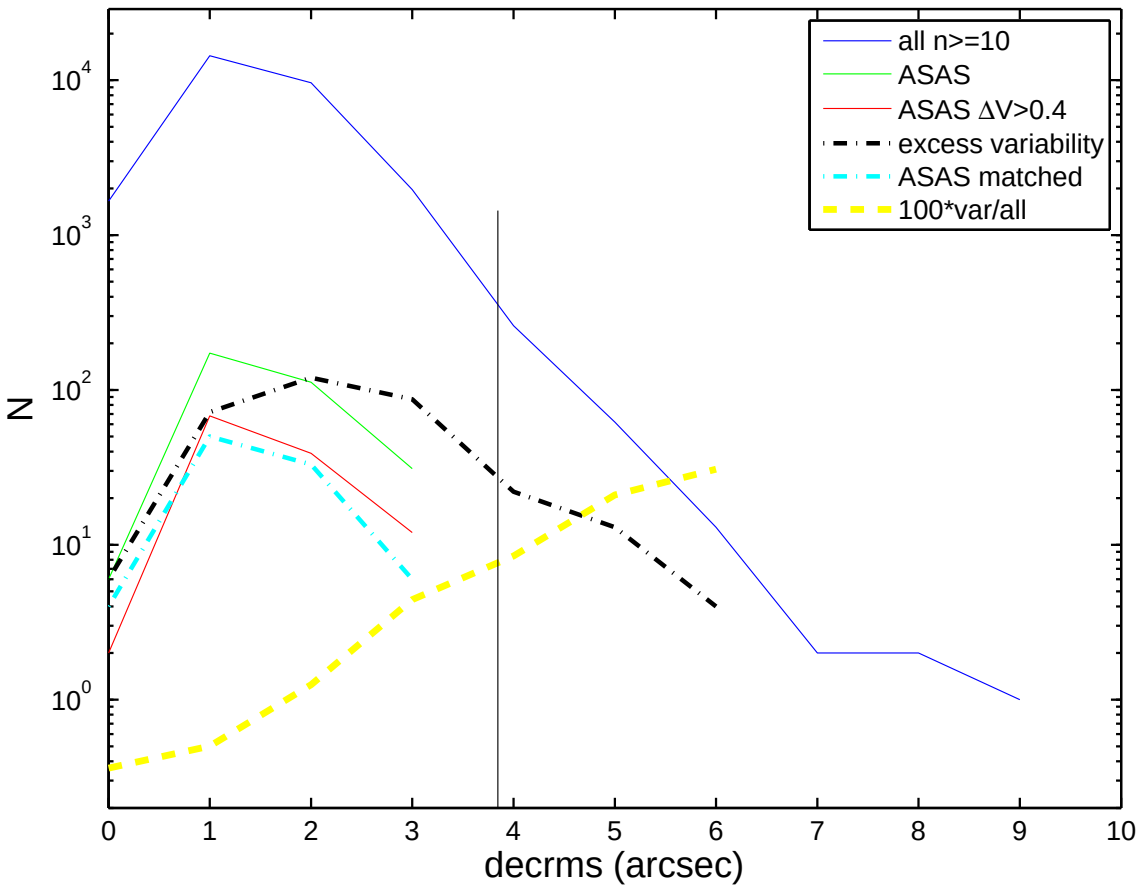

Figure 7.3.— Histogram of rms in Dec for stars with $n \geq 10$ good points in the Kepler field. Objects with higher rms in RA are more likely to be contaminated by blending or mis-match. Symbols are similar as Figure 7.2.

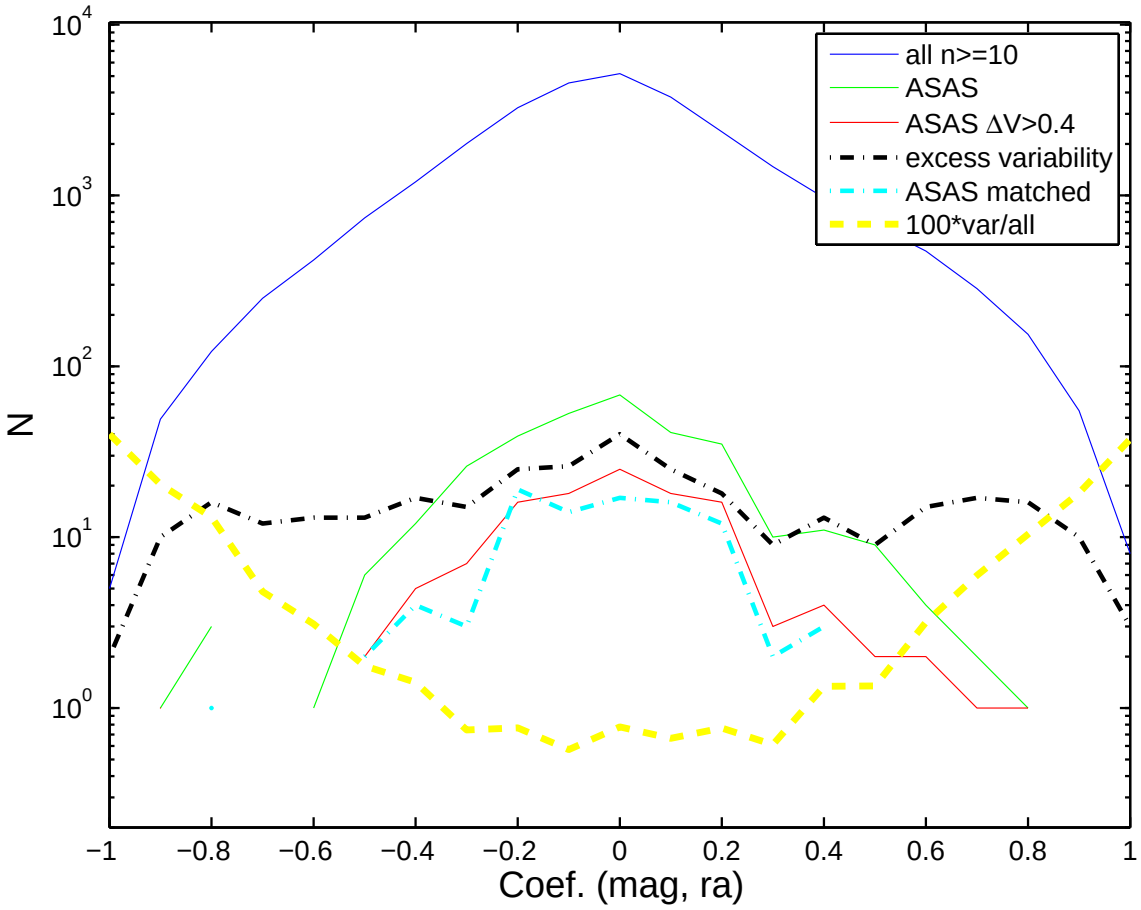

Figure 7.4.— Histogram of correlation coefficient between magnitude and RA for stars with $n \geq 10$ good points in the Kepler field. Objects with higher absolute values of correlation coefficient are more likely to be contaminated by blending. Symbols are similar to Figure 7.2.

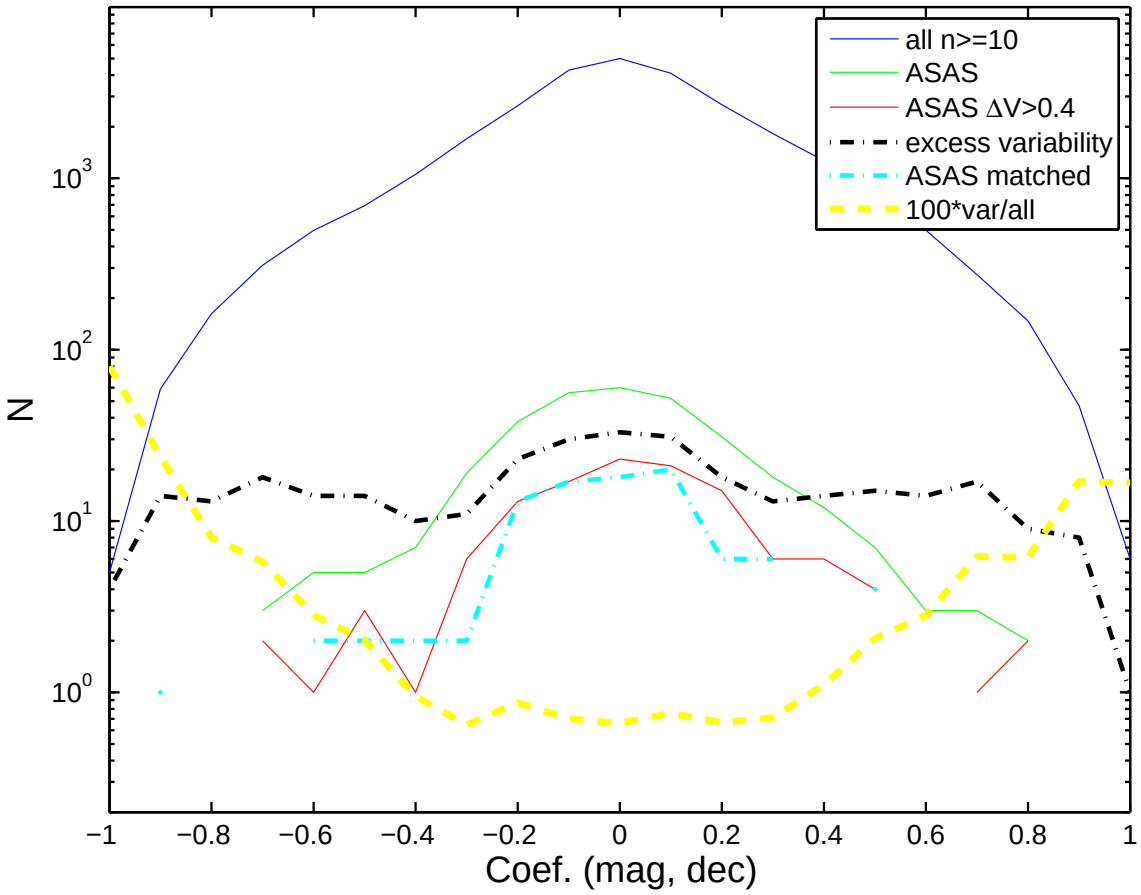

Figure 7.5.— Histogram of correlation coefficient between magnitude and Dec for stars with $n \geq 10$ good points in the Kepler field. Objects with higher absolute values of correlation coefficient are more likely to be contaminated by blending. Symbols are similar to Figure 7.2.

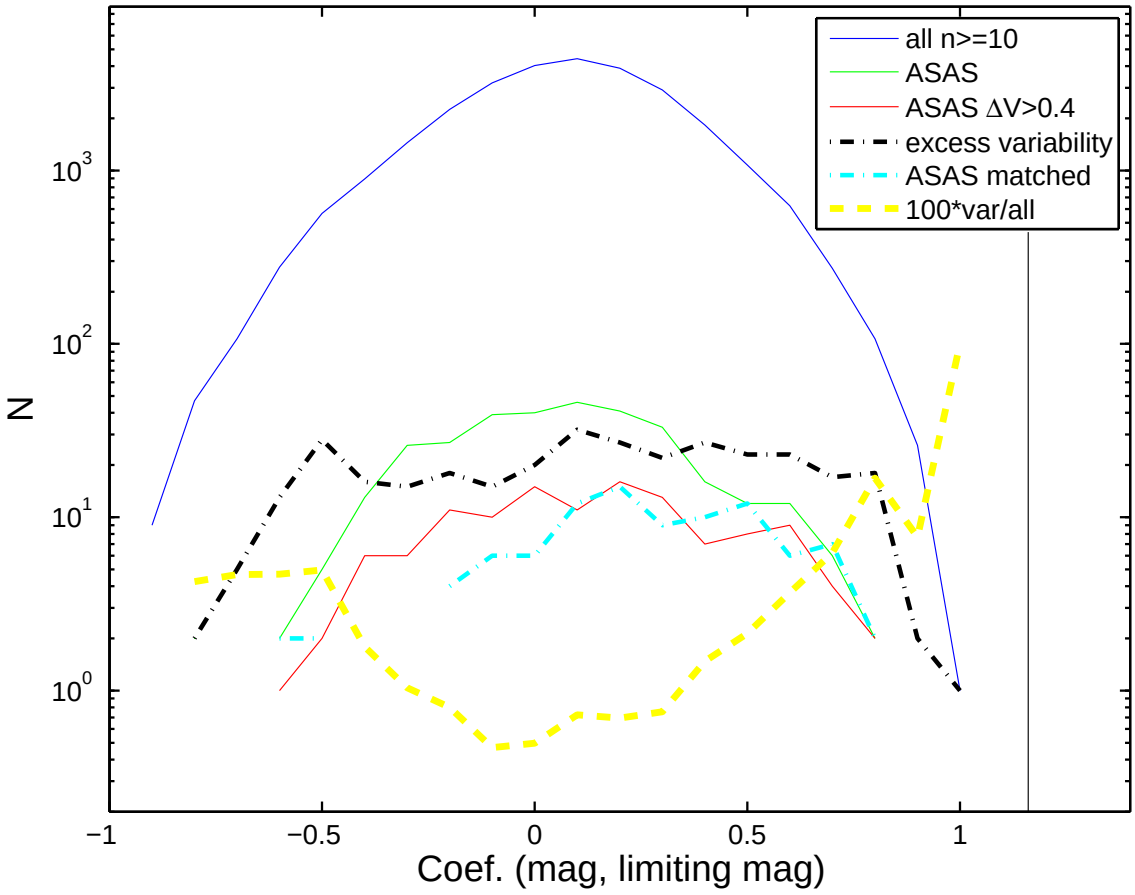

Figure 7.6.— Histogram of correlation coefficient between magnitude and plate limiting magnitude for stars with $n \geq 10$ good points in the Kepler field. Objects with higher negative values of correlation coefficient, i.e. appear brighter on deeper plates, are more likely to be contaminated by blending of neighbor faint stars, or non-point sources such as galaxies or nebulae. Objects with higher positive values of correlation coefficient, i.e. appear fainter on deeper plates, are more likely to be contaminated by noise; although selection effect of real variables also contributes to a positive correlation coefficient, as they are more likely to be observed on deeper plates when they are in fainter phases. Symbols are similar to Figure 7.2.

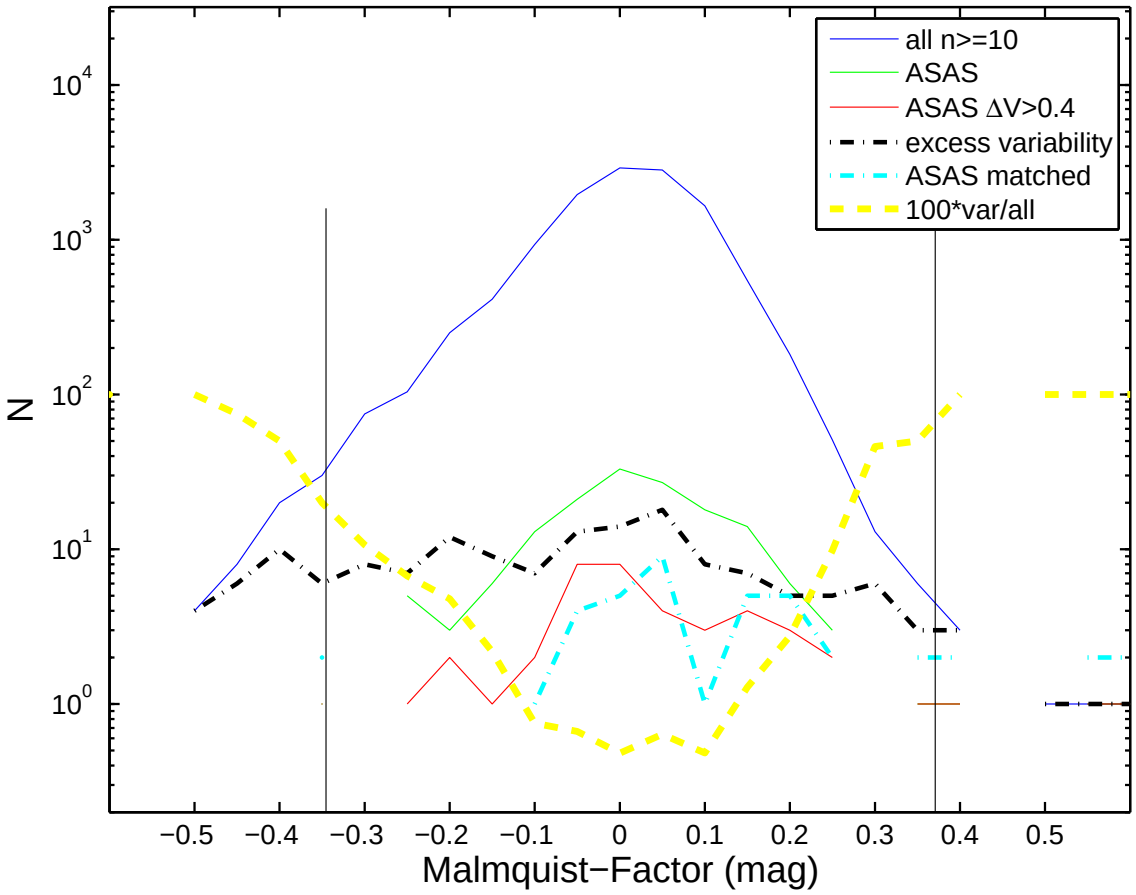

Figure 7.7.— Histogram of clipped median DASCH magnitude of 20 deepest plates − clipped median DASCH magnitude of 20 shallowest plates using 'good' points. Objects with larger absolute values are more likely to be contaminated by blending or noise. Symbols are similar to Figure 7.2.

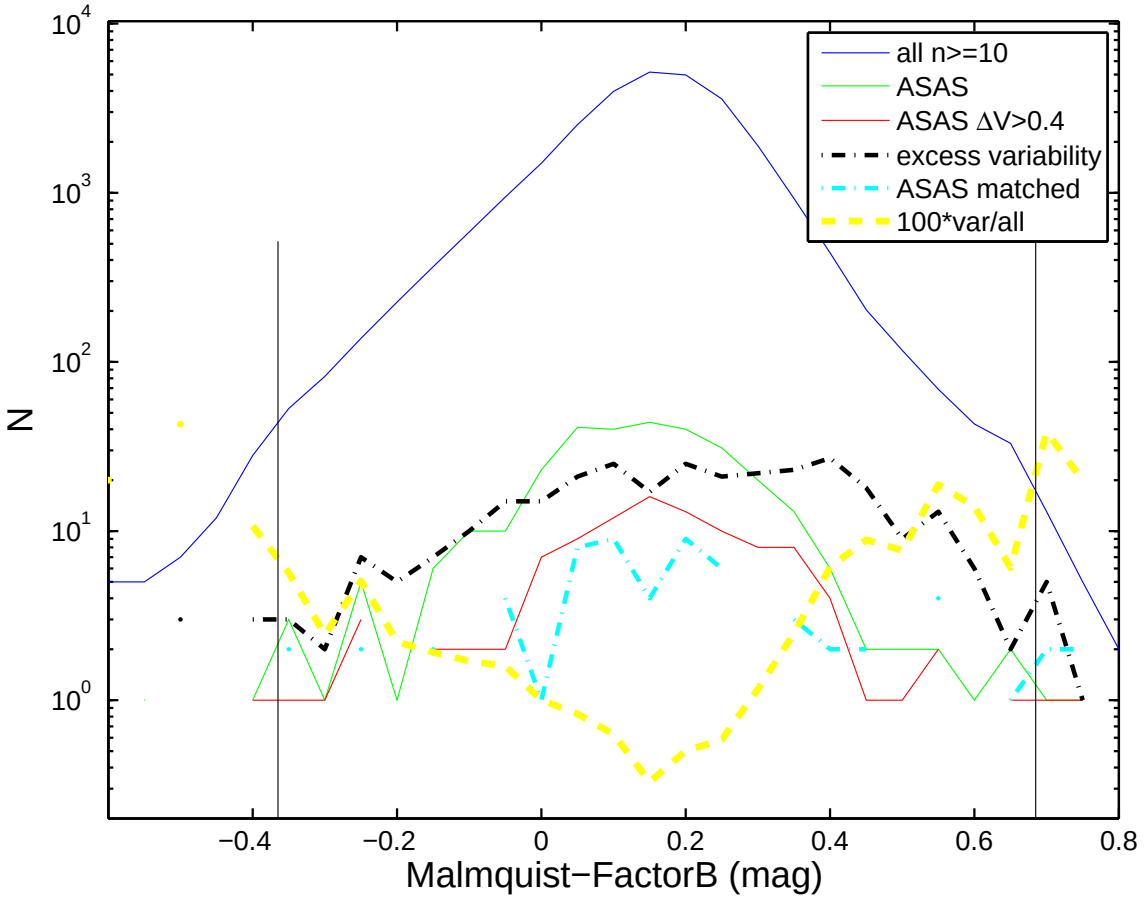

Figure 7.8.— Similar to Figure 7.7, but also includes defects, low altitude, uncertain date and second quality plates. Objects with larger absolute values are more likely to be contaminated by blending or noise. Symbols are similar to Figure 7.2.

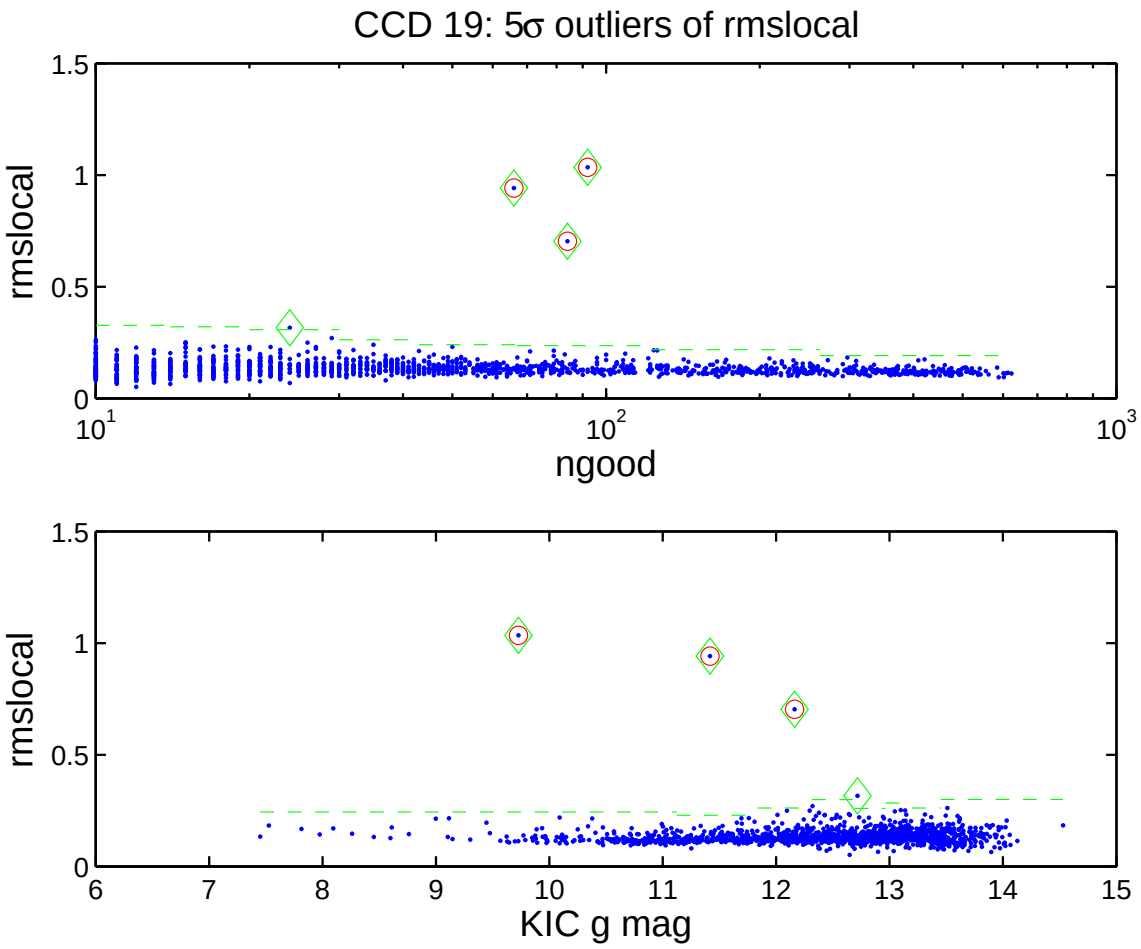

Figure 7.9.— Light curve rms using all points vs number of good points (upper panel), and KIC g mag (lower panel). Blue dots are all objects, red circles are ASAS variables with $\Delta V \geq 0.4$ mag (here all the three are Miras), and green diamonds mark the variable candidates which are selected. Stars are divided into 8 bins in number of good points (upper panel), or KIC g mag (lower panel), with equal number (exact or ± 1) of objects in each bin. Then the σ and the thresholds (green horizontal dashed lines; 5σ here) are calculated separately for each bin.

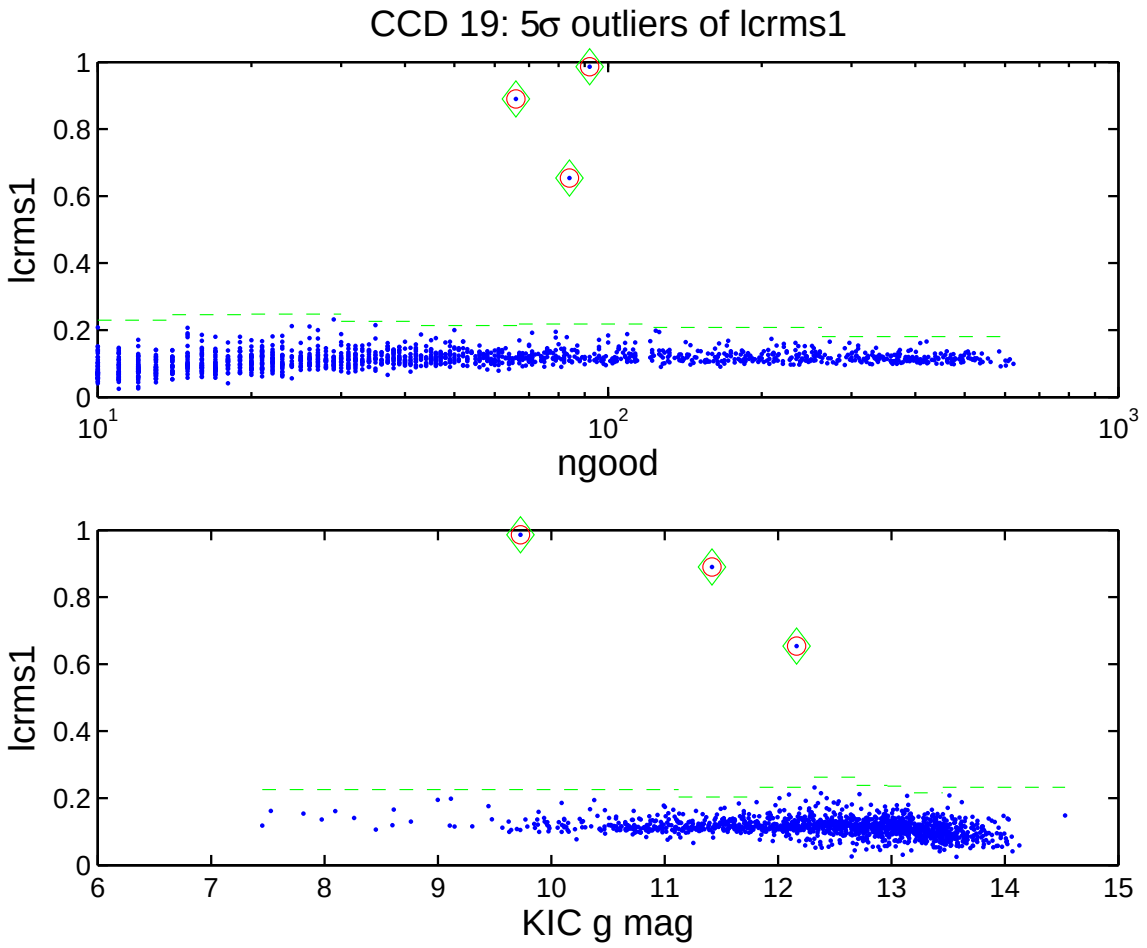

Figure 7.10.— Light curve rms calculated only using good points vs number of good points (upper panel), and KIC g mag (lower panel). Symbols are the same as Figure 7.9.

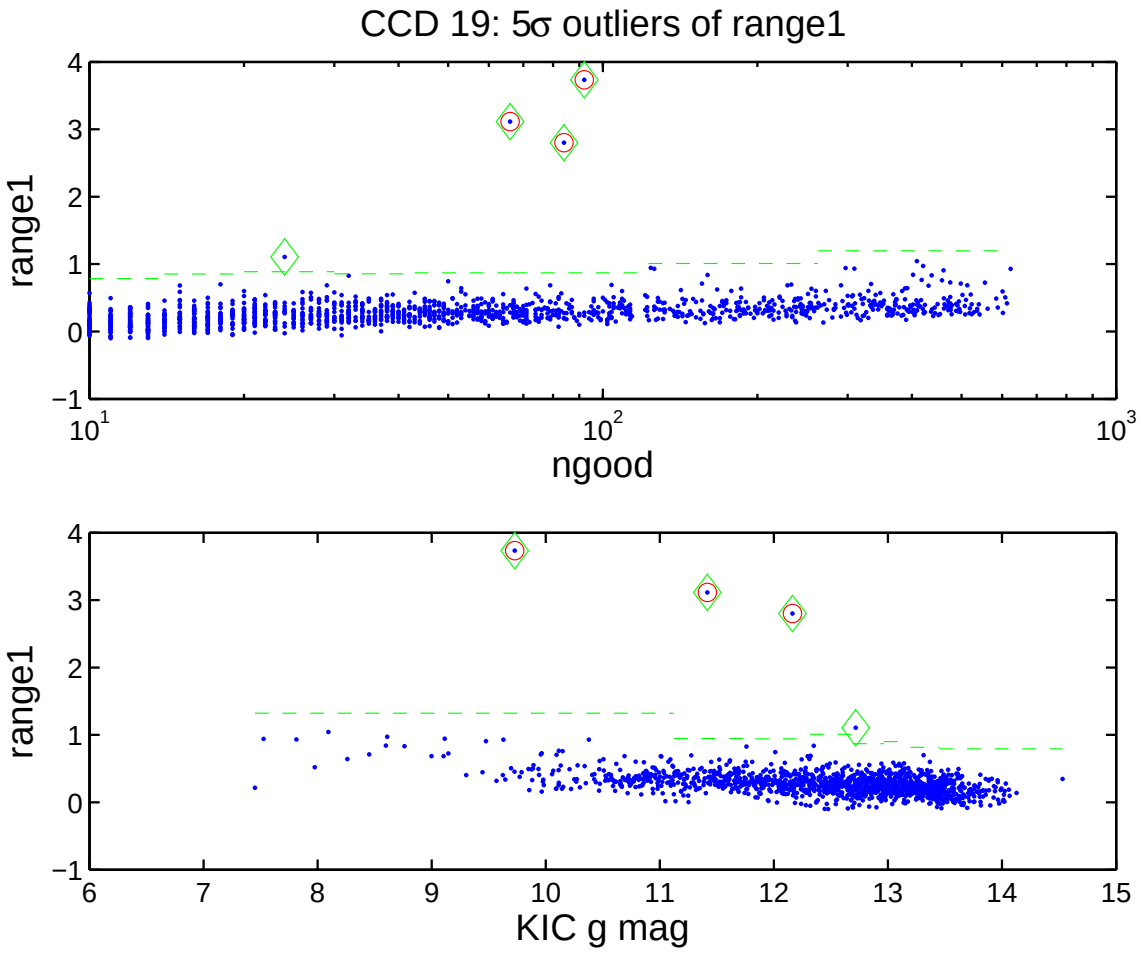

Figure 7.11.— Measurement *range_local* vs number of good points (upper panel), and KIC g mag (lower panel). *range_local* is defined as the difference between the brightest and the faintest points, minus the sum of their errors. Symbols are the same as Figure 7.9.

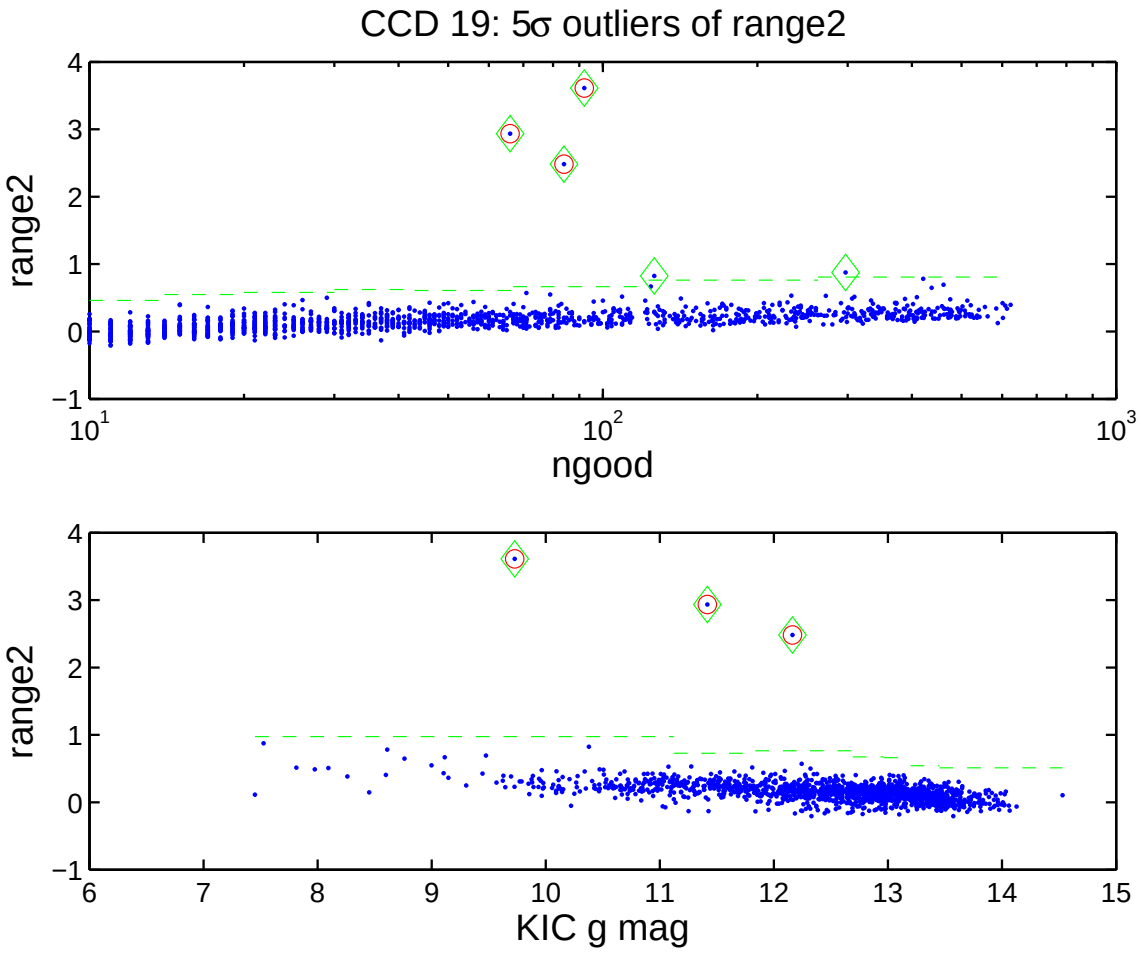

Figure 7.12.— Measurement *range_local*2 vs number of good points (upper panel), and KIC g mag (lower panel). *range_local* is defined as the difference between the brightest and the faintest points, minus the sum of their errors. Symbols are the same as Figure 7.9.

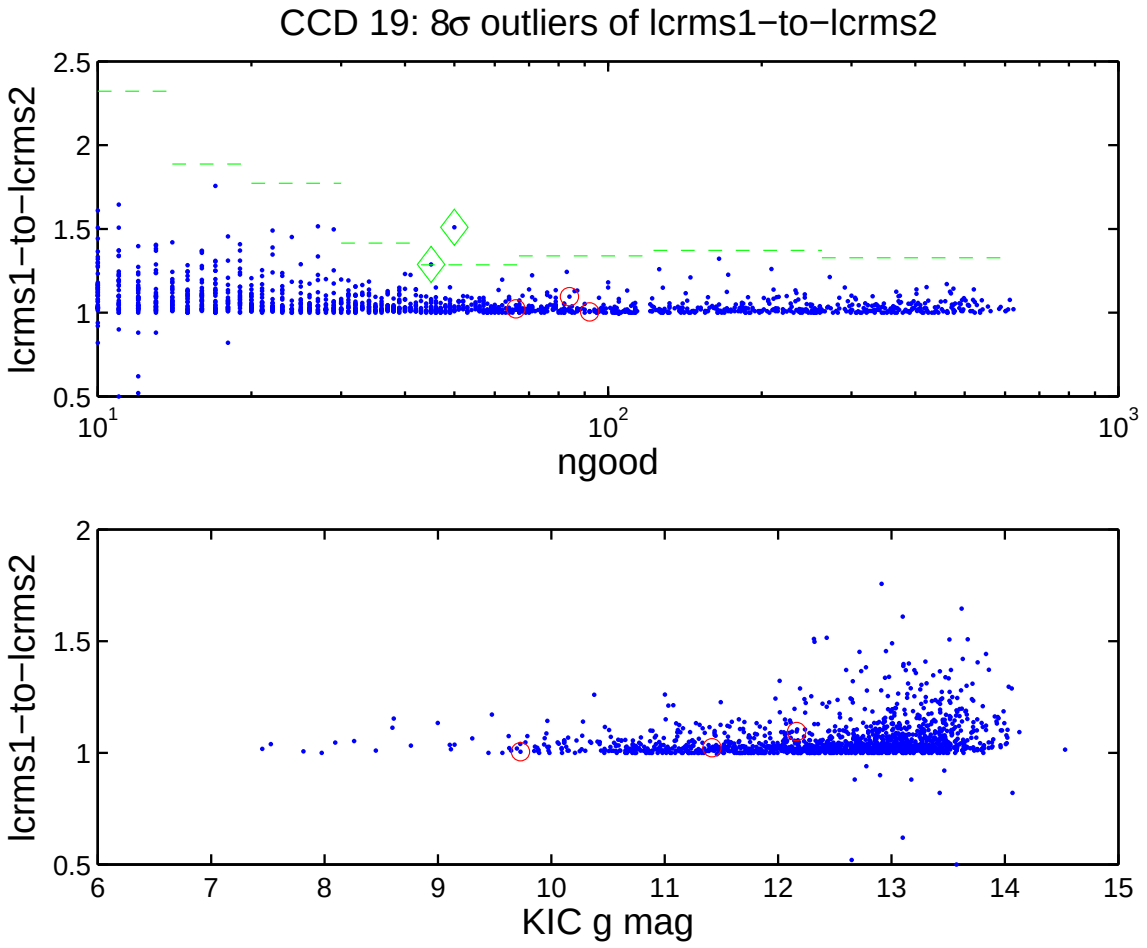

Figure 7.13.— Measurement lightcurverms1 over lcrms2 vs number of good points (upper panel), and KIC g mag (lower panel). *lightcurverms*1 is the rms after 4 iterations of 5σ clipping, and *lightcurverms*2 rms of light curve residuals after detrending using smooth(x,y,0.4, 'lowess'). Symbols are the same as Figure 7.9.

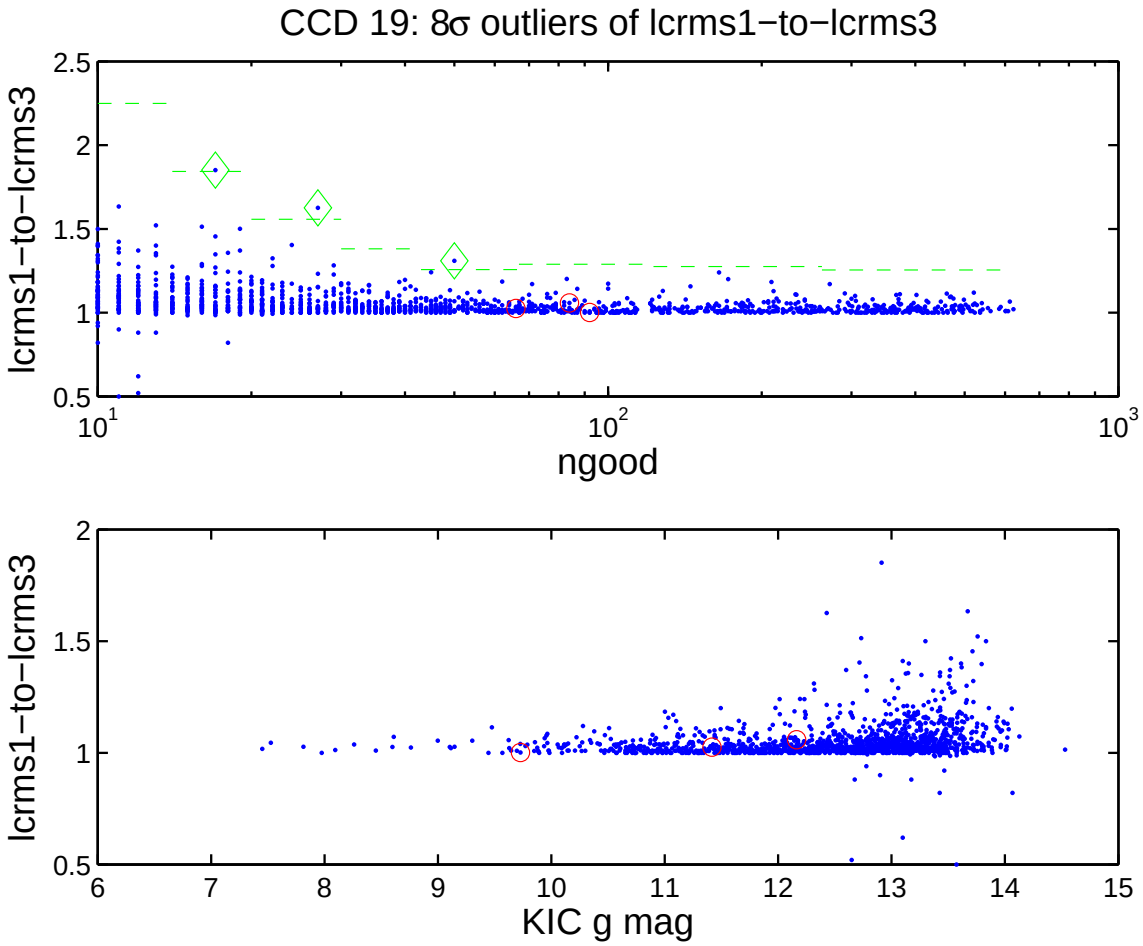

Figure 7.14.— Measurement lightcurverms1 over lightcurverms3 vs number of good points (upper panel), and KIC g mag (lower panel). *lightcurverms*1 is the rms after 4 iterations of 5σ clipping, and *lightcurverms*3 rms of light curve residuals after de-trending using smooth(y,0.8, 'lowess'). Symbols are the same as Figure 7.9.

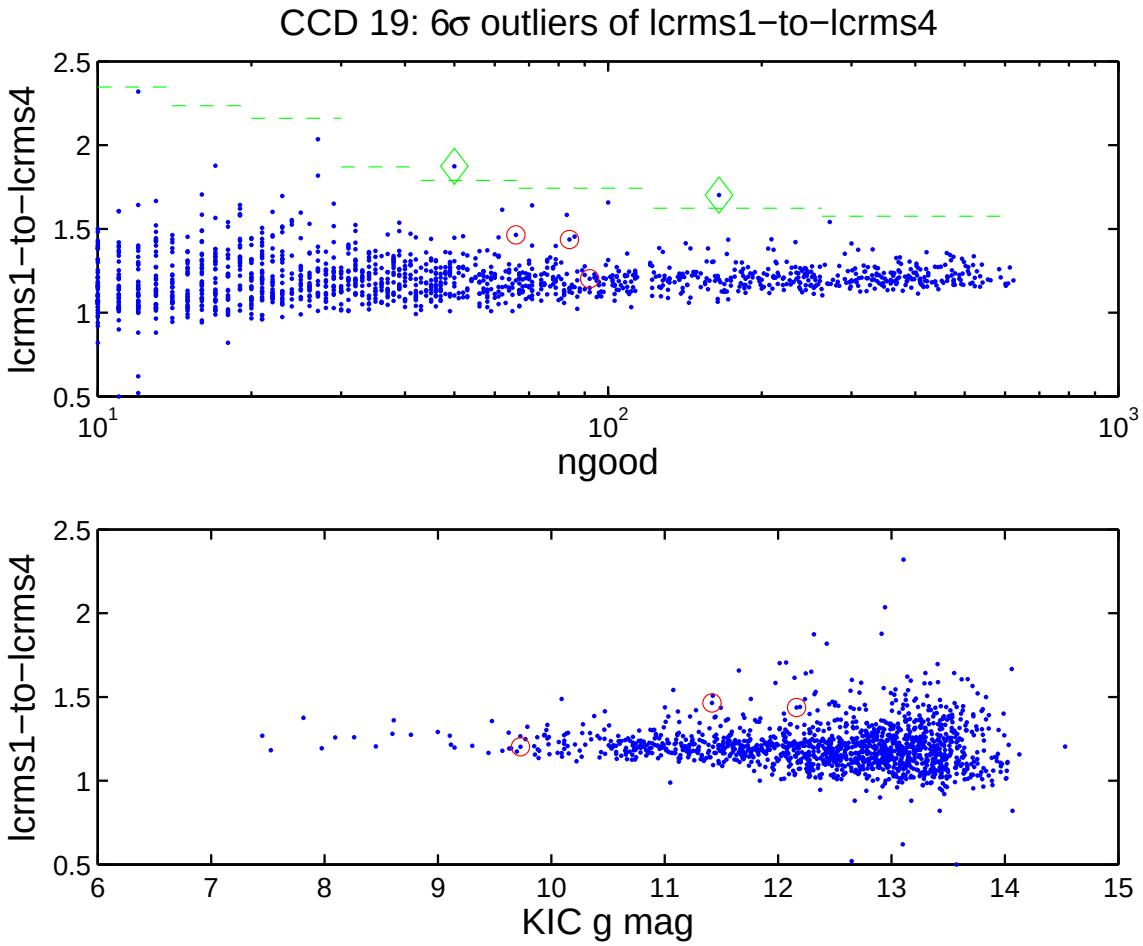

Figure 7.15.— Measurement lightcurverms1 over lightcurverms4 vs number of good points (upper panel), and KIC g mag (lower panel). *lightcurverms*1 is the rms after 4 iterations of 5σ clipping, and *lightcurverms*4 rms of light curve residuals after de-trending using smooth(y,10, 'sgolay'). Symbols are the same as Figure 7.9.

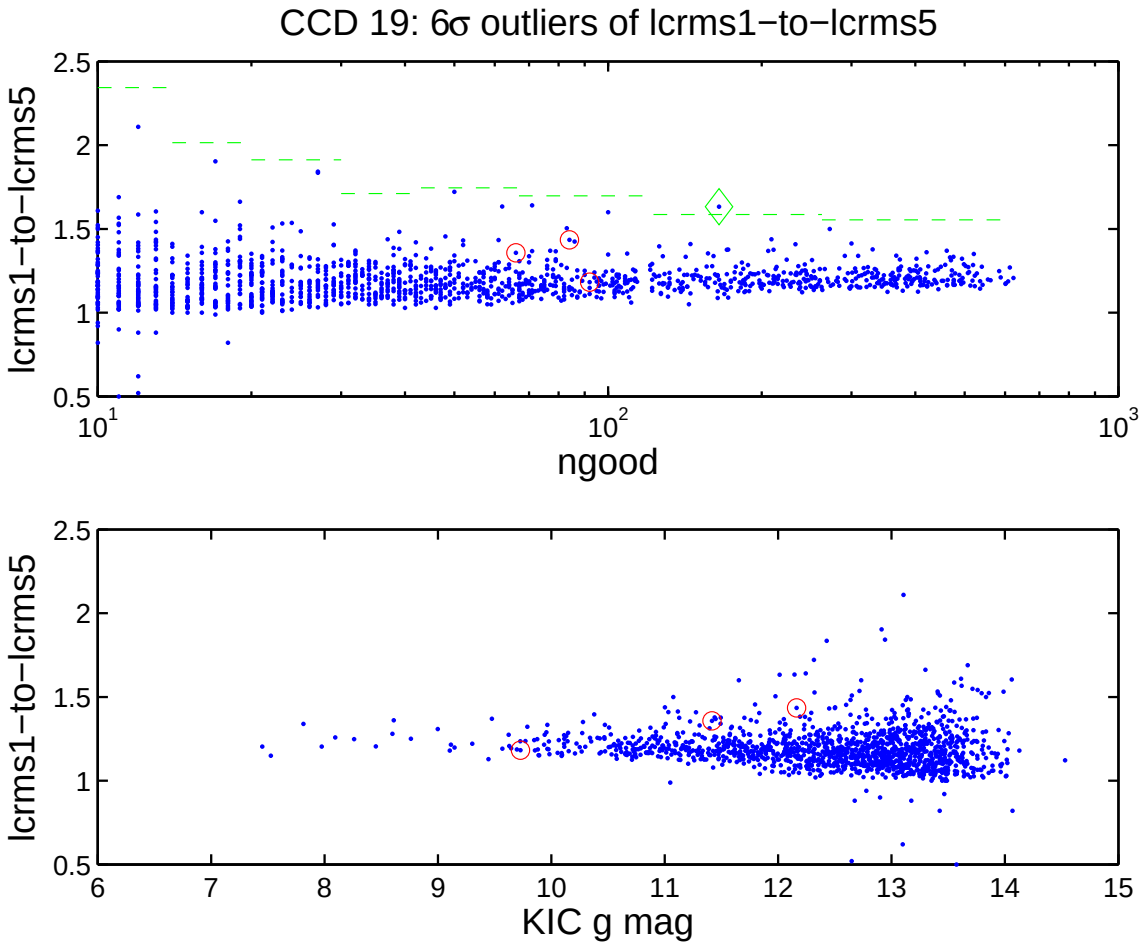

Figure 7.16.— Measurement lightcurverms1 over lightcurverms5 vs number of good points (upper panel), and KIC g mag (lower panel). *lightcurverms*1 is the rms after 4 iterations of 5σ clipping, and *lightcurverms*5 rms of light curve residuals after de-trending using smooth(y,15, 'loess'). Symbols are the same as Figure 7.9.

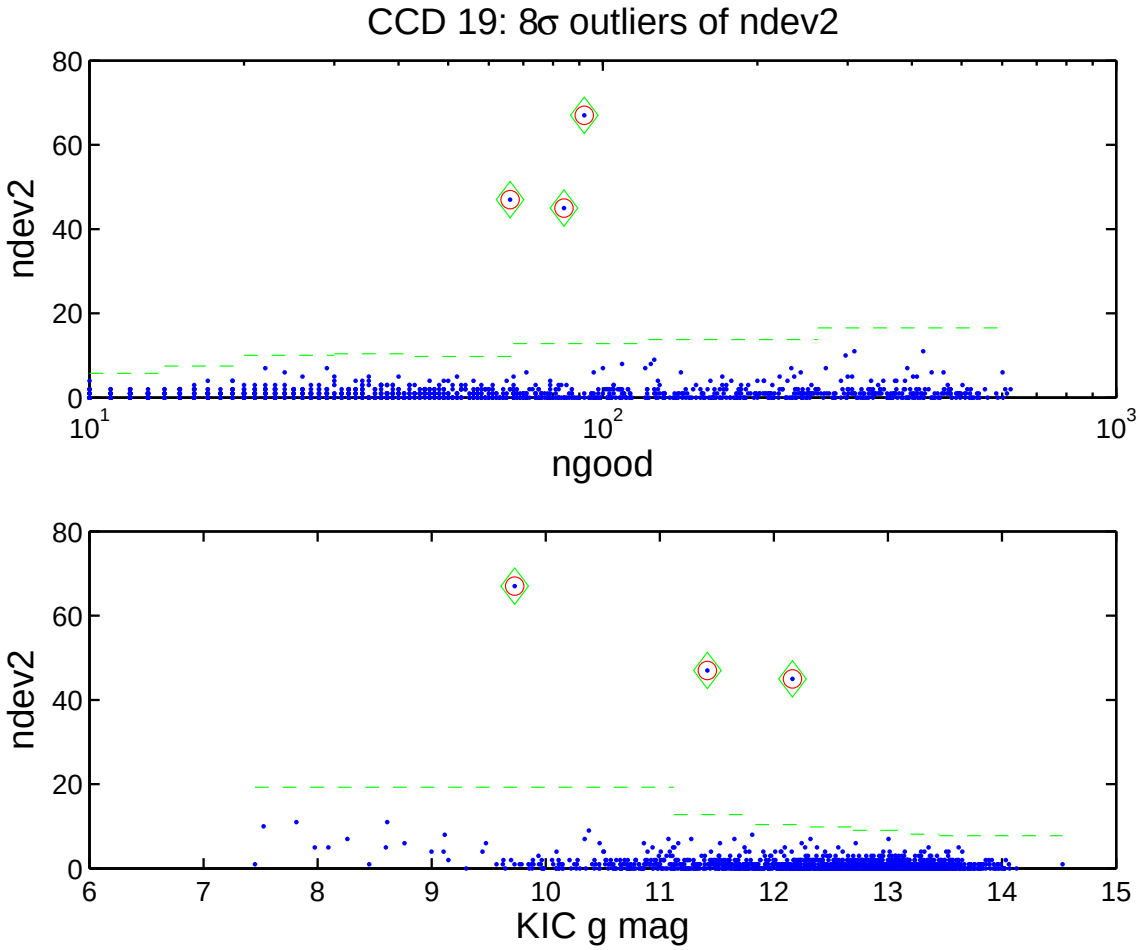

Figure 7.17.— Measurement ndev2 vs number of good points (upper panel), and KIC g mag (lower panel). *ndev*2 is defined as the number of points $\geq 2\sigma$ brighter or fainter than the median value. Symbols are the same as Figure 7.9.

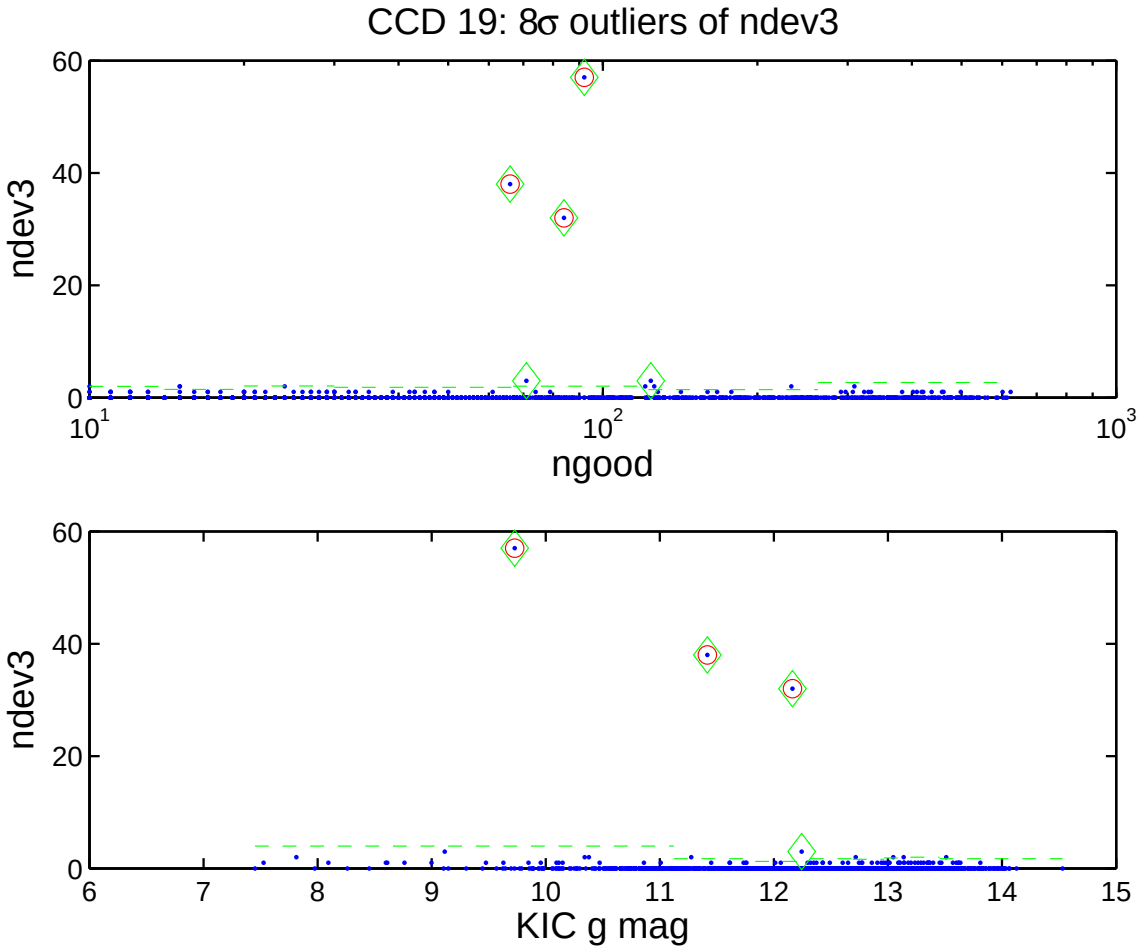

Figure 7.18.— Measurement ndev3 vs number of good points (upper panel), and KIC g mag (lower panel). *ndev*3 is defined as the number of points $\geq 3\sigma$ brighter or fainter than the median value. Symbols are the same as Figure 7.9.

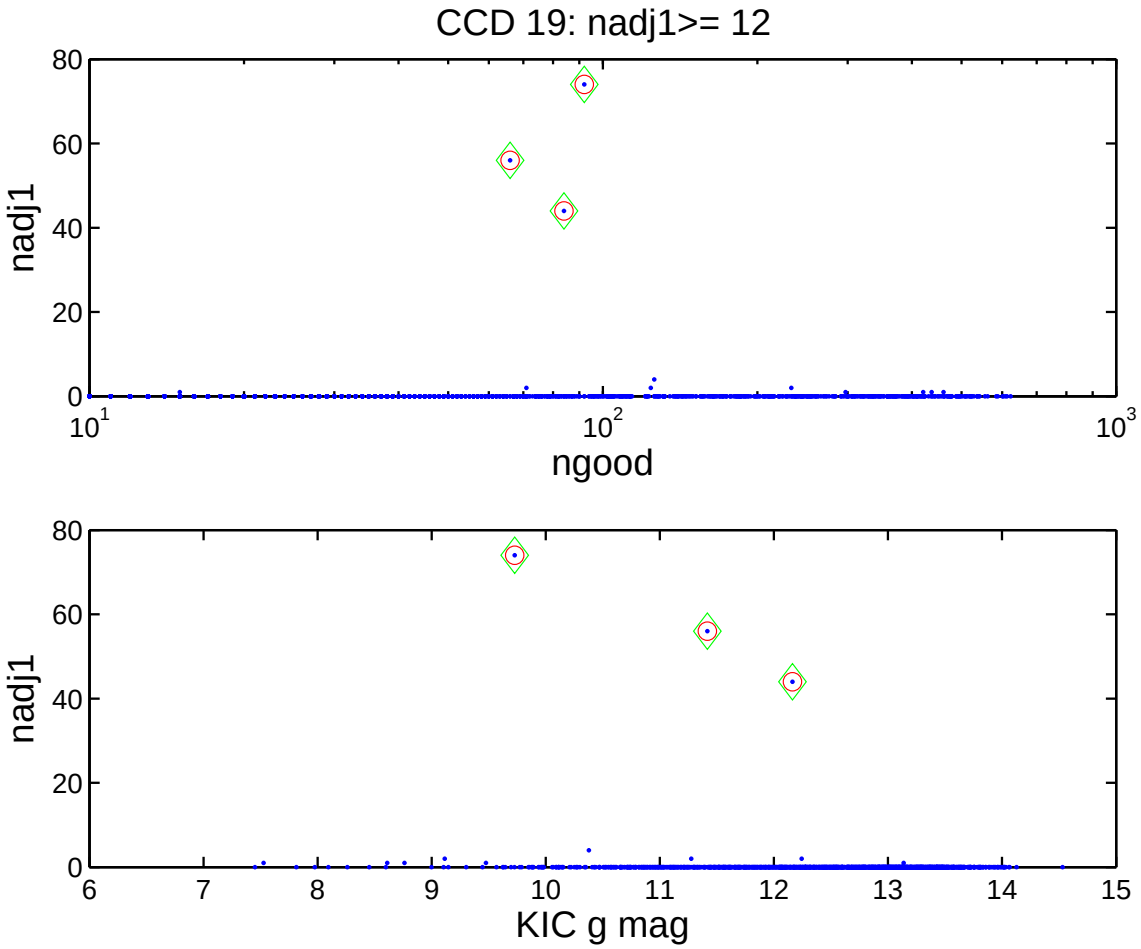

Figure 7.19.— Measurement nadj1 vs number of good points (upper panel), and KIC g mag (lower panel). *nadj*1 is a measure of the number of adjacent nburst3/4 and ndip3/4 points. Symbols are the same as Figure 7.9.

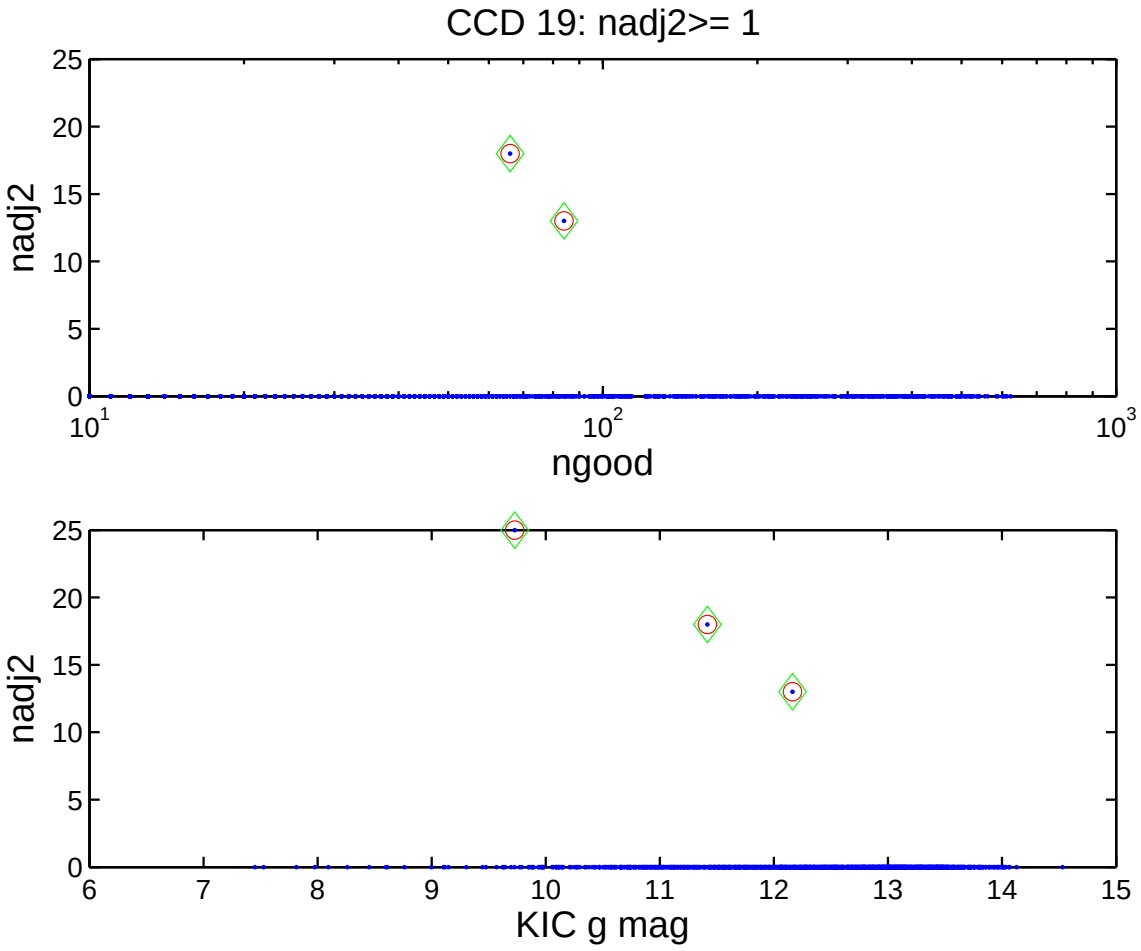

Figure 7.20.— Measurement nadj2 vs number of good points (upper panel), and KIC g mag (lower panel). *nadj*2 is a measure of the number of > 5 adjacent nburst3/4 and ndip3/4 points. Symbols are the same as Figure 7.9.

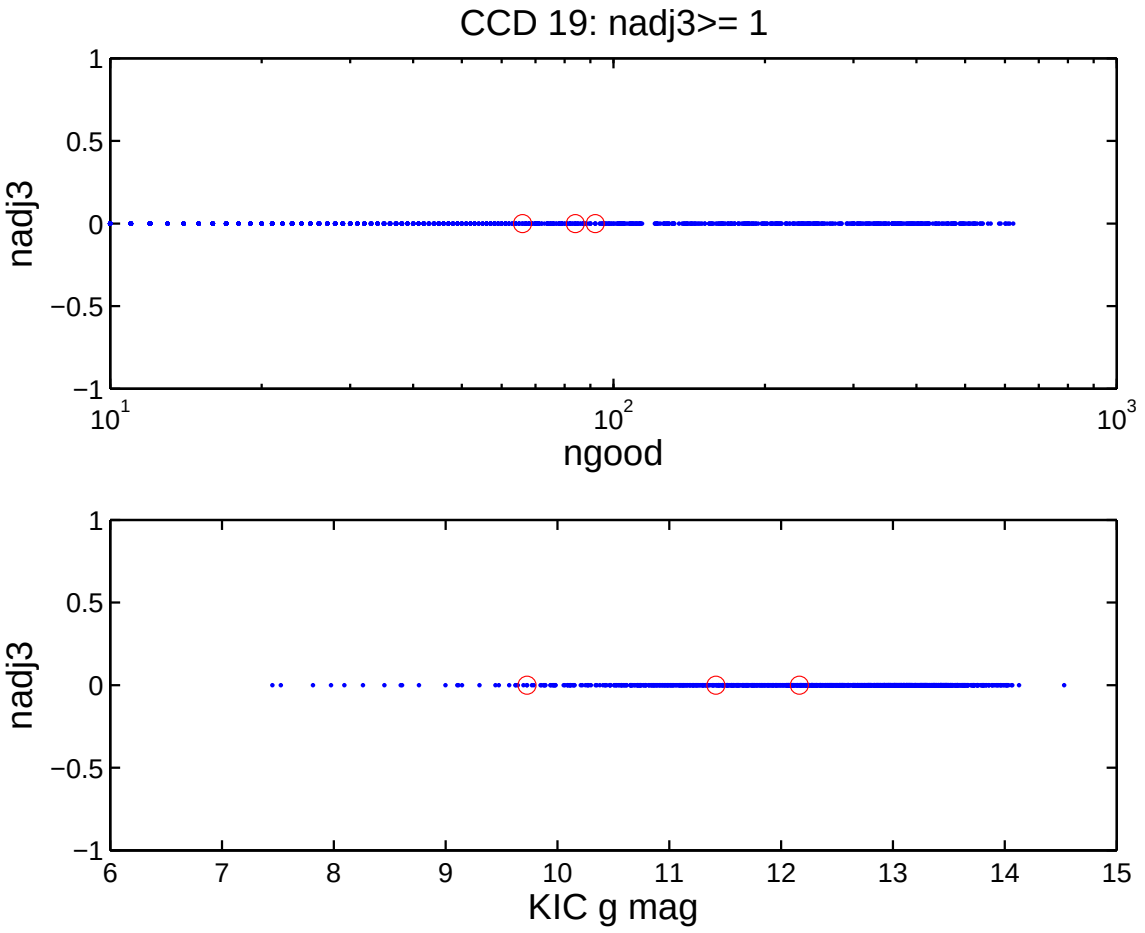

Figure 7.21.— Measurement nadj3 vs number of good points (upper panel), and KIC g mag (lower panel). *nadj*3 is a measure of the number of > 7 adjacent nburst3/4 and ndip3/4 points. Symbols are the same as Figure 7.9.

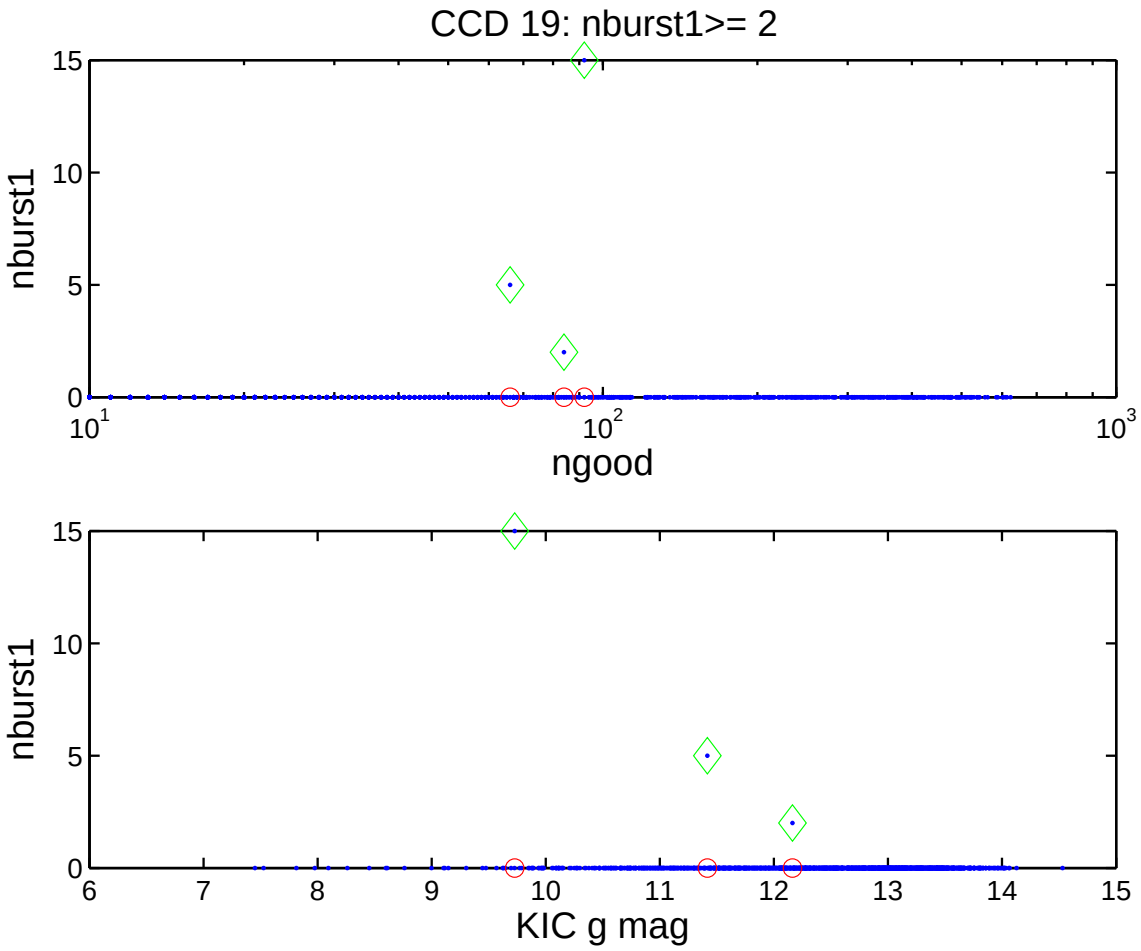

Figure 7.22.— Measurement nburst1 vs number of good points (upper panel), and KIC g mag (lower panel). *nburst*1 is defined as the number of points $\geq$ 0.8 mag brighter than the median value. Symbols are the same as Figure 7.9.

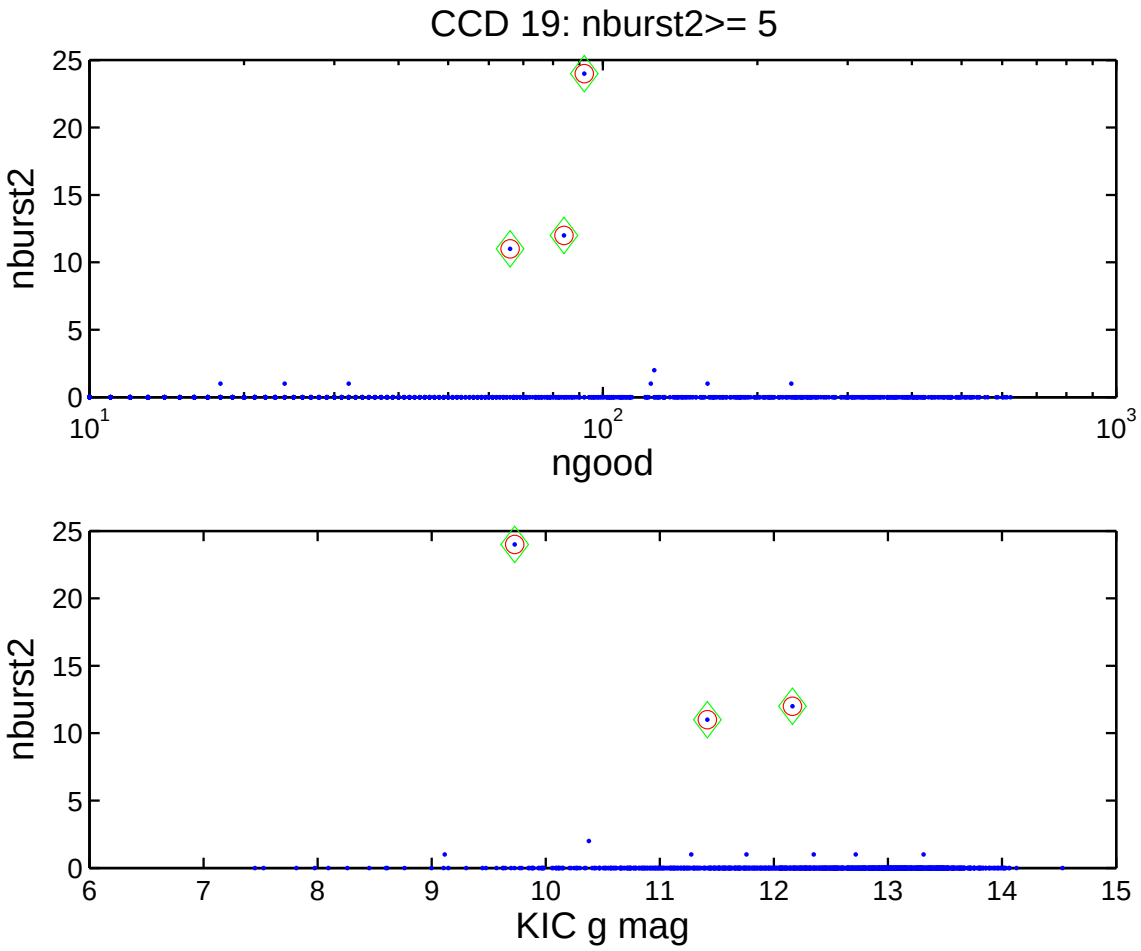

Figure 7.23.— Measurement nburst2 vs number of good points (upper panel), and KIC g mag (lower panel). *nburst*2 is defined as the number of points $\geq$ 0.5 mag brighter than the median value. Symbols are the same as Figure 7.9.

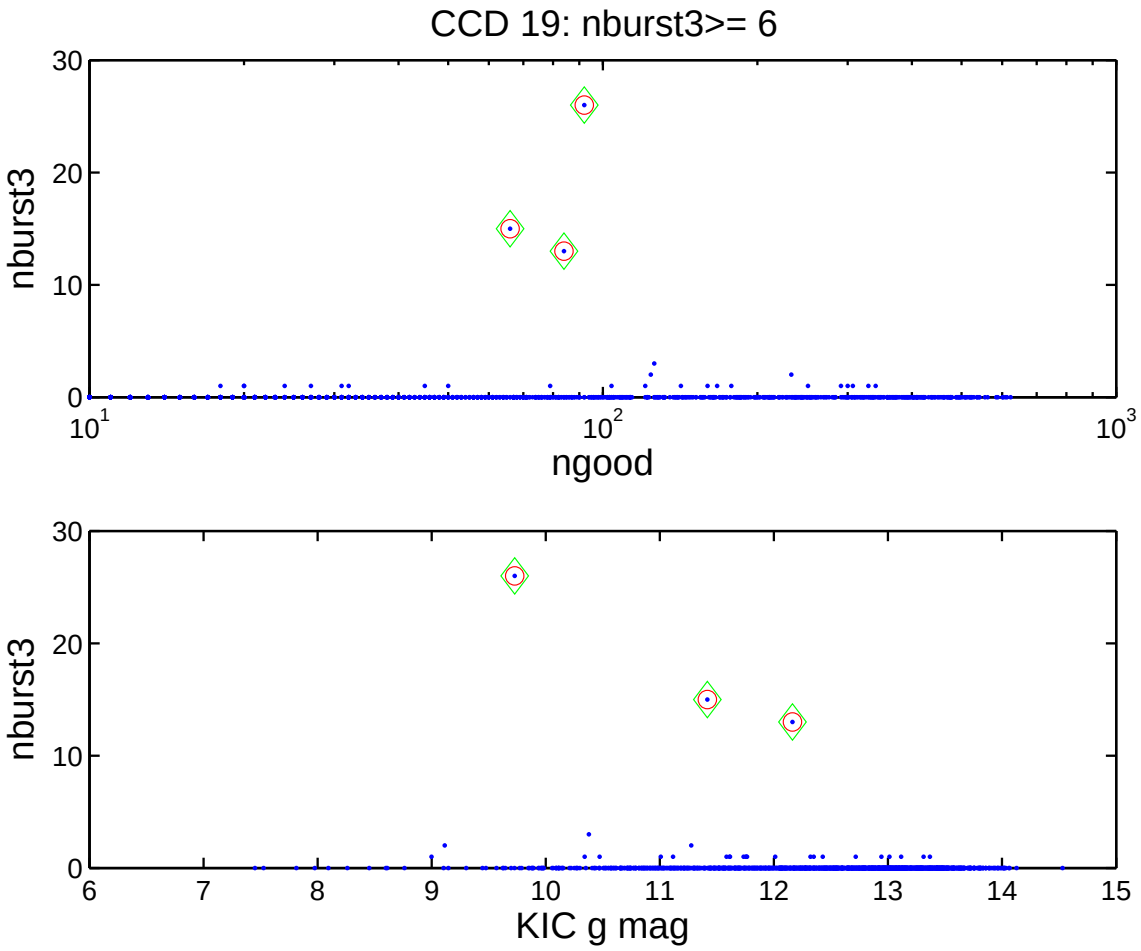

Figure 7.24.— Measurement nburst3 vs number of good points (upper panel), and KIC g mag (lower panel). *nburst*3 is defined as the number of points $\geq$ 0.4 mag brighter than the median value. Symbols are the same as Figure 7.9.

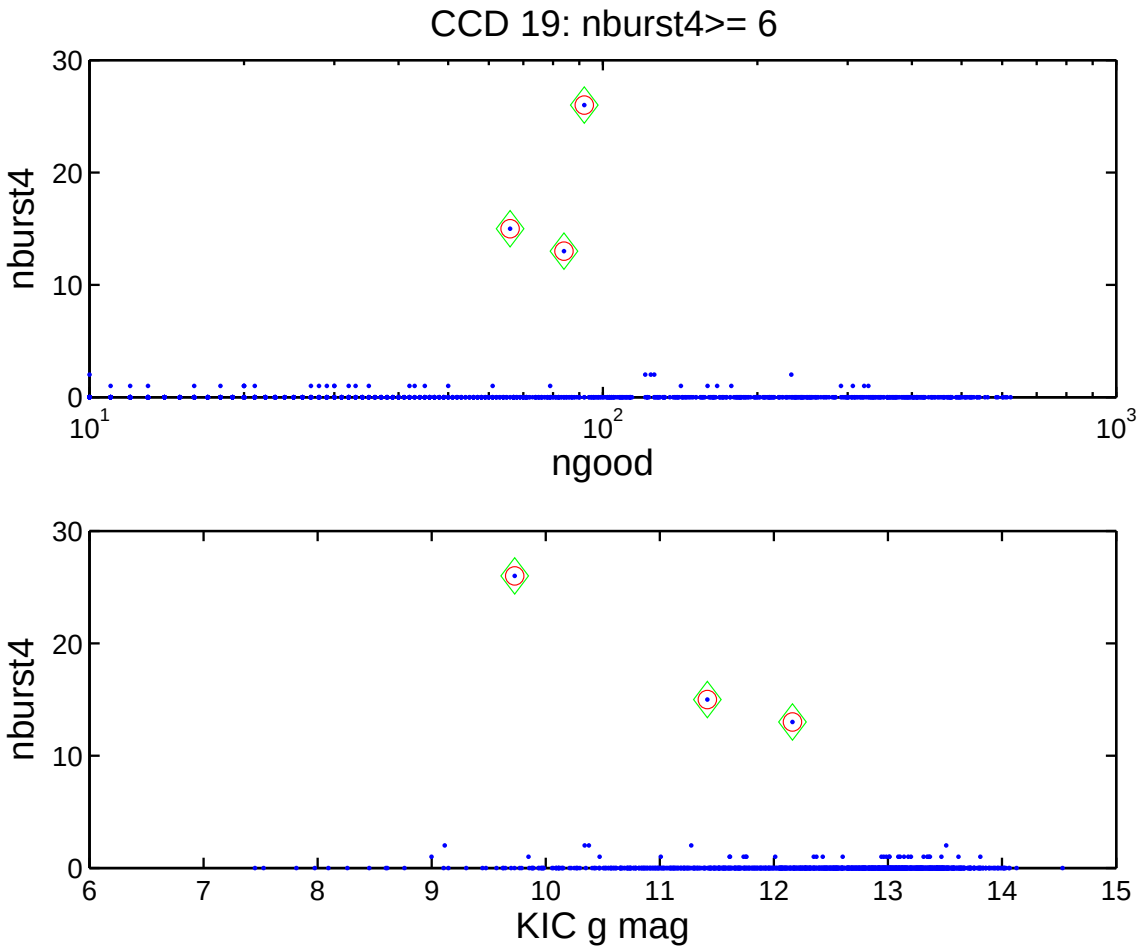

Figure 7.25.— Measurement nburst4 vs number of good points (upper panel), and KIC g mag (lower panel). *nburst*4 is defined as the number of points $\geq 3\sigma$ brighter than the median value. Symbols are the same as Figure 7.9.

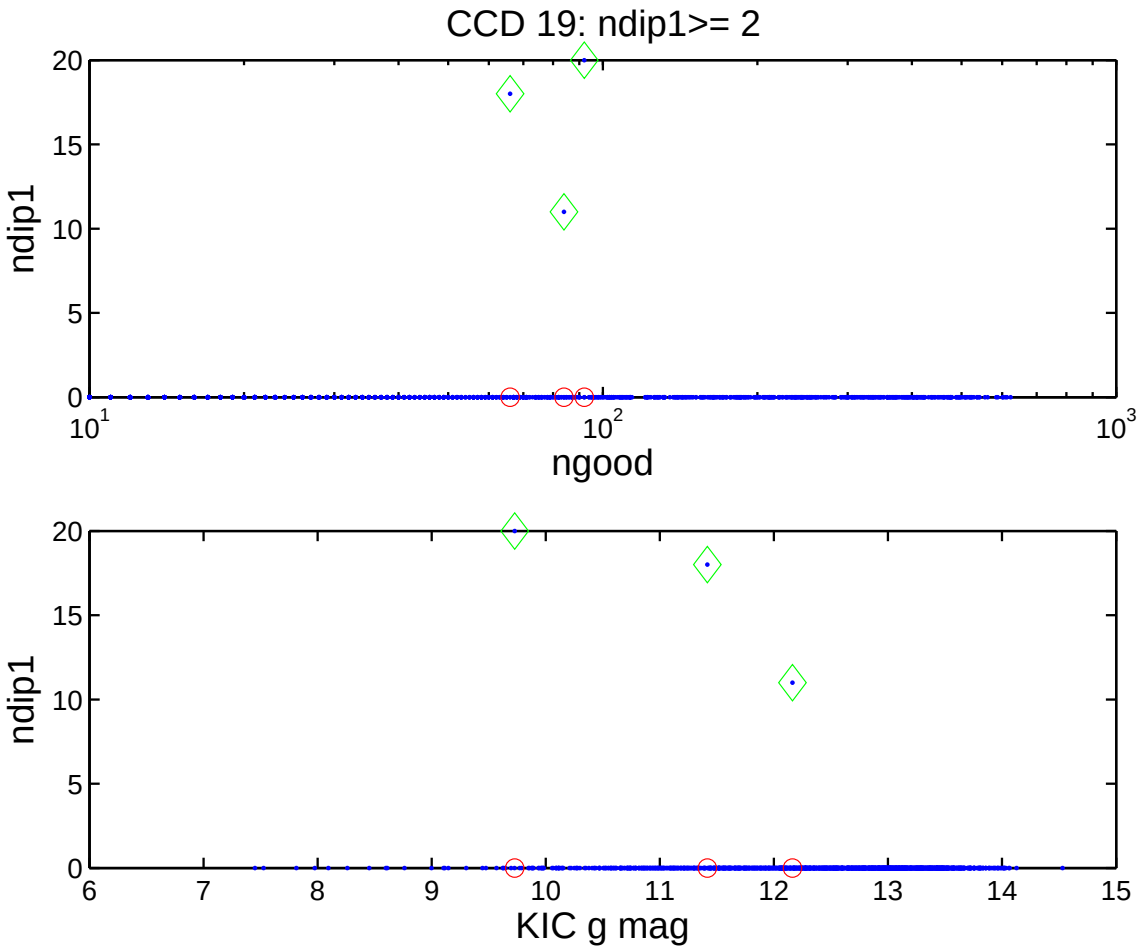

Figure 7.26.— Measurement ndip1 vs number of good points (upper panel), and KIC g mag (lower panel). *ndip*1 is defined as the number of points ≥ 0.8 mag fainter than the median value. Symbols are the same as Figure 7.9.

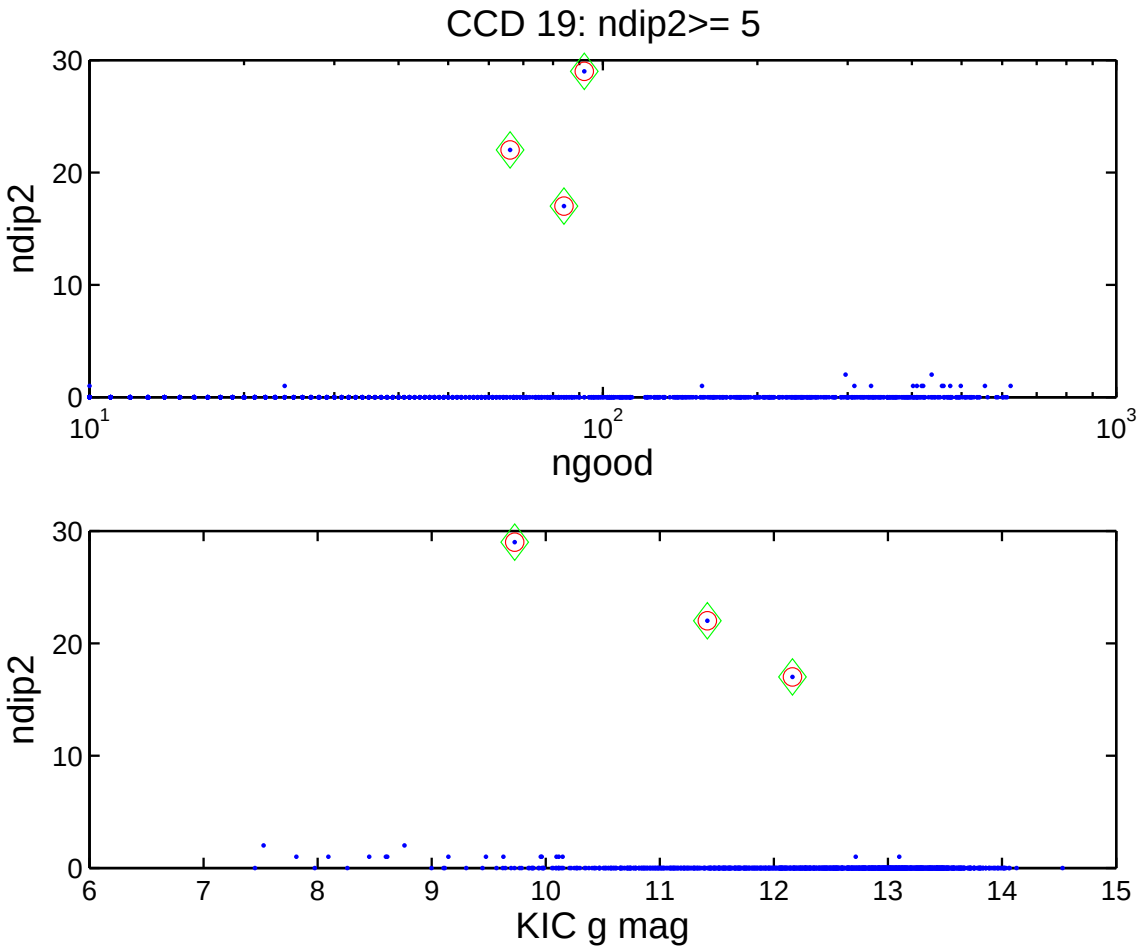

Figure 7.27.— Measurement ndip2 vs number of good points (upper panel), and KIC g mag (lower panel). *ndip*2 is defined as the number of points ≥ 0.5 mag fainter than the median value. Symbols are the same as Figure 7.9.

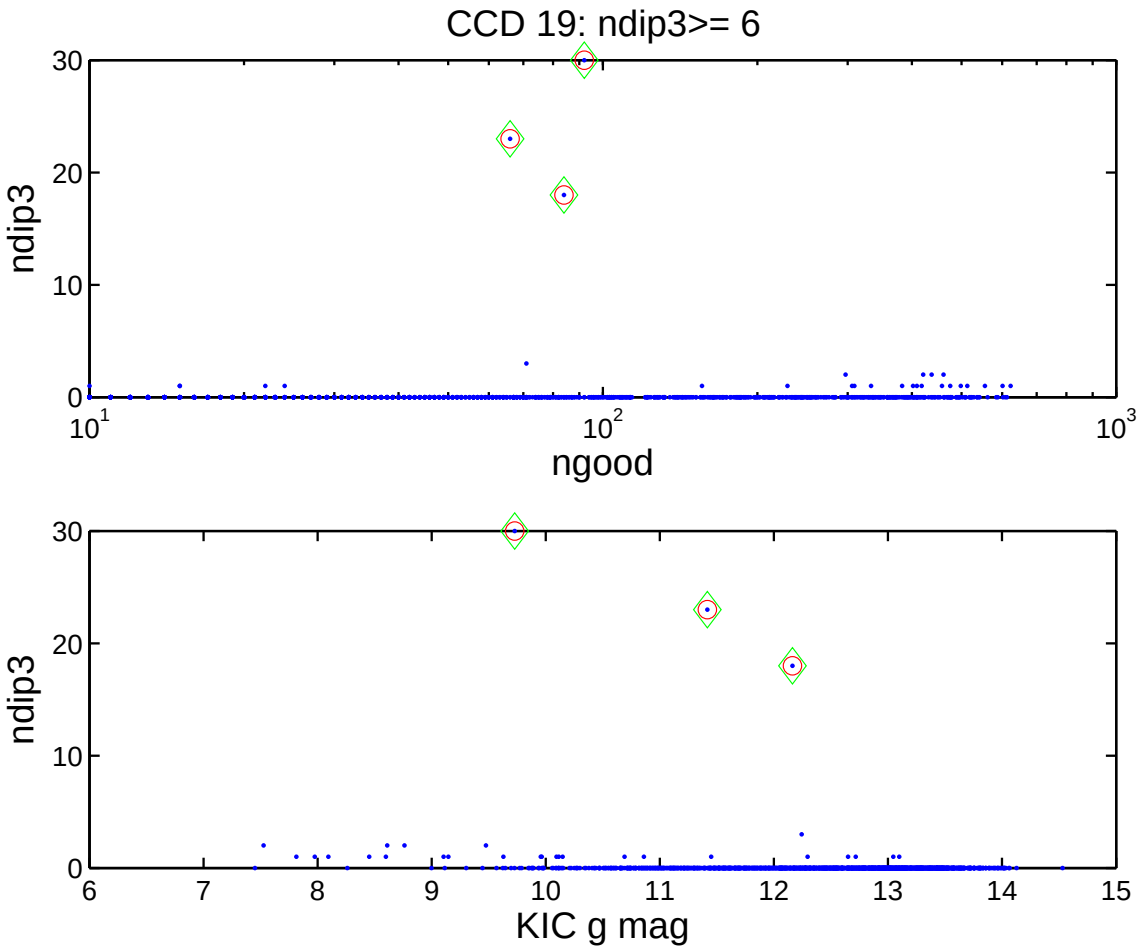

Figure 7.28.— Measurement ndip3 vs number of good points (upper panel), and KIC g mag (lower panel). *ndip*3 is defined as the number of points ≥ 0.4 mag fainter than the median value. Symbols are the same as Figure 7.9.

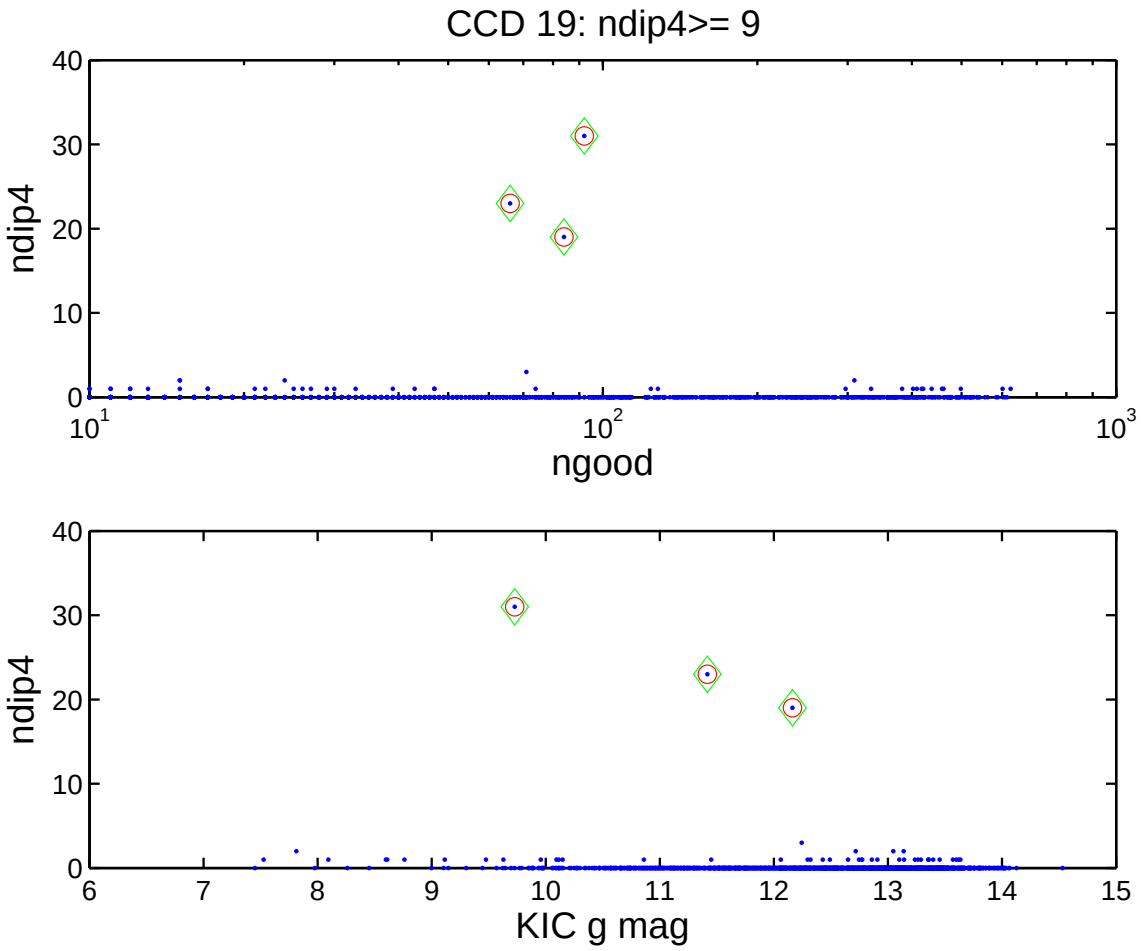

Figure 7.29.— Measurement ndip4 vs number of good points (upper panel), and KIC g mag (lower panel). *ndip*4 is defined as the number of points $\geq 3\sigma$ fainter than the median value. Symbols are the same as Figure 7.9.

7.2.4 Further removal of dubious variable candidates

Although we have identified and excluded most blended images and plate defects, there are still some light curves with dubious variations and thus included as variable candidates. Therefore, two more steps are used to further filter out dubious variables. First, if a star has neighbor or neighbors within 30 arcsec contributing $\geq 20\%$ of its flux, then we calculate the flux ratio of these neighbors to the flux of the star, $f_{neighbor}/f_{star}$. The blending of the star with its neighbors would resulted in higher light curve rms if not recognized. In the worst scenario, i.e., where half of the points are non-blended, and the other half are blended but not recognized, the light curve rms would be approximately $rms \sim sqrterror^2 + (f_{neighbor}/f_{star}/2)^2$. Therefore, if $f_{neighbor}/f_{star} > 0.2$ and $rms \leq sqrterror^2 + (f_{neighbor}/f_{star}/2)^2$, where the error is given by the average light curve rms of two neighbor stars with similar magnitudes and colors, the light curve rms is likely heavily contaminated or even dominated by blending, and we remove it from the variable candidate list. An example is shown in Figure 7.30.

Second, stars showing same outbursts or dips as its neighbor stars are excluded; An example is shown in Figure 7.31. In this case, the dips are from plate ac 36474 with emulsion defect, and resulted in wrong magnitude calibration.

7.3 Variable candidates

After carrying out the above cleaning steps, we are able to derive a catalog of DASCH variable candidates in the Kepler FOV, containing 92 objects. In this

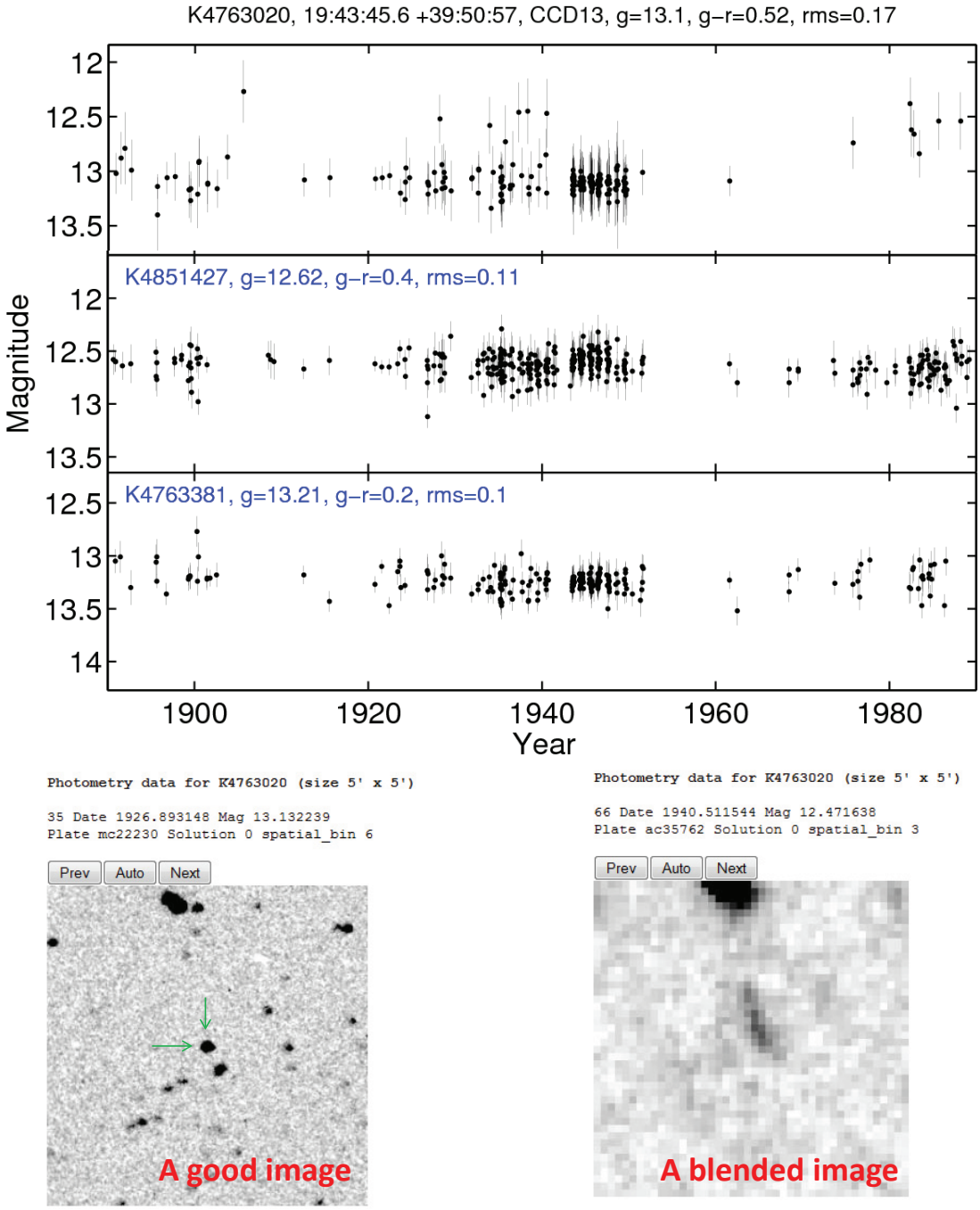

Figure 7.30.— An example light curve contaminated by blending, KIC 4763020. It has $g = 13.06$ mag, and it has a neighbor star K4762999 with $g = 14.15$ mag at a separation of 25″. Light curves of two neighbor stars are also shown for comparison. An example good plate image is shown at the lower-left corner, and an example blended image is shown at the lower-right corner.

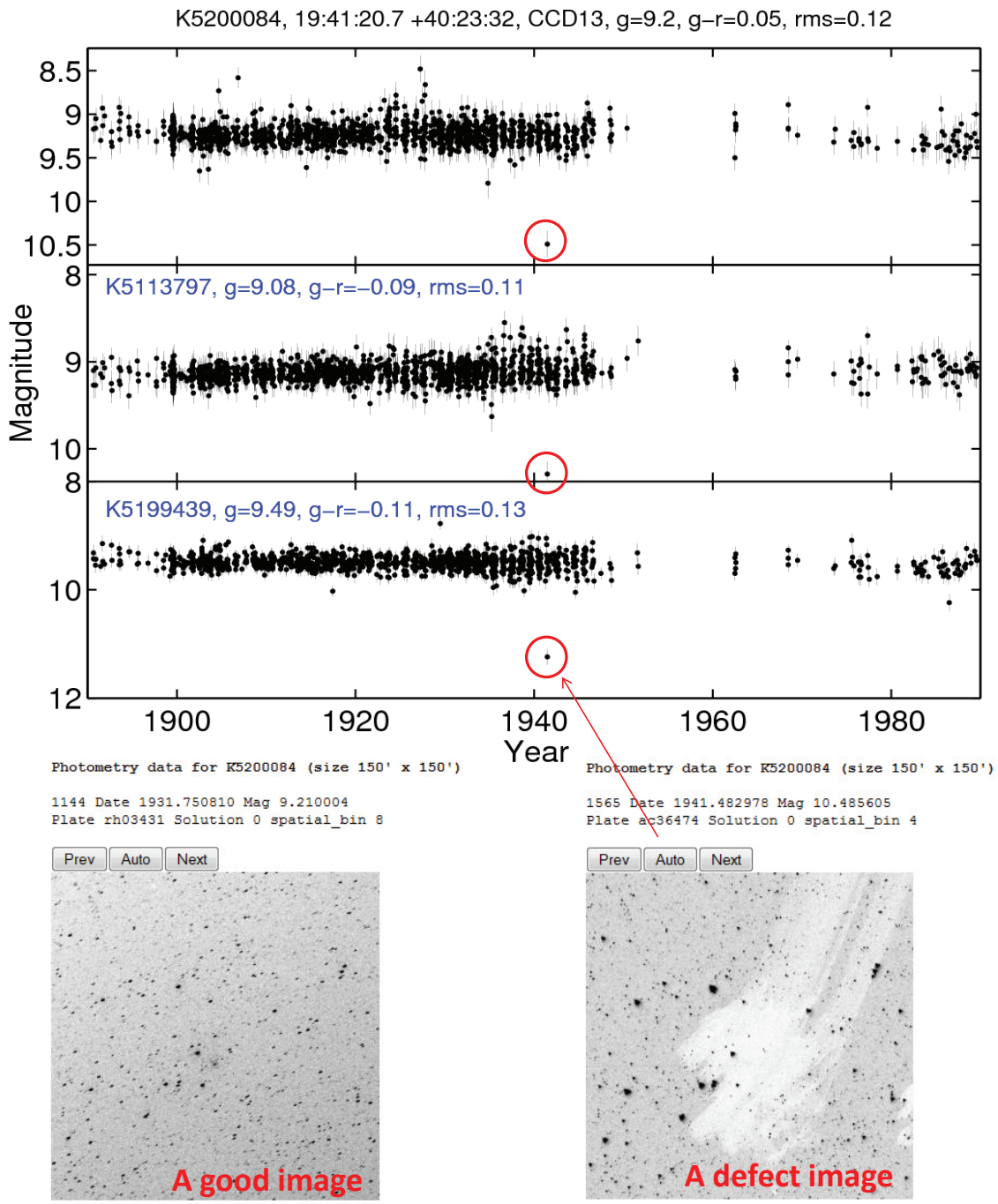

Figure 7.31.— An example light curve contaminated by emulsion defect, KIC 5200084. Light curves of two neighbor stars are shown for comparison, both also show the same dip in 1941, on plate ac 36474. An example good plate image is shown at the lower-left corner, and the defect image on plate ac 36474 is shown at the lower-right corner.

section, I describe the general properties of these candidates, discuss the selection efficiency by comparing with the ASAS variable catalog, and present a few example variables.

7.3.1 General properties and comparison with the ASAS variable catalog

The DASCH light curve rms and amplitude vs KIC g mag for these 92 DASCH variable candidates are shown in Figures 7.32-34. They are mostly bright stars (90 out of 92 with $g < 14$ mag, 77 out of 92 with $g < 13$ mag, and 55 out of 92 with $g < 12$ mag). As expected, most of them are mostly large rms or/and large amplitude variables. For example, there are 84 (91.3%), 88 (95.7%), and 90 (97.8%) variables with $range\_local > 0.5$, 0.4, and 0.3 mag, respectively ($range\_local$ is defined as the difference between the brightest and the faintest points, minus the sum of their errors). The distribution of their g mag, light curve rms and amplitude are also shown in Figures 7.32-34. Note that these 92 objects are the preliminary variable candidates, and further examination of their light curves and plate images on a one-by-one basis are still needed for verification.

The ASAS variable catalog contains 947 objects in the Kepler field (Pigulski et al. 2009). Most of them are relatively faint, and only 322 of them have more than 10 good points in DASCH. We obtained 50 of them as variable candidates. Their DASCH light curve rms and amplitude vs ASAS amplitude are shown in Figures 7.35-37.

We recovered most ASAS variables with large light curve rms, as shown in the

lower-right panel of Figure 7.35. All the 28 ASAS variables with rms$>$ 0.3 mag, are found to be variables in DASCH light curves; 92%, i.e. 34 out of 37, ASAS variables with rms $>$ 0.25 mag, are found to be variables in DASCH light curves.

Most ASAS variables we missed are small amplitude variables (ASAS V amplitude $\leq$ 0.5 mag), limited by our photometry uncertainty (which is $\sim 0.1 - 0.13$ mag). The numbers and percentages of different types of ASAS variables we obtained as DASCH variables are listed in Table 7.1. We recovered all the Miras in the ASAS catalog, and 80% of RR Lyr stars and 58% of long period variables (APER) with $\Delta V \geq 0.5$ mag. Our recovery rate of variables with a dominating periodicity but also other variations (QPER), Algol-type eclipsing binaries (EA), β Lyr-type and W UMa-type (EB/EW) are relatively lower, which is 33%, 33% and 9% for these types of ASAS variables with $\Delta V \geq 0.5$ mag, respectively. The 10 out of 11 EB/EW eclipsing binaries with ASAS $\Delta V \geq 0.5$ mag we missed all have relatively small amplitude ($\Delta V \leq 0.75$ mag), and thus do not show significant variations in DASCH light curves (light curve rms $<$ 0.25 mag).

The ASAS variables with large amplitude in V band we missed are relatively faint stars, which have relatively poor coverage in DASCH. For example, among the 14 ASAS variables with V amplitude $>$ 0.8 mag we missed, 10 of them are fainter than $g = 12.5$ mag, and 6 of them are fainter than $g = 13$ mag; among the 46 ASAS variables with V amplitude $>$ 0.5 mag we missed, 24 of them are fainter than $g = 12.5$ mag, and 16 of them are fainter than $g = 13$ mag.

Table 7.1: Compare DASCH variables with the ASAS variable catalog.

Variable Type	APER[a]	QPER[b]	MIRA	RRLyr	EA[c]	EB/EW[d]	HADS[e]	CEP[f]	Total
DASCH&ASAS	14	14	9	4	6	2	1	0	50
ASAS ΔV >0.5									
DASCH	14	10	9	4	2	1		0	40
ASAS	24	30	9	5	6	11		1	86
ratio	58%	33%	100%	80%	33%	9%		0%	47%
ASAS ΔV >0.8									
DASCH	9	5	9	3	0				26
ASAS	13	13	9	4	1				40
ratio	69%	38%	100%	75%	0%				65%
ASAS ΔV >1									
DASCH	8	2	9	2					21
ASAS	9	3	9	2					23
ratio	89%	67%	100%	100%					91%
ASAS ΔV >1.5									
DASCH	4	1	9						14
ASAS	4	1	9						14
ratio	100%	100%	100%						100%

[a] ASAS variables with no well-pronounced periodicity or the period is longer than the analyzed data (17 months; Pigulski et al. 2009).

[b] ASAS variables with dominated periodicity but also show other variations.

[c] ASAS Algol-type eclipsing binaries.

[d] ASAS β Lyr-type or W UMa-type eclipsing binaries.

[e] ASAS high-amplitude δ Sct stars.

[f] ASAS Cepheids.

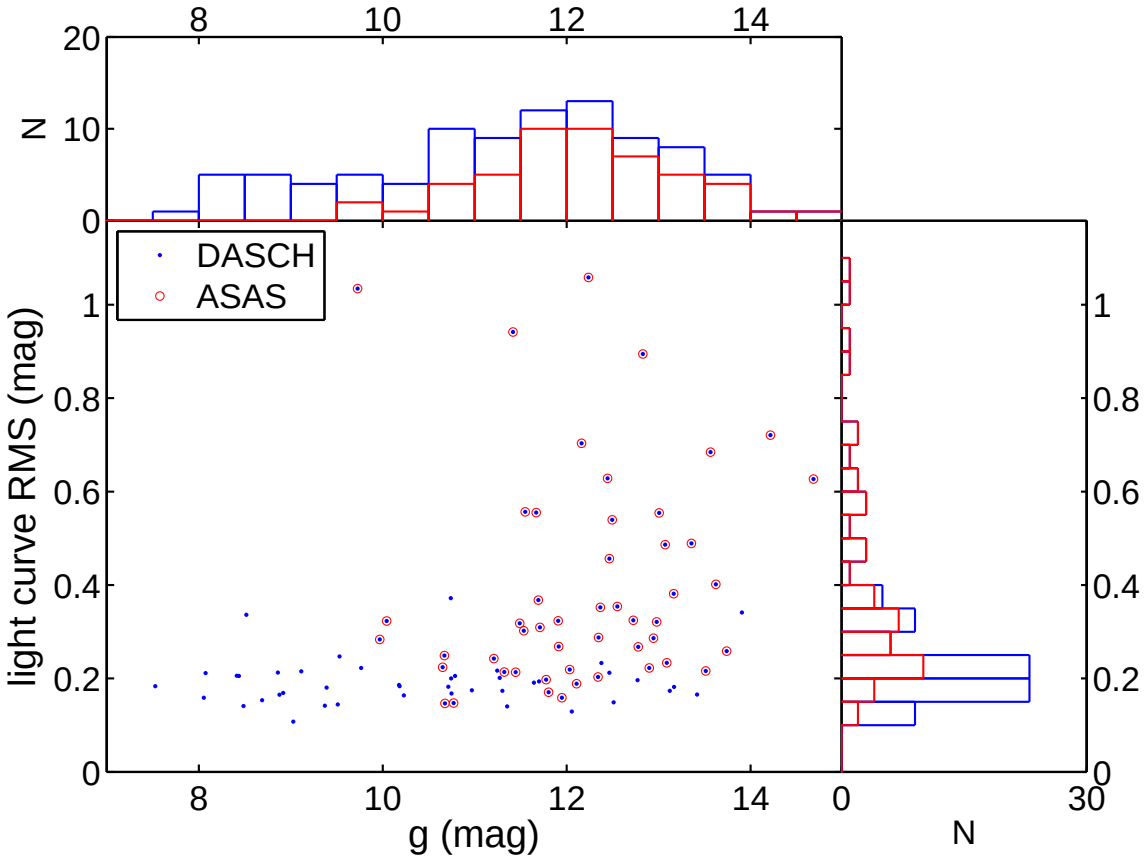

Figure 7.32.— DASCH light curve rms vs KIC g mag for 92 DASCH variable candidates. Each blue dot represents a DASCH variable. Objects overlap with the ASAS variable catalog are marked by red open circles. The histograms in g mag and light curve rms are also shown, with blue for the whole sample, and red for these also in ASAS.

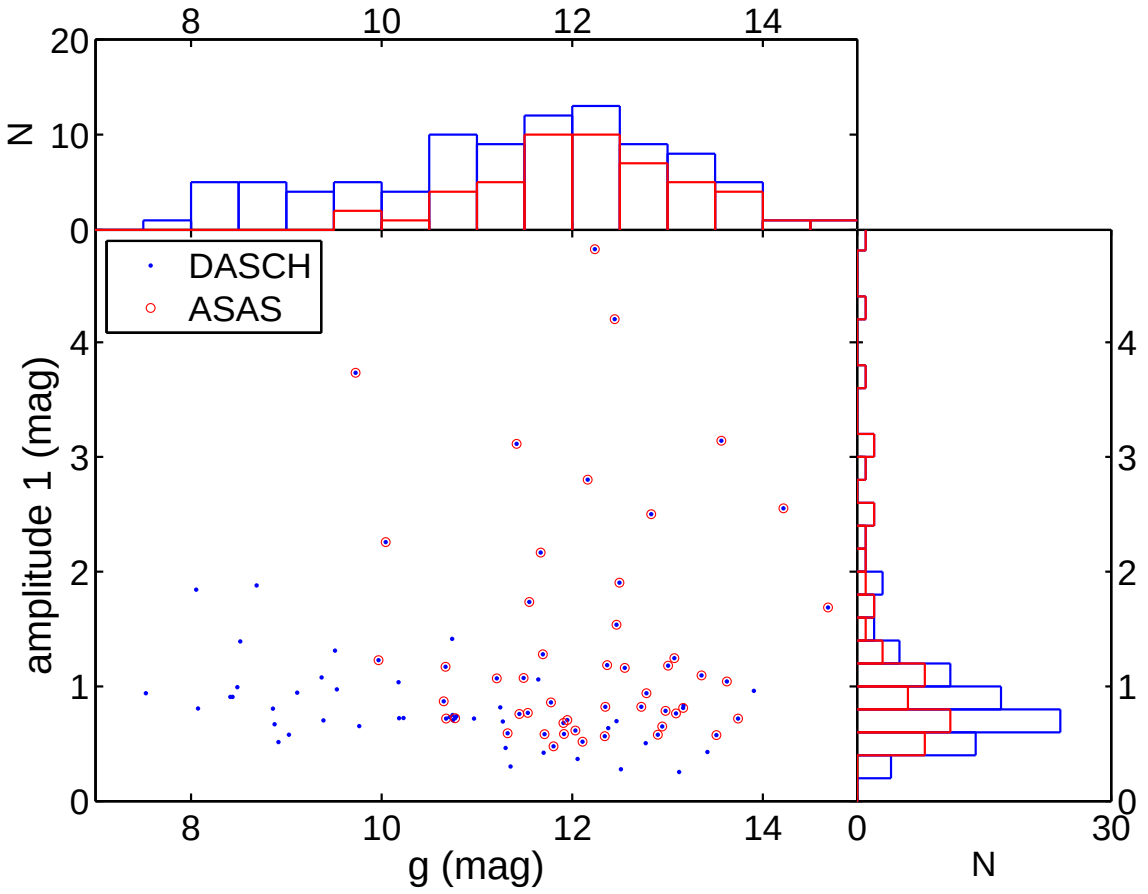

Figure 7.33.— DASCH light curve amplitude range_local vs KIC g mag for 92 DASCH variable candidates. *range_local* is defined as the difference between the brightest and the faintest points, minus the sum of their errors. Symbols are the same as Figure 7.32.

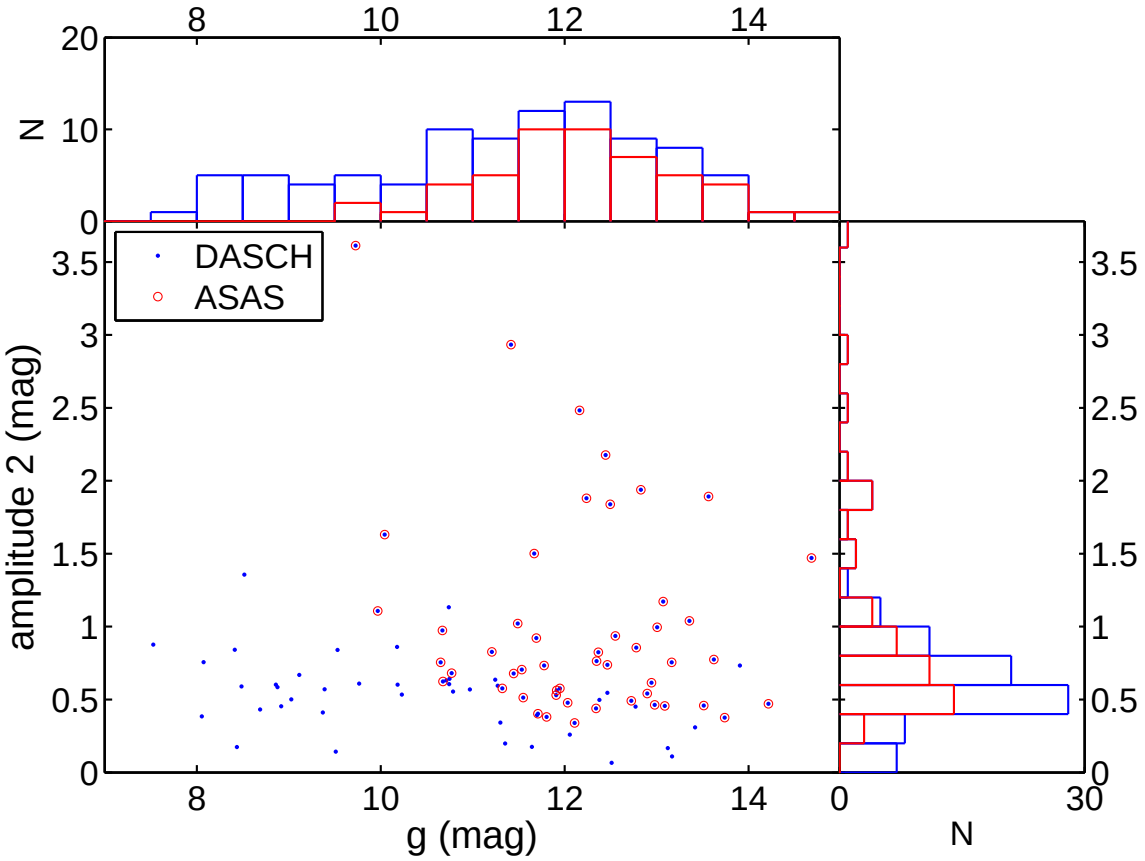

Figure 7.34.— DASCH light curve amplitude range_local2 vs KIC g mag for 92 DASCH variable candidates. *range_local2* is defined as the difference between the second brightest and the second faintest points, minus the sum of their errors. Symbols are the same as Figure 7.32.

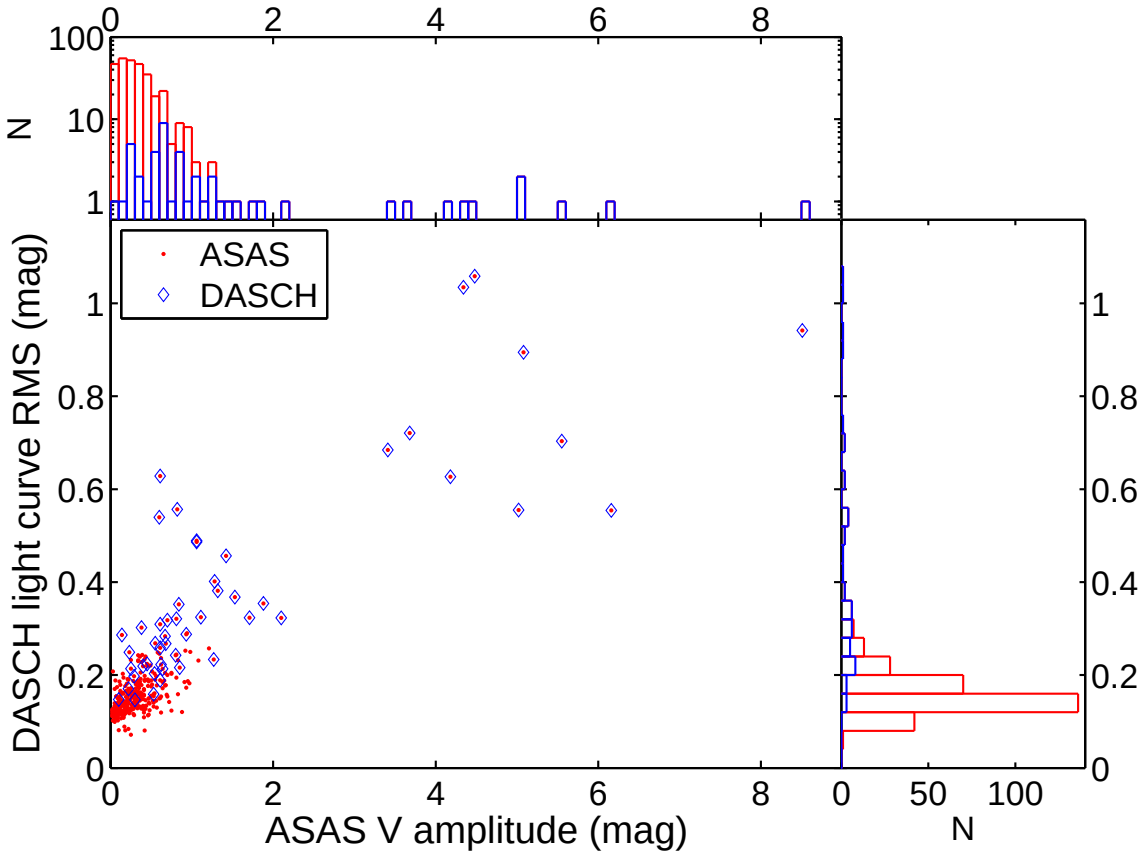

Figure 7.35.— DASCH light curve rms vs ASAS V band amplitude for 322 ASAS variables with ≥ 10 good points in DASCH. Each red dot represents a ASAS variable. Objects identified as DASCH variables are marked by blue diamonds. The histograms in both axis are also shown, with red for the whole sample, and red for these which are also DASCH variables.

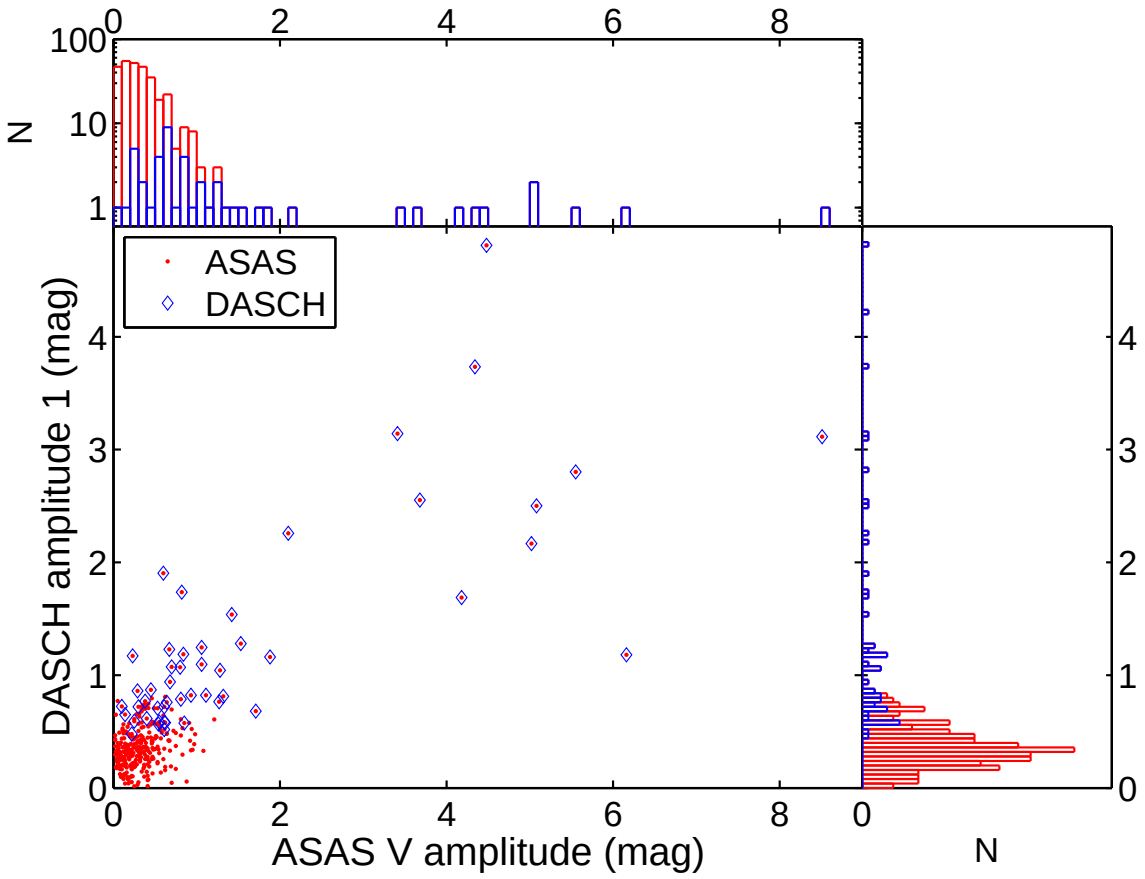

Figure 7.36.— DASCH light curve amplitude range_local vs ASAS V band amplitude for 322 ASAS variables with ≥ 10 good points in DASCH. *range_local* is defined as the difference between the brightest and the faintest points, minus the sum of their errors. Symbols are the same as Figure 7.35.

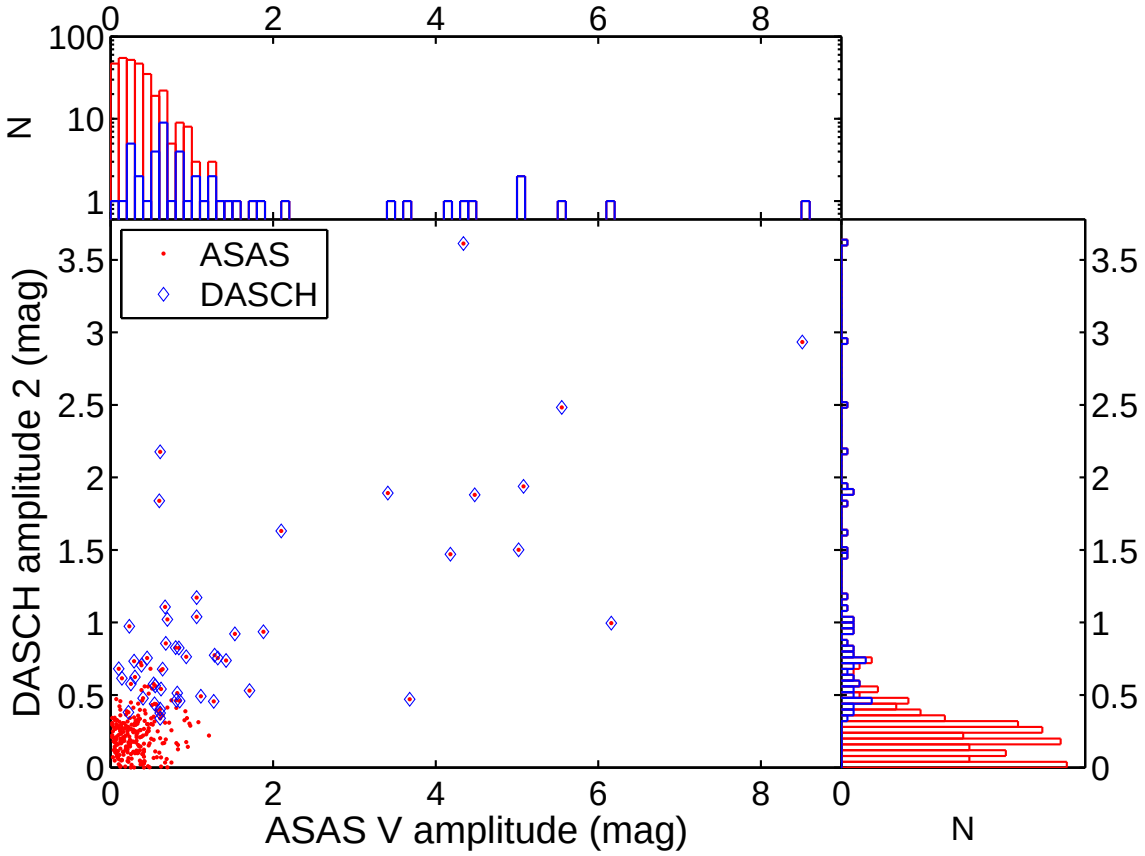

Figure 7.37.— DASCH light curve amplitude range_local2 vs ASAS V band amplitude for 322 ASAS variables with ≥ 10 good points in DASCH. *range_local2* is defined as the difference between the second brightest and the second faintest points, minus the sum of their errors. Symbols are the same as Figure 7.35.

7.3.2 A few example variables

Here I present the DASCH light curves of 6 example variables, as shown in Figures 7.38-43. The light curves of two neighbor stars for each variable are also shown for comparison.

The first three examples are also ASAS variable(Pigulski et al. 2009). The first example, K10003658, is a MIRA variable, as shown in Figure 7.38. It has $\Delta V = 4.5$ mag in ASAS. The second example, K11125706, as shown in Figure 7.39, is classified as RR Lyrae type ab in ASAS with $\Delta V = 0.55$ mag. The third example, K2708156, is an eclipse binary, as shown in Figure 7.40. It is also an ASAS eclipsing binary with $P = 1.8913$ days (Pigulski et al. 2009). The forth and fifth examples are eclipsing binaries not recognized in ASAS variable catalog, i.e. K9101279 (V1580 Cyg), as shown in Figure 7.41, and K9207508 (V512 Lyr), as shown in Figure 7.42.

The last example, K4644922, showed a 2.5 mag dimming event from the 1890s to the 1960s, as shown in Figure 7.43. It is classified as a G dwarf in KIC catalog, however, our FAST spectrum suggests it is a G type giant. It is classified as 'QPER' in ASAS with $P = 128.8$ days ('QPER' means it has a dominating periodicity, but also show other changes superimposed on the variability on a longer time scale; Pigulski et al. 2009). Its Kepler light curve shows modulation with $P \sim 129$ days similar to ASAS. It is an extremely bright IR source, with IRAS flux of 2 Jy, 1.6 Jy, and 0.5 Jy at 12, 25, and 60 μm, respectively. It is also an AKARI/IRC source, with flux of 1.7 Jy and 1.4 Jy at 9 and 18 μm, respectively, Its 20 μm to optical flux ratio is ~ 250 times larger compared with PHI 2 ORI, a G8III IR standard star. It is probably a post-AGB star, and the 60 yr dip is likely a spectacular dust event.

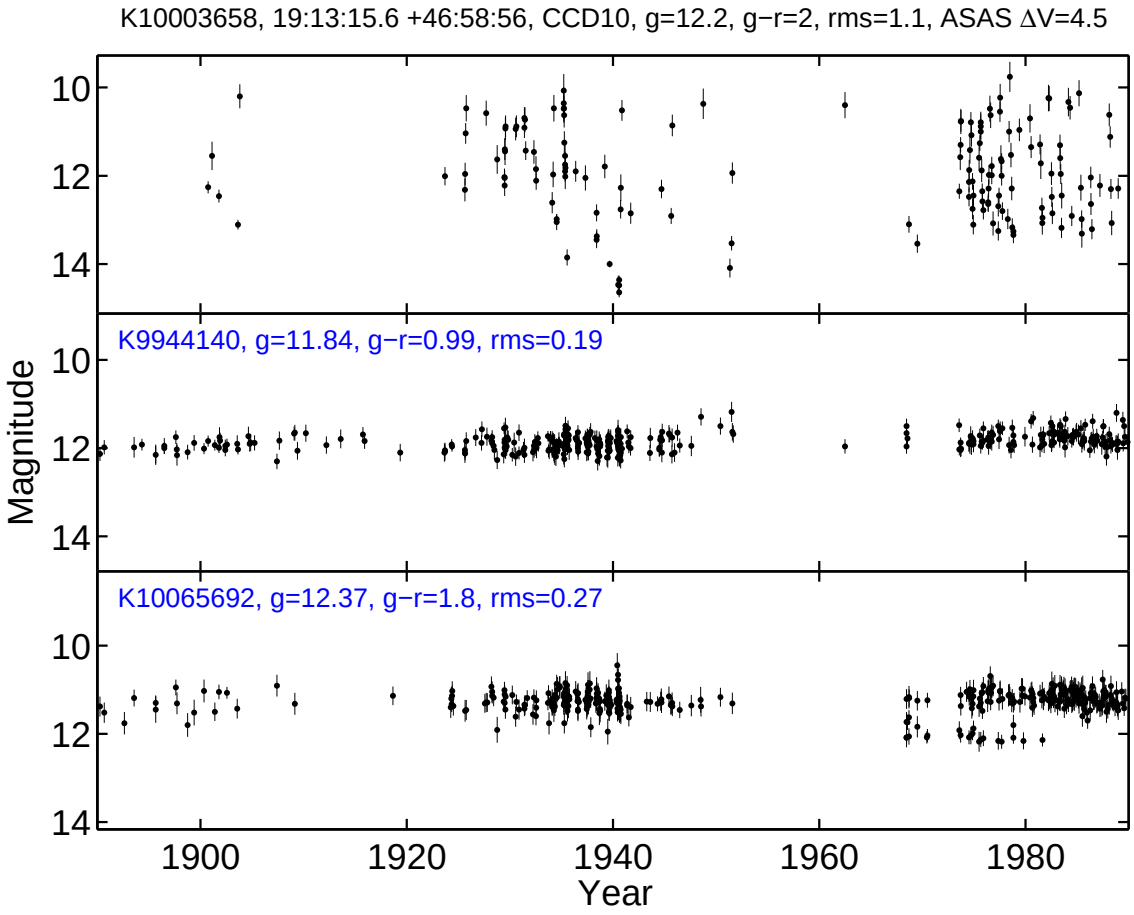

Figure 7.38.— DASCH light curves of K10003658 (top panel), a Mira variable star, and its two neighbors.

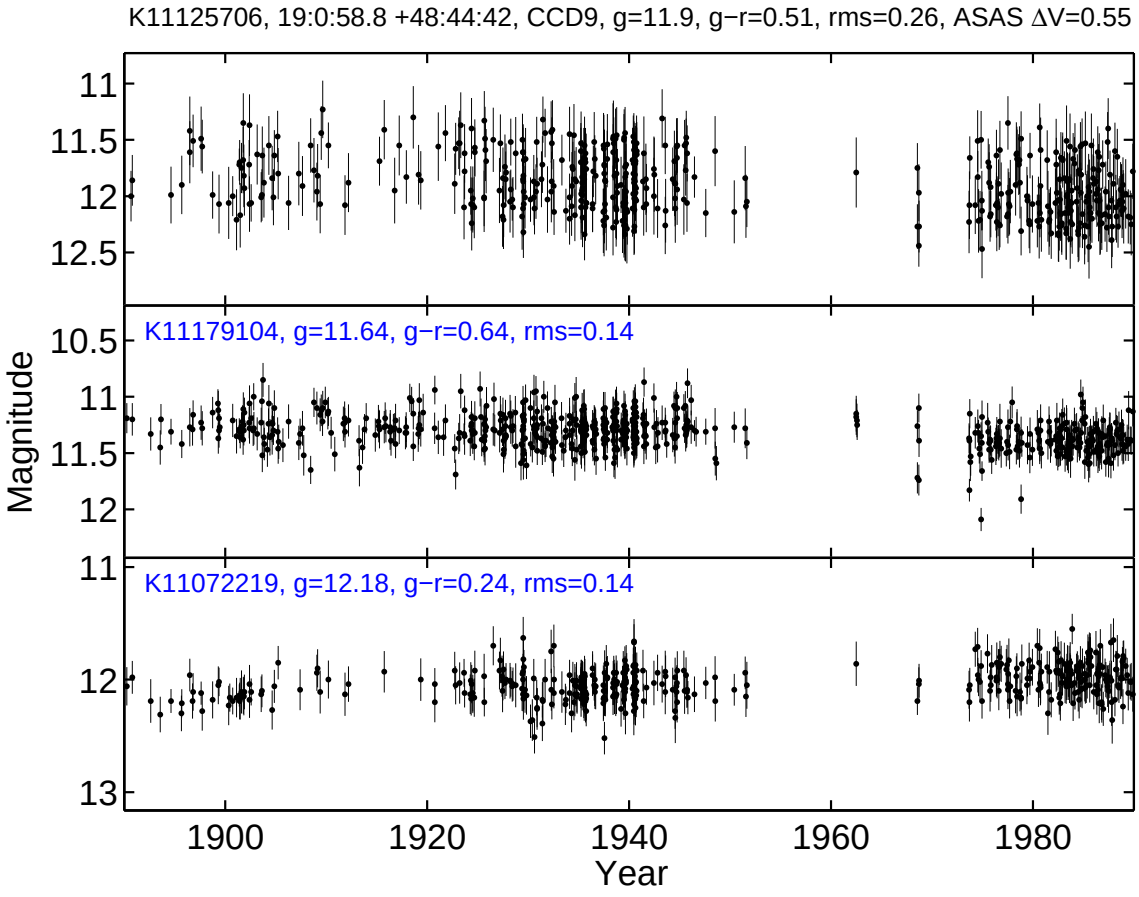

Figure 7.39.— DASCH light curves of K11125706 (top panel), a RR Lyr variable star, and its two neighbors.

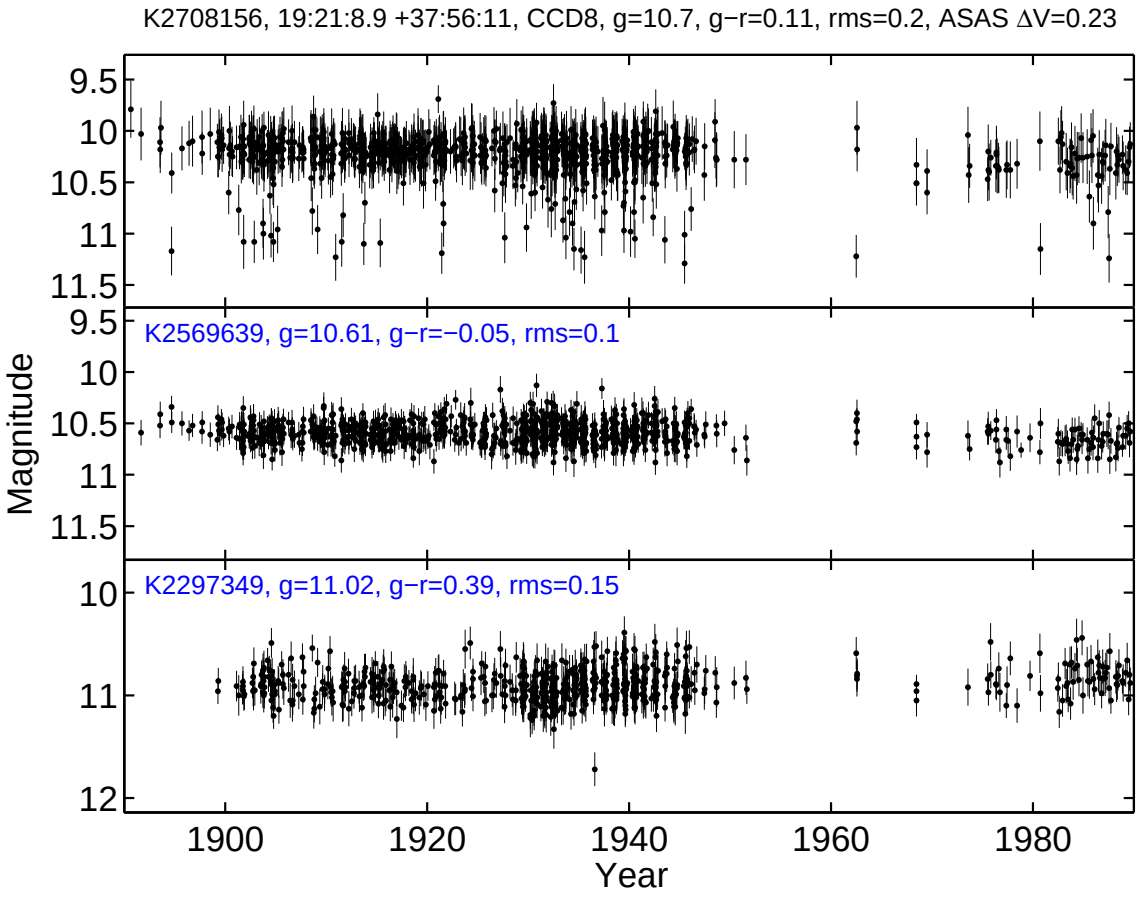

Figure 7.40.— DASCH light curves of K2708156 (top panel), an eclipsing binary, and its two neighbors.

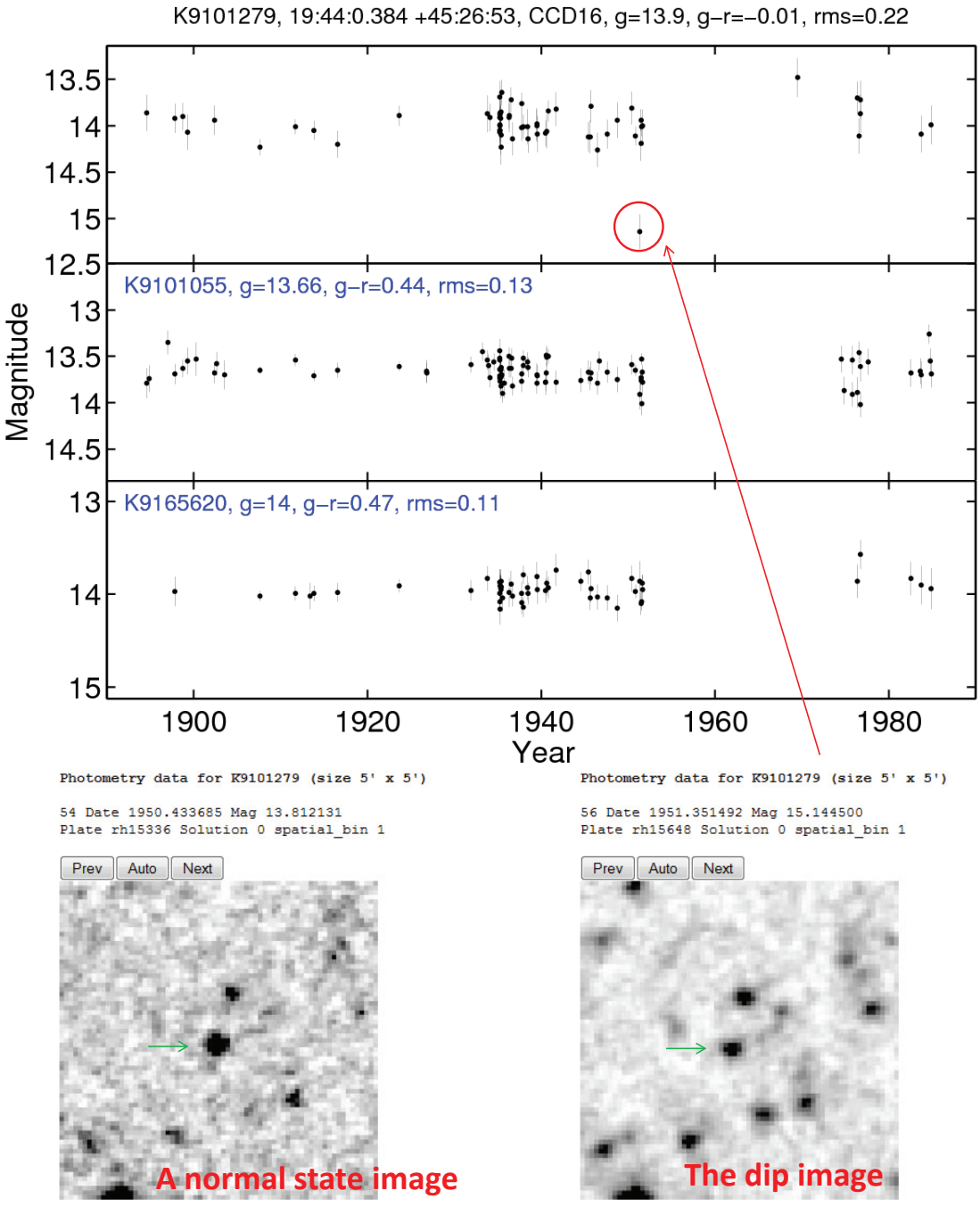

Figure 7.41.— DASCH light curves of K9101279 (top panel), an eclipsing binary not included in the ASAS variable catalog, and its two neighbors.

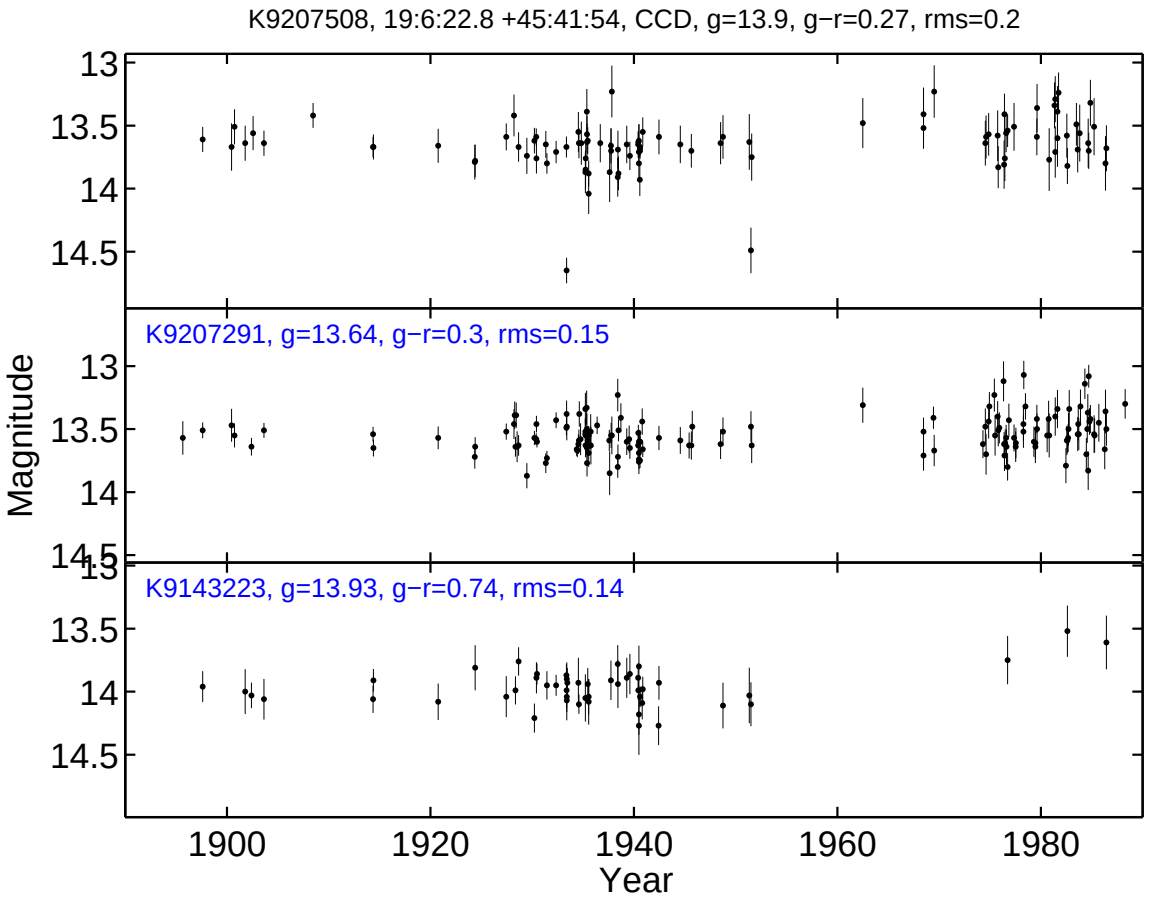

Figure 7.42.— DASCH light curves of K9207508 (top panel), an eclipsing binary not included in the ASAS variable catalog, and its two neighbors.

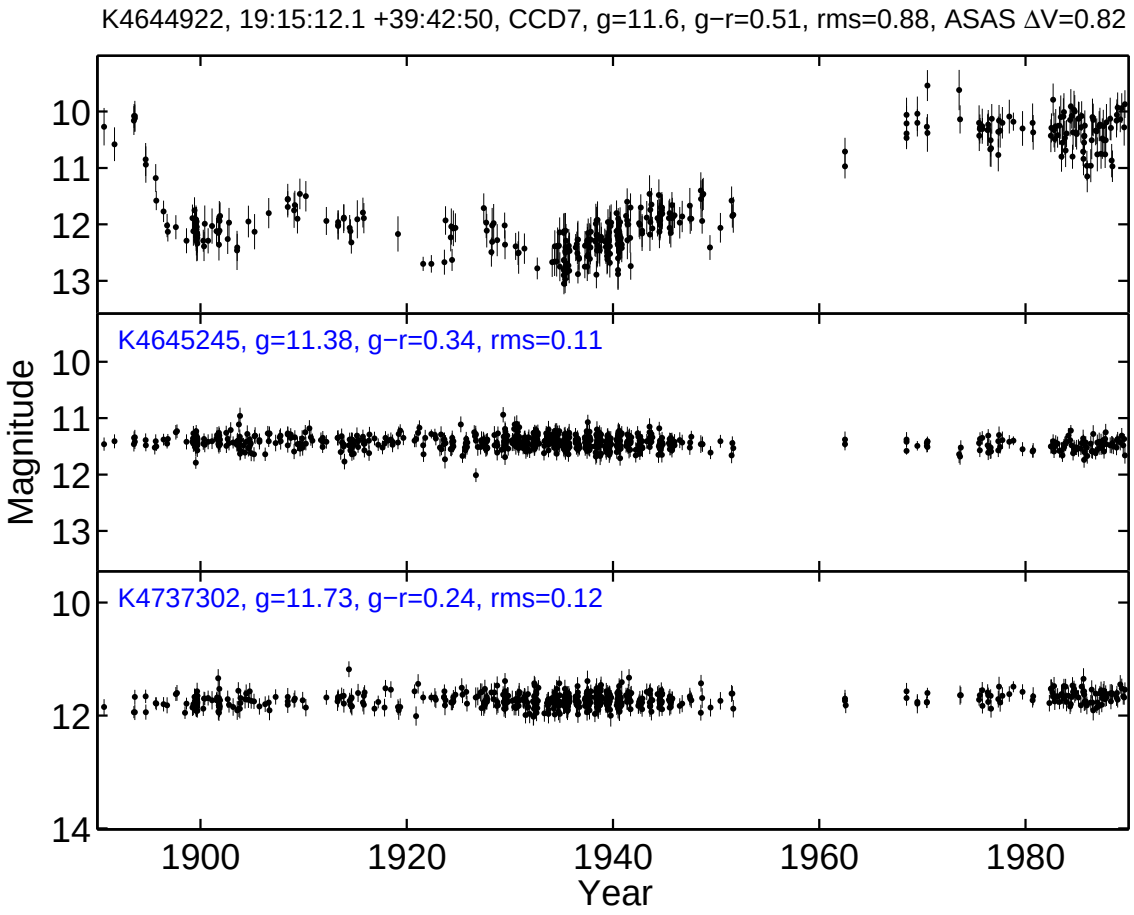

Figure 7.43.— DASCH light curves of K4644922 (top panel), a peculiar long-term variable, and its two neighbors.

7.4 DASCH-Kepler Variable Catalog

The layout of the catalog of variable candidates is presented in Table 7.2, with the first 10 entries of the 92 sources. In the table, I provide the KIC id, RA, Dec, DASCH B mag (median value in DASCH light curve), DASCH light curve RMS, and DASCH light curve amplitude (ΔB). I also provide the ASAS ID, type, period and ΔV for the variables included in the ASAS variable catalog (Pigulski et al. 2009). They are ranked by increasing RA order. Note that although all of these 92 objects show excess variability in DASCH light curves, some of them might not be genuine variables. Further examination of their light curves and plate images on a one-by-one basis and follow-up observations are still needed for verification.

Table 7.2: DASCH catalog of variables in the Kepler FOV.

KIC	RA (°)	Dec (°)	B (mag)	RMS (mag)	ΔB (mag)	ASAS ID	Type	Period (days)	ΔV (mag)
K7797807	280.03397	43.5762	9.74	0.18	0.7	NA	NA	NA	NA
K7869590	281.7762	43.6762	11.6	0.17	0.48	184706+4340.6	QPER	19.91	0.22
K9933239	281.8351	46.8987	9.42	0.14	1.31	NA	NA	NA	NA
K7584285	282.05462	43.245	12.66	0.4	1.04	184813+4314.7	APER	NA	1.28
K8077489	282.67998	43.9574	7.92	0.21	0.91	NA	NA	NA	NA
K6020264	282.7415	41.3993	12.31	0.19	0.52	185058+4124.0	APER	NA	0.61
K11229003	282.87552	48.9119	12.46	0.55	1.18	185130+4854.7	MIRA	396	6.16
K7662831	283.16208	43.3878	12.41	0.23	0.64	NA	NA	NA	NA
K7259917	283.25914	42.8456	12.07	0.21	0.7	NA	NA	NA	NA
K9815101	283.42019	46.686	12.19	0.29	0.82	185341+4641.2	QPER	148.3	0.93

7.5 Summary

In this chapter, I described my variable search algorithms, and presented a preliminary variable candidate catalog including 92 variable candidates. I compared the catalog with the ASAS variable catalog, and 50 variables are included in both catalogs. I showed that most bright ($g < 13$ mag) and large amplitude ($\Delta V > 0.5$ mag) ASAS variables are recovered by DASCH, with three example variables shown in Figures 7.38-39. ASAS variables not found by DASCH are mostly small amplitude variables (with light curve rms$<$ 0.25 mag). Some variables not included in ASAS variable catalog are also found, with two example eclipsing binaries shown in Figures 7.41-42. To illustrate the unique advantage of DASCH which covers a century timescale, a peculiar long-term variable with a 2.5 mag dip which lasted $\sim$ 60 years is shown in Figure 7.43. This object might be a post-AGB star with a spectacular dust event, and study of this object is in progress.

Chapter 8

Conclusions

This thesis is the culmination of six chapters (each chapter alone is a first-authored scientific paper) that includes two parts: (i) development of DASCH photometric pipeline and variable search, and (ii) studies of individual peculiar long-term variables.

The variability of stars over long timescales from years to decades are poorly explored due to the lack of data. With the 100-yr data of DASCH, it is now possible to do it in a systematic way. I have found many peculiar long-term variables from DASCH. After finding them, I have carried out follow-up spectroscopic observations, which provide important information on these stars, including spectral and luminosity classifications, radial velocities and orbits, and stellar parameters such as temperatures, surface gravity and metallicity. Using DASCH data and follow-up spectra, I was able to study the long-term and extreme variability of stars, which provides important information on stellar evolution, magnetic cycles, accretion physics, and dust processes.

8.1 Photometric Development and Variable Search

In Chapter 2, I described my work on the DASCH photometry pipeline. It includes annular bin photometry, plate color-term fitting, identifying blended images, filtering out defects by image profiles and large astrometric deviations, as well as improved local calibrations by using neighbor stars with similar magnitudes and colors. All of the above developments are designed to serve the scientific purpose of finding real variables on DASCH plates. We report that our photometry accuracy is about $0.1 - 0.13$ mag. We also define statistical measurements of light curves, which will be used for selecting variable stars.

In Chapter 6, I presented 100 year DASCH light curves of Kepler planet-candidate host stars. No variation is found at 3σ level for these host stars, which is good for the habitability of these planets.

In Chapter 7, I presented DASCH variable search in the Kepler field of view (FOV). I describe the variable search algorithms, the preliminary results of variable candidates, and presented several example variables. Comparing with the ASAS variable catalog, most of large amplitude variable stars with at least 10 good measurements in DASCH, i.e. 47% of the variables with $\Delta m \geq 0.5$ mag, and 92% of the variables with rms > 0.25 mag, are recovered by DASCH. I conclude this chapter with a preliminary version of the DASCH-Kepler Variables Catalog, with representative entries and a brief discussion of what the catalog contains and the verification work still to be done, as well as spectroscopic followup.

8.2 Individual Peculiar Long-term Variable Stars

In Chapters 3-5, I studied individual exciting long-term variables discovered in DASCH. The most interesting one is a peculiar 10-yr nova, as in Chapter 5. With $P = 119$ days, it is interestingly located in the gap region between classic novae and symbiotic novae. The most probable explanation of the outburst is Hydrogen shell-burning on the WD without significant mass loss, which suggests a promising new channel for Type Ia Supernovae (SNe). I have found peculiar long-term K giant variables with $1 - 2$ mag variations over decades, as presented in Chapter 3. It contains a subgroup of RS CVn binaries with strong magnetic activity, and another subgroup of single stars. In both cases, the variation amplitudes and timescales are abnormal, and may be related to either ultra strong star spots, or novel dust formation processes. I have also discovered a 5-yr duration dust accretion event in KU Cyg, which is probably related to its accretion disk.

8.3 Additional Variables and Future Work

There are several other very interesting variables. One is a G dwarf + white dwarf (WD) binary which showed ~ 14 yr activity cycles. Its spectra show strong Ca H&K emissions, indicating strong chromospheric activity; It is also a bright soft X-ray and UV source, probably from the WD. We suggest that the G dwarf is barely filling its Roche lobe but when it undergoes enhanced flaring activity due to its convective stirring by its WD companion, the WD is able to accrete at moderately high rate (10^{-9} $M_{\odot}$/yr) to produce the sustained brightenings that may be quasi-periodic on

a $\sim$ 14 yr "solar cycle".

Another one is a M giant with $\sim$ 3 yr eclipses, showing $\sim$ 4 mag dips in both optical bands and NIR JHK. It is probably an extremely rare Epsilon Aurigae-like system, where the dips were caused by the eclipse of a huge disk around its companion.

I have also found a group of large amplitude ($\sim$ 1 mag) Be variables which might be Be X-ray binaries (neutron star + Be star binaries). Follow-up observations are in progress and I expect to finish the papers on them soon.

References

Alcock, C., et al. 2000, ApJ, 542, 281

—. 2001, ApJ, 554, 298

Allen, D. A. 1980, MNRAS, 192, 521

Basri, G., et al. 2010, ApJ, 713, L155

—. 2011, AJ, 141, 20

Bedding, T. R. 2000, in The Third MONS Workshop: Science Preparation and Target Selection, ed. T. Teixeira & T. Bedding, 97

Bedding, T. R., Zijlstra, A. A., Jones, A., Marang, F., Matsuura, M., Retter, A., Whitelock, P. A., & Yamamura, I. 2002, MNRAS, 337, 79

Bedin, L. R., Piotto, G., Zoccali, M., Stetson, P. B., Saviane, I., Cassisi, S., & Bono, G. 2000, A&A, 363, 159

Belczyński, K., Mikołajewska, J., Munari, U., Ivison, R. J., & Friedjung, M. 2000, A&AS, 146, 407

Bensby, T., Feltzing, S., & Lundström, I. 2004, A&A, 421, 969

Bernstein, R., Shectman, S. A., Gunnels, S. M., Mochnacki, S., & Athey, A. E. 2003, in Society of Photo-Optical Instrumentation Engineers (SPIE) Conference Series, Vol. 4841, Society of Photo-Optical Instrumentation Engineers (SPIE) Conference Series, ed. M. Iye & A. F. M. Moorwood, 1694–1704

Bertelli, G., Girardi, L., Marigo, P., & Nasi, E. 2008, A&A, 484, 815

Bertin, E. 2006, in Astronomical Society of the Pacific Conference Series, Vol. 351, Astronomical Data Analysis Software and Systems XV, ed. C. Gabriel, C. Arviset, D. Ponz, & S. Enrique, 112

Bertin, E., & Arnouts, S. 1996, A&AS, 117, 393

Borucki, W. J., et al. 2010, Science, 327, 977

—. 2011, ApJ, 736, 19

Brahe, T. 1573, De nova stella (On the new star), ed.

Brown, T. M., Latham, D. W., Everett, M. E., & Esquerdo, G. A. 2011, AJ, 142, 112

Carollo, D., et al. 2010, ApJ, 712, 692

Ciesla, F. J. 2007, Science, 318, 613

Cincunegui, C., Díaz, R. F., & Mauas, P. J. D. 2007, A&A, 469, 309

Clayton, G. C. 1996, PASP, 108, 225

Cleveland, W. S. a. 1981, Am. Stat., 35, 54

Covey, K. R., et al. 2007, AJ, 134, 2398

Cox, A. N. 2000, Allen's astrophysical quantities, ed. Cox, A. N.

De Marco, O., Clayton, G. C., Herwig, F., Pollacco, D. L., Clark, J. S., & Kilkenny, D. 2002, AJ, 123, 3387

Di Stefano, R. 2010, ApJ, 712, 728

Djorgovski, S. G., et al. 2011, ArXiv e-prints

Downes, R. A., Duerbeck, H. W., & Delahodde, C. E. 2001, Journal of Astronomical Data, 7, 6

Dupree, A. K., & Smith, G. H. 1995, AJ, 110, 405

Edmonds, P. D., & Gilliland, R. L. 1996, ApJ, 464, L157

Eggleton, P. P. 1983, ApJ, 268, 368

Faber, S. M., Friel, E. D., Burstein, D., & Gaskell, C. M. 1985, ApJS, 57, 711

Fabricant, D., Cheimets, P., Caldwell, N., & Geary, J. 1998, PASP, 110, 79

Fröhlich, C. 2006, in ESA Special Publication, Vol. 617, SOHO-17. 10 Years of SOHO and Beyond

Girardi, L., Bressan, A., Bertelli, G., & Chiosi, C. 2000, A&AS, 141, 371

Grindlay, J., Tang, S., Simcoe, R., Laycock, S., Los, E., Mink, D., Doane, A., & Champine, G. 2009, in Astronomical Society of the Pacific Conference Series, Vol. 410, Preserving Astronomy's Photographic Legacy: Current State and the Future of North American Astronomical Plates, ed. W. Osborn & L. Robbins, 101

Gutierrez-Soto, J., et al. 2008, Communications in Asteroseismology, 157, 70

Hauschildt, P. H., Allard, F., Ferguson, J., Baron, E., & Alexander, D. R. 1999, ApJ, 525, 871

Hoffmeister, C., Richter, G., & Wenzel, W. 1990, Variable stars, ed. Hoffmeister, C., Richter, G., & Wenzel, W.

Høg, E., et al. 2000, A&A, 355, L27

Hubble, E. 1929, Proceedings of the National Academy of Science, 15, 168

Hubert, A. M., & Floquet, M. 1998, A&A, 335, 565

Iben, Jr., I. 2003, in Astronomical Society of the Pacific Conference Series, Vol. 303, Astronomical Society of the Pacific Conference Series, ed. R. L. M. Corradi, J. Mikolajewska, & T. J. Mahoney, 177

Kaiser, N., et al. 2002, in Society of Photo-Optical Instrumentation Engineers (SPIE) Conference Series, Vol. 4836, Society of Photo-Optical Instrumentation Engineers (SPIE) Conference Series, ed. J. A. Tyson & S. Wolff, 154–164

Kato, M., & Hachisu, I. 1994, ApJ, 437, 802

Kato, M., Hachisu, I., Cassatella, A., & González-Riestra, R. 2011, ApJ, 727, 72

Kenyon, S. J. 1986, The symbiotic stars, ed. Kenyon, S. J.

—. 1994, Mem. Soc. Astron. Italiana, 65, 135

Kenyon, S. J., & Webbink, R. F. 1984, ApJ, 279, 252

King, A. R., Rolfe, D. J., & Schenker, K. 2003, MNRAS, 341, L35

Kraft, R. P. 1967, ApJ, 150, 551

Krautter, J., et al. 2002, AJ, 124, 2888

Kriz, S., et al. 1980, Bulletin of the Astronomical Institutes of Czechoslovakia, 31, 284

Kurucz, R. L. 2005, Memorie della Societa Astronomica Italiana Supplementi, 8, 14

Lang, D., Hogg, D. W., Mierle, K., Blanton, M., & Roweis, S. 2010, AJ, 139, 1782

Lasker, B. M., Sturch, C. R., McLean, B. J., Russell, J. L., Jenkner, H., & Shara, M. M. 1990, AJ, 99, 2019

Law, N. M., et al. 2009, PASP, 121, 1395

Laycock, S., Tang, S., Grindlay, J., Los, E., Simcoe, R., & Mink, D. 2010, AJ, 140, 1062

Leavitt, H. S., & Pickering, E. C. 1912, Harvard College Observatory Circular, 173, 1

Liller, M. H., & Liller, W. 1979, AJ, 84, 1357

Linsky, J. L., McClintock, W., Robertson, R. M., & Worden, S. P. 1979, ApJS, 41, 47

Los, E., Grindlay, J., Tang, S., Servillat, M., & Laycock, S. 2011, in Astronomical Society of the Pacific Conference Series, Vol. 442, Astronomical Data Analysis Software and Systems XX, ed. I. N. Evans, A. Accomazzi, D. J. Mink, & A. H. Rots, 269

Masetti, N., et al. 2002, A&A, 382, 104

—. 2007, A&A, 470, 331

Mikołajewska, J. 2003, in Astronomical Society of the Pacific Conference Series, Vol. 303, Astronomical Society of the Pacific Conference Series, ed. R. L. M. Corradi, J. Mikolajewska, & T. J. Mahoney, 9

Mikołajewska, J. 2007, Baltic Astronomy, 16, 1

Mikolajewska, J. 2010, ArXiv e-prints

Mikolajewska, J., Kolotilov, E. A., Shenavrin, V. I., & Yudin, B. F. 2002, in Astronomical Society of the Pacific Conference Series, Vol. 261, The Physics of Cataclysmic Variables and Related Objects, ed. B. T. Gänsicke, K. Beuermann, & K. Reinsch, 645

Mikolajewski, M., Mikolajewska, J., & Khudiakova, T. N. 1990, A&A, 235, 219

Mink, D. J. 2002, in Astronomical Society of the Pacific Conference Series, Vol. 281, Astronomical Data Analysis Software and Systems XI, ed. D. A. Bohlender, D. Durand, & T. H. Handley, 169

Mink, D. J. 2011, in Astronomical Society of the Pacific Conference Series, Vol. 442, Astronomical Data Analysis Software and Systems XX, ed. I. N. Evans, A. Accomazzi, D. J. Mink, & A. H. Rots, 305

Morton, T. D., & Johnson, J. A. 2011, ApJ, 738, 170

Mowlavi, N. 1999, A&A, 344, 617

Muerset, U., Nussbaumer, H., Schmid, H. M., & Vogel, M. 1991, A&A, 248, 458

Murset, U., & Nussbaumer, H. 1994, A&A, 282, 586

Nomoto, K., Saio, H., Kato, M., & Hachisu, I. 2007, ApJ, 663, 1269

Nussbaumer, H. 2000, in Astronomical Society of the Pacific Conference Series, Vol. 204, Thermal and Ionization Aspects of Flows from Hot Stars, ed. H. Lamers & A. Sapar, 317

Olson, E. C. 1988, AJ, 96, 1439

—. 1991, AJ, 102, 1423

Olson, E. C., & Etzel, P. B. 1995, AJ, 109, 1308

Olson, E. C., Etzel, P. B., & Dewey, M. R. 1995, AJ, 110, 2378

Origlia, L., Ferraro, F. R., Fusi Pecci, F., & Rood, R. T. 2002, ApJ, 571, 458

Orosz, J. A., & Hauschildt, P. H. 2000, A&A, 364, 265

Paczynski, B., & Rudak, B. 1980, A&A, 82, 349

Palacios, A., Charbonnel, C., & Forestini, M. 2001, A&A, 375, L9

Pasquini, L., de Medeiros, J. R., & Girardi, L. 2000, A&A, 361, 1011

Percy, J. R. 2007, Understanding variable stars, ed. Percy, J. R.

Perlmutter, S., et al. 1999, ApJ, 517, 565

Pickles, A. J. 1998, PASP, 110, 863

Pigulski, A., Pojmański, G., Pilecki, B., & Szczygieł, D. M. 2009, Acta Astron., 59, 33

Podsiadlowski, P., & Mohamed, S. 2007, Baltic Astronomy, 16, 26

Pojmanski, G. 2002, Acta Astron., 52, 397

Popper, D. M. 1964, ApJ, 139, 143

—. 1965, ApJ, 141, 314

Prialnik, D. 2000, An Introduction to the Theory of Stellar Structure and Evolution, ed. Prialnik, D.

Prialnik, D., & Kovetz, A. 1995, ApJ, 445, 789

Riess, A. G., et al. 1998, AJ, 116, 1009

Sackmann, I.-J., Boothroyd, A. I., & Kraemer, K. E. 1993, ApJ, 418, 457

Salaris, M., Cassisi, S., & Weiss, A. 2002, PASP, 114, 375

Schlegel, D. J., Finkbeiner, D. P., & Davis, M. 1998, ApJ, 500, 525

Servillat, M., Los, E. J., Grindlay, J. E., Tang, S., & Laycock, S. 2011, in Astronomical Society of the Pacific Conference Series, Vol. 442, Astronomical Data Analysis Software and Systems XX, ed. I. N. Evans, A. Accomazzi, D. J. Mink, & A. H. Rots, 273

Shen, K. J., & Bildsten, L. 2007, ApJ, 660, 1444

Simcoe, R. J., Grindlay, J. E., Los, E. J., Doane, A., Laycock, S. G., Mink, D. J., Champine, G., & Sliski, A. 2006, in Society of Photo-Optical Instrumentation Engineers (SPIE) Conference Series, Vol. 6312, Society of Photo-Optical Instrumentation Engineers (SPIE) Conference Series

Skopal, A. 2008, Journal of the American Association of Variable Star Observers (JAAVSO), 36, 9

Skopal, A., et al. 1996, MNRAS, 282, 327

Skrutskie, M. F., et al. 2006, AJ, 131, 1163

Smak, J. I., & Plavec, M. J. 1997, Acta Astron., 47, 345

Smith, J. A., et al. 2002, AJ, 123, 2121

Soderblom, D. R. 1983, ApJS, 53, 1

Sokoloski, J. L., et al. 2006, ApJ, 636, 1002

Starrfield, S., Timmes, F., Iliadis, C., Hix, W., Arnett, W., Meakin, C., & Sparks, W. 2012, Baltic Astronomy, 21, 75

Stasińska, G., & Tylenda, R. 1990, in Lecture Notes in Physics, Berlin Springer Verlag, Vol. 369, IAU Colloq. 122: Physics of Classical Novae, ed. A. Cassatella & R. Viotti, 293

Strassmeier, K. G., Handler, G., Paunzen, E., & Rauth, M. 1994, A&A, 281, 855

Szentgyorgyi, A. H., & Furész, G. 2007, in Revista Mexicana de Astronomia y Astrofisica Conference Series, Vol. 28, Revista Mexicana de Astronomia y Astrofisica Conference Series, ed. S. Kurtz, 129–133

Takeuchi, T., & Lin, D. N. C. 2003, ApJ, 593, 524

Tang, S., Grindlay, J., Los, E., & Laycock, S. 2010, ApJ, 710, L77

Tang, S., Grindlay, J., Los, E., & Servillat, M. 2011a, ApJ, 738, 7

Tang, S., Grindlay, J., Moe, M., Orosz, J., Kurucz, R., Quinn, S., & Servillat, M. 2011b, ArXiv e-prints

Tokarz, S. P., & Roll, J. 1997, in Astronomical Society of the Pacific Conference Series, Vol. 125, Astronomical Data Analysis Software and Systems VI, ed. G. Hunt & H. Payne, 140

Townsley, D. M., & Bildsten, L. 2004, ApJ, 600, 390

Tsuji, T. 2009, A&A, 504, 543

Tyson, J. A., Wittman, D. M., Hennawi, J. F., & Spergel, D. N. 2003, Nuclear Physics B Proceedings Supplements, 124, 21

Udalski, A., Kubiak, M., & Szymanski, M. 1997, Acta Astron., 47, 319

Vinković, D. 2009, Nature, 459, 227

Walker, A. R. 2003, Mem. Soc. Astron. Italiana, 74, 999

Whitelock, P. A., Feast, M. W., Marang, F., & Groenewegen, M. A. T. 2006, MNRAS, 369, 751

Wurm, G., & Haack, H. 2009, in Astronomical Society of the Pacific Conference Series, Vol. 414, Cosmic Dust - Near and Far, ed. T. Henning, E. Grün, & J. Steinacker, 509

Zahn, J.-P. 1989, A&A, 220, 112

Zola, S. 1992, Acta Astron., 42, 355